Numerical and Experimental Studies of a Small Vertical-Axis Wind Turbine with Variable-Pitch Blades

Dissertation

Numerical and Experimental Studies of a Small Vertical-Axis Wind Turbine with Variable-Pitch Blades

（可変ピッチ翼を有する小形垂直軸風車の数値及び実験的研究）

Graduate School of
Natural Science & Technology
Kanazawa University

Division of Innovative Technology and Science

Student ID No. : 1123122216

Name : Rachmat Firdaus

Chief advisor : Prof. Kiwata Takahiro

Date of Submission : January 09, 2015

Abstract

Wind power is play important role of future energy due to renewable, cheap, low maintenance, continuous and ecofriendly. Wind power contribute of CO_2 emission and its can reduce dependence of fossil fuel which limited reservoir in the world recently. The global wind power grew increase and become renewable energy targets in last decade and future.

The wind turbine can be classified into two groups. The first group is the orientation of the axis of rotation of the turbine (parallel or transverse to the wind flow) which i.e. horizontal axis wind turbine (HAWT) and vertical axis wind turbine (VAWT). The second is the power generation source, which i.e. wind turbines are called lift-based or drag-based. The Darrieus, Savonius, and Orthopter wind turbine are vertical axis wind turbine.

Generally, HAWTs have higher efficiency than all VAWTs followed by Darrieus turbine (lift-based type) and Savonius turbine (drag-based type). However, VAWTs have many advantages, such as being omni-directional without needing a yaw control system, having better aesthetics for their integration into buildings, and having lower sound emissions; therefore, VAWTs are expected to be used in urban areas.

Torque generation of rotor blade of Darrieus and drag-type turbine are vary correspondent to azimuth position. Positive torque of Darrieus turbine mostly generate at upstream area and decreasing power generation at downstream area due to wake effect. The drag-type turbine has positive torque generation at advising blade position or lower side wind area. The drawback of drag-type turbine is negative power in upper wind area due to reverse force on the returning blade. The dynamic stall phenomenon, which is a major component of the unsteady aerodynamics of a Darrieus wind turbine at low tip speed ratio contribute on the drawback of turbine.

Therefore, modified of pitch angle rotor blades of WAVTs are needed to overcome turbine disadvantages. There are two type modifications, the first is Darrieus wind turbine with variable pitch, and the second is the Orthopter wind turbine. The orthopter wind turbine is combination between a drag-type and a lift-type vertical axis wind turbine. The blade rotor of orthopter wind turbine enable rotating its own axis and turbine's shaft axis as simultaneously. .

Numerical studies and experiment of both the wind turbines were carried out using ANSYS Fluent 13.0 programs and wind tunnel test. The effect of variable pitch angle blade of Darrieus wind turbine and the effect number and aspect ratio of rotor of the orthopter wind turbine were investigated.

The results showed good agreement of both numerical and experiment of the performance the wind turbines. The variable pitch blades of Darrieus wind turbine give significant effect on the power generation and aerodynamic behaviour. The effect number of blade, aspect ratio of rotor, and tip speed ratio influence on the performance of Orthopter wind turbine.

Acknowledgments

First of all, I would like to thank my supervisor Professor Takahiro KIWATA for many valuable suggestion, discussion, support and encouragement. I learned a lot of many things; research, wind turbine, fluid mechanic from his expertise.

I would like to express my gratitude to Professor Shigeo KIMURA for support, suggestion, advice, and discussion. I learned a lot of many things; research, heat transfer from his expertise.

I would like to express my gratitude to Associate Professor Hiroshi ENOMOTO, Professor Nobuyoshi KAWABATA, Associate Professor Yoshikazu TERAOKA, Associate Professor Yukio TADA, Dr. Nobuyoshi KOMATSU, Dr. Takaaki KONO for support, suggestion, and discussion.

I would like to give thanks to Mr. Koji NAGAO, Mr. Tomohiro KURATANI, Mr. Yoshiaki SAWADE, Ms. Yurie KOAMI, and DAIDO Company for our research.

I also would like to thank to my Government and Kanazawa University for support my scholarship and any help since beginning until end of my study.

Finally, many thanks to express my sincerest appreciate to my family, all my Japanese and Indonesian friends for their moral support.

Contents

List of Figures

Chapter 1 Introduction

1.1 Background

Wind power is an important energy source that having a beneficial effect on the environment or ecofriendly and lower risk for utilization in the last decade and future. All wind turbines installed is increasing every year and many countries do intensify their effort in wind power development in the future. Wind power generation does not cause the emission of carbon dioxide and pollution, and thus the capacity of wind power generation has increased rapidly in recent years. Global warming and climate change will have a decisive impact on the mid-term and long-term prospects of wind power, which has increased awareness of potential contributions of wind energy, including economic, social, and ecological sustainability, to the total energy supply (WWEA, 2011).

Wind power has simple of construction and minimize risk of dangerous. Many countries have made plans for investments in wind turbines. Wind varies with time in intensity and direction, and the potential of a wind site is generally evaluated as a function of the annual average wind speed. Wind power available more continuously compared than solar energy and water power. The solar energy is effective in the daytime and dependent on season like water power in several countries. Low cost maintenance of wind power is one of reason.

Globally, the all wind turbines types that can be classification into two groups. The classification of group is depending on the orientation of their axis of rotation relatively to wind, namely horizontal axis wind turbines (HAWTs) and vertical axis wind turbines (VAWTs). Horizontal axis wind turbines such as propeller type is the most common type which have more higher coefficient of performance than vertical axis wind turbines. The vertical axis wind turbine appears to be advantageous to the horizontal axis wind turbine in many aspects. Many advantages could be performed effectively by vertical axis wind turbine using mechanical drive, For instance; pumping water, purifying and desalinating water. There are three common type of Vertical axis wind turbine such as H-rotor type, Darrieus model and Savonius type.

Another type of wind turbines are based on the power generation source which i.e. lift-based type and drag-based type. The Darrieus wind turbine is lift-based type wind

turbine which major power generation from lift force by rotor blade in one revolution. The orthopter wind turbine is combination between lift- and drag-based types. Due to movement of blade rotor, enable to pitch angle vary correspondent to azimuthal angle position. Therefore, at azimuthal angle $\theta = 270$ blade perpendicular to wind flow and maximum drag generated.

In the Figure 1-1 show the wind turbine types (VAWTs and HAWTs). The vertical axis wind turbine which i.e., Darrieus wind turbine and Savonius wind turbine. In Figure 1-2 shows the performance maximum of all type wind turbine. The highest maximum performance is HAWT followed Darrieus model while Savonius model is low maximum performance and low tip speed ratio operation.

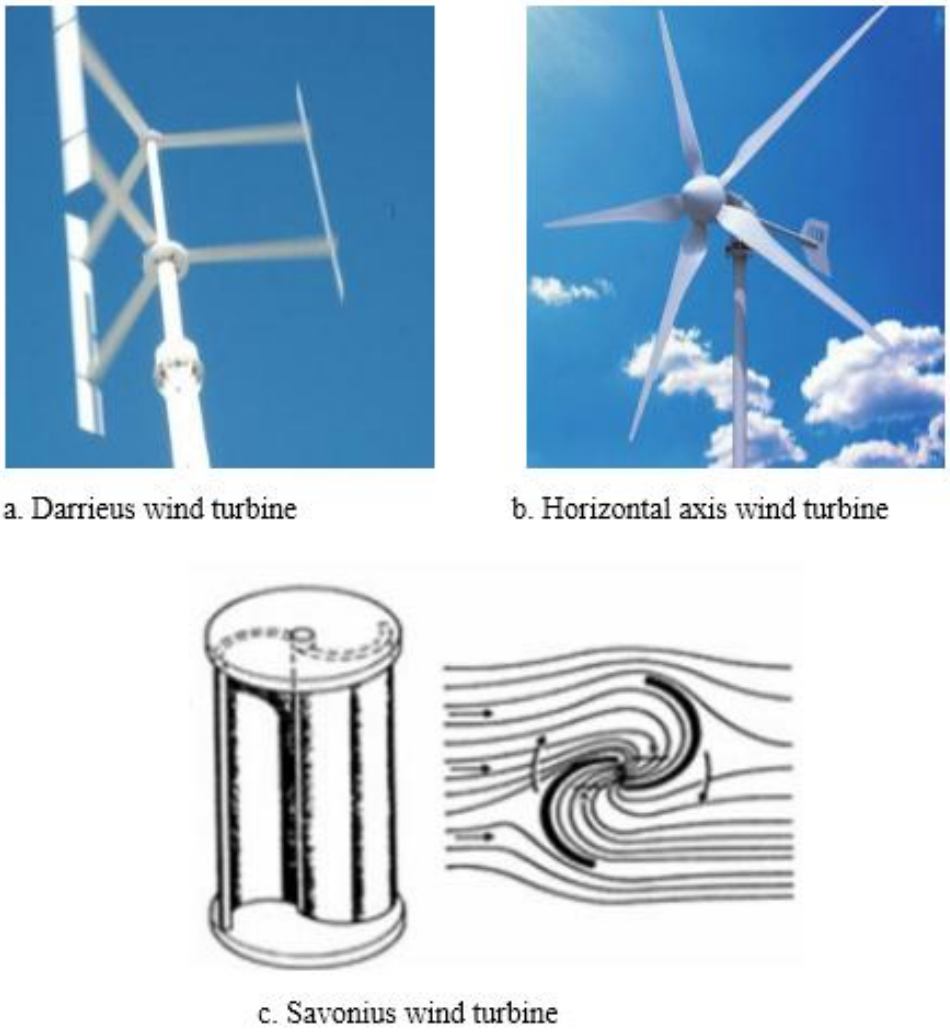

Figure 1-1 Wind turbine types

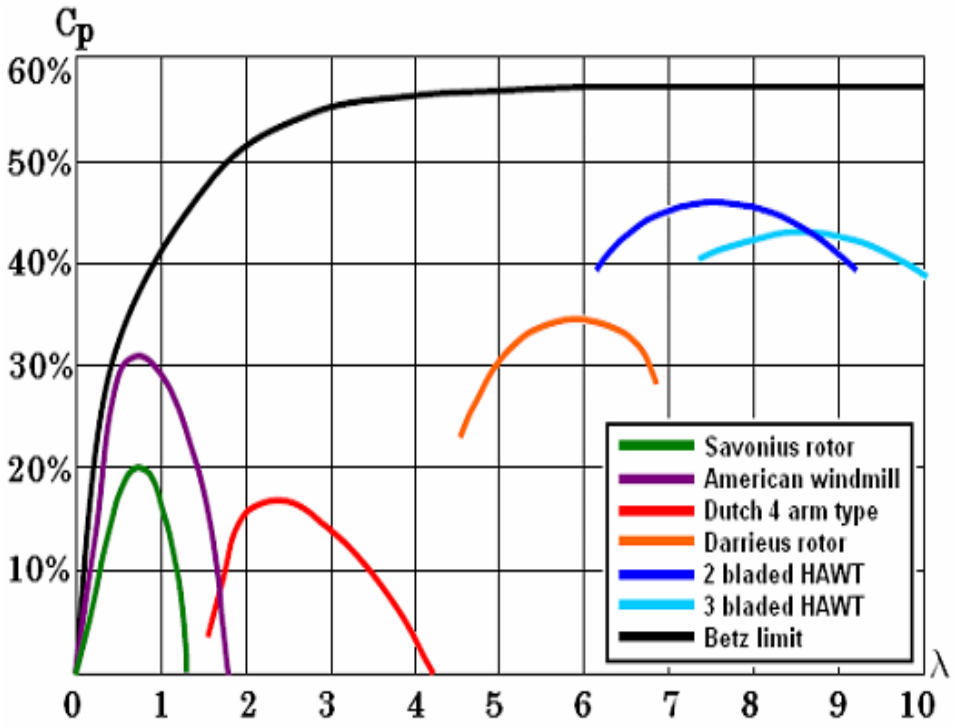

Figure 1-2 Performance of all wind turbine types (Hau, 2000)

Table 1 Aspect level of wind turbines type (*, Erickson S., 2008)

no	Aspect	*H-rotor WT	*Darrieus WT	*HAWT	Savonius WT
1	Blade profile	Simple	Complicated	Complicated	Simple
2	Self-starting	No	No	Yes	Yes
3	Blade area	Moderate	Large	Small	Large
4	Yaw mech. needed	No	No	Yes	Optional
5	Pitch mech. possible	Yes	No	Yes	No
6	Noise	Low	Moderate	High	Low
7	Generator position	On ground	On ground	On top tower	On ground
8	Coefficient power	Moderate	Moderate	High	Low
9	Overall structure	Simple	Simple	Complicated	Simple
10	Foundation	Moderate	Simple	Complicated	Simple
11	Safety	Low risk	Low risk	High risk	Low risk
12	Max tip speed ratio	Medium	Medium	High	Low
13	Solidity	Medium	Medium	Low	Medium

Figure 1-3 shows total installed wind capacity and prediction until 2020. Total wind capacity include large and small wind turbine. The trend of wind turbine in future is very sharp rise.

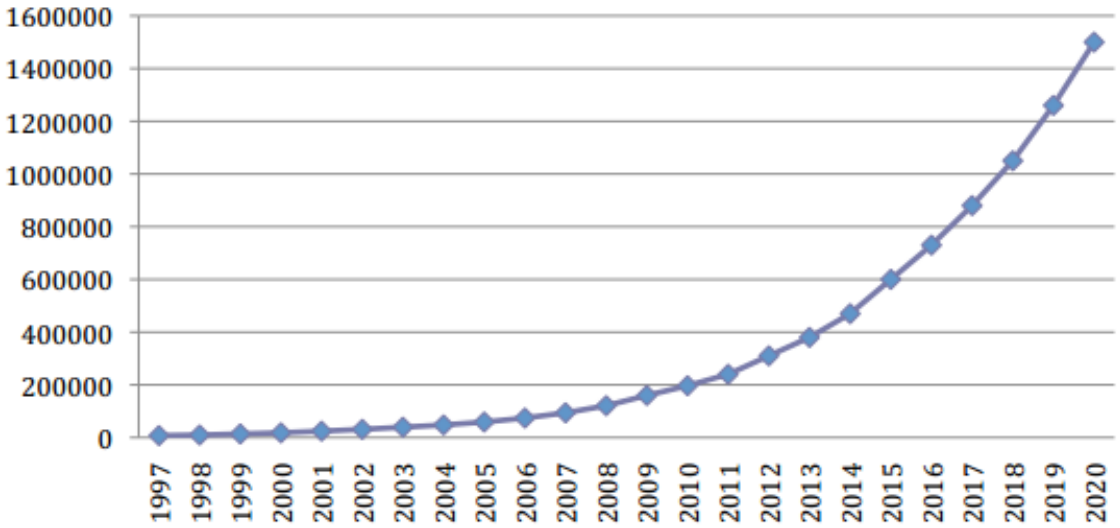

Figure 1-3 Total installed wind capacity [MW] (WWEA, 2013)

Figure 1-4 shows annual forecasting of installed small wind turbine until 2020. The trend of utilizing of small wind turbine is increase as increase of total wind turbine. Total large wind turbine installed is higher than small wind turbine. However, growth of small wind turbine installed is significant due to many aspects into consideration in order to benefit of small wind turbine

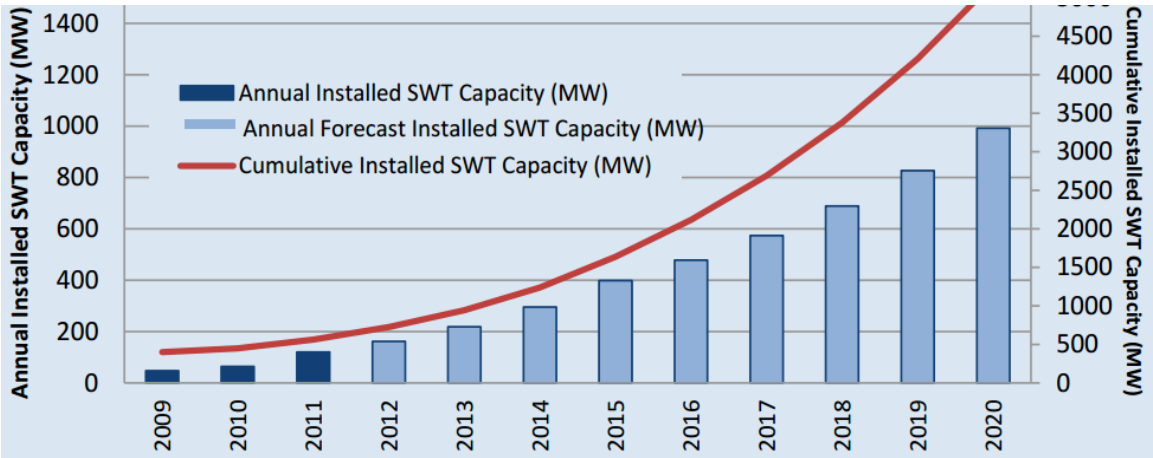

Figure 1-4 SWT Installed Capacity World Market Forecast 2009 – 2020 (WWEA, 2013)

Figure 1-5 shows small wind turbine orientation by manufactured in 2011. The vertical axis wind turbine type has 18% of total small wind turbine manufacture. Most of small wind turbine manufactures produce HAWT type by 74%.

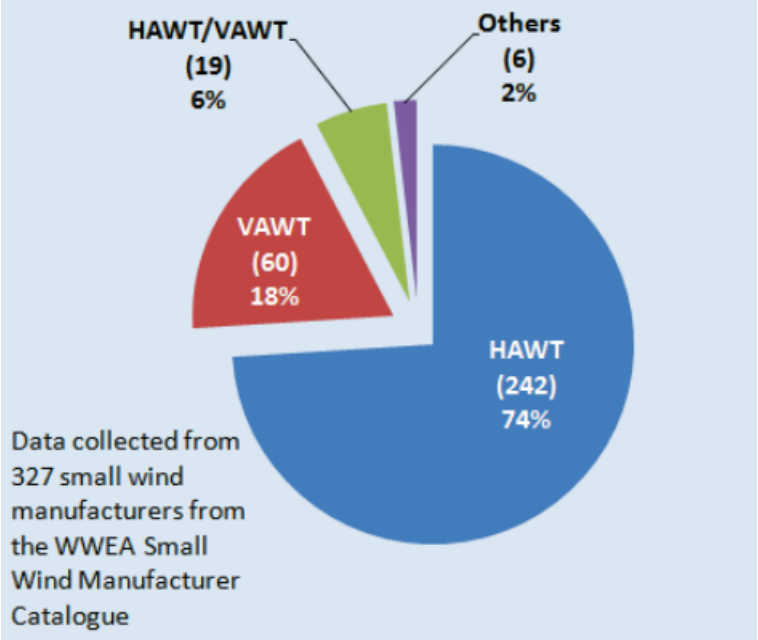

Figure 1-5 Small wind turbine orientation by manufacture, 2011 (WWEA 2013)

Figure 1-6 shows the country installed of small wind turbine in the world. China and USA are very dominant of total cumulative installed small wind turbine followed by UK.

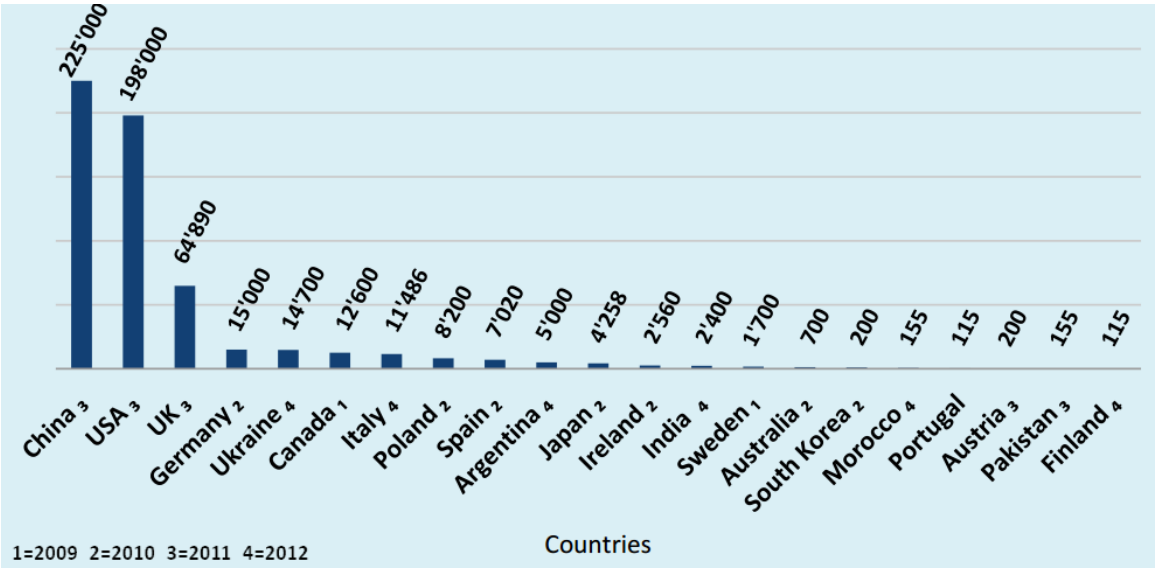

Figure 1-6 Total Cumulative Installed Small Wind Capacity Worldwide (WWEA, 2013)

1.2 The Brief overview of past Study

The experiment and computational studies on 2-D and 3-D models at different Reynolds numbers were performed by Howell et al. (2009) and Claessens (2006). Effect of surface roughness was also taken into consideration. The results show 3-D computational results in a good agreement with the experiments. It was concluded that 2-D CFD results are always higher than 3-D CFD results due to the presence of end tip vortices which causes circulation in real wind turbine. The effect loss end tip vortices and rotor arm are ignored in 2 –D simulation. Periodic pattern of torque coefficient was also observed. Claessens (2006) studied the effect of Reynolds number, airfoil thickness and tip speed ratio on NACA 0012, NACA 0015, NACA 0018, and NACA 0021.

Numerical and experimental studies of VAWTs have been carried out by several researchers, including Castelli et al. (2011), Takao et al. (2008), Howell et al. (2010), Sato et al. (2011) and Chong et al. (2013). Guerri et al. (2007) and Chen and Zhou (2009) both analyzed the own around a rotating VAWT by using Reynolds Averaged Navier Stokes (RANS) solver in 2-D simulation. The NACA 0018 airfoil type was chosen for both the studies and Sliding mesh technique was used to make a moving mesh. The SST k-ω turbulent model was used to get the own details near the wall of the blades. Due to the improving performance of VAWTs with straight fixed-pitch blades, Tanaka et al. (2011) have studied the effects of blade profiles (NACA0018, NACA4418 with its camber facing outward, and NACA4418 with its camber facing inward) and setting angle on the performance of a small straight-bladed VAWT. They indicated that the starting performance of the VAWT with the NACA0018 can be further improved by setting the wings at an outward angle of 5 degrees. Yamada et al. (2011) have also studied the effects of the camber and thickness of a blade (NACA0020, 3520, 6518, 6520, 6525, 6530, and 8520) on the performance of a small straight-bladed VAWT. Their report showed the mean and temporal torque variation at any azimuth angle of one and two blades.

As part of a numerical simulation, Chen and Kuo (2013) have studied the effects of pitch angle and blade camber on the unsteady flow characteristics and the performance of a small-size Darrieus wind turbine with the NACA0012, 2412, and 4412 blade profiles. Their results indicated that the self-starting ability and the moment coefficients of a VAWT that has blades with large cambers (NACA4412) are better than those with the other blades (NACA0012 and 2412). Chen and Zhou (2013) used the SST k-ω

model to investigate the aerodynamic performance of a VAWT via a two-dimensional numerical simulation. The results showed the optimum pitch angle for the power coefficient of the VAWT. Aresti et al. (2013) conducted two- and three-dimensional numerical simulations of the performance and flow through a small scale H-type Darrieus wind turbine by using the RNG k-ε, standard k-ε, and standard k-ω turbulence models. The self-starting capabilities of the VAWT were found to increase with the increasing mount angle of attack of the blades. Almohammadi et al. (2013) investigated the mesh independence of the predicted power coefficient of a VAWT with straight blades by employing a two-dimensional numerical simulation. Roh and Kang (2013) investigated the effects of a blade profile, the Reynolds number, and the solidity on the performance of a straight-bladed VAWT by using the numerical procedure of the multiple stream tube method. McNaughton et al. (2014) presented a two-dimensional numerical investigation of a VAWT, which had a high solidity of 1.1, and investigated the effects of the original and a modified version of the SST models for low Reynolds numbers on the flow structure, dynamic stall, and blade-vortex interaction.

Due to the phenomenon called a dynamic stall, which is a major component of the unsteady aerodynamics of a Darrieus wind turbine with a low tip speed ratio (TSR) (Nobile et al., 2011; Paraschivoiu, 2002), an aerodynamic analysis of a VAWT is complex. The dynamic stall of a blade can produce a lift force and pitching moment values that exceed static values. The dynamic stall process depends on both the amplitude and the history of angles of attack of the airfoil (Spera, 2009). Due to the formation of vortices, which reduce the static pressure on the suction side of the rotor blade, the presence of a dynamic stall at low TSRs can have a positive impact on power generation; however, the formation of vortices can have negative consequences such as vibration, noise, and a reduction in the fatigue life of the components of the VAWT (Fujisawa and Shibuya, 2001) during operation. A VAWT with straight variable-pitch blades can change the amplitude and the rate of increase of the angle of attack in one revolution, compared to a VAWT with straight fixed-pitch blades. Simão Ferreira et al. (2007, 2009, and 2010) investigated the dynamic stall of a two-dimensional single-bladed VAWT via PIV and evaluated the differences between the commonly used turbulence models. Zhang et al. (2013) predicted the aerodynamic performance and the flow field of a straight-bladed VAWT. The power coefficient of the two-dimensional computational fluid dynamics (CFD) agreed well with the experimental data, and it was

demonstrated that the RNG *k*-ε turbulent model is a useful resource to predict the tendency of aerodynamic forces; however, the model requires a high estimate value of the turbulence viscosity coefficient.

The development of VAWTs with variable-pitch straight blades has been carried out to obtain a high starting torque and high efficiency during operating speeds. A few of these VAWTs include the ASI/PINSON wind turbine (Noll and Zvara, 1981), a Giromill wind turbine (Anderson, 1981), a straight-bladed cycloturbine (Nattuvetty and Gunkel, 1982), a VAWT with a self-acting variable pitch system (Pawsey, 1999), and the Orthoptere wind turbine (Shimizu et al., 1997). Kiwata et al. (2010) and Yamada et al. (2012) developed a VAWT with variable-pitch straight blades that have a slight camber using a four-bar linkage without actuators. It was found that the power coefficient of this VAWT is better than that with fixed-pitch blades. Furthermore, this VAWT can direct itself towards the wind, which enables it to utilize the rotational speed control in the turbine via its tail vanes.

A previous study by Bayeul et, al [5] confirmed that the performance of this kind of turbine was better than those of classical VAWTs for some specific blade stagger. The arrangement of diffuser of the orthopter study by Shimizu [6] confirmed that the arrangement of diffuser on the top and both sides has good performance.

1.3 Motivation and Objectives

Generally, HAWTs have higher efficiency than all VAWTs followed by Darrieus turbine and Savonius turbine. Most of the large wind turbines for power generation are HAWTs. However, VAWTs have many advantages, such as being omni-directional without yaw control, having better aesthetics for integrating into buildings, having more efficiency in turbulent environments, and having lower sound emissions. Therefore, the VAWT is expected to be used in urban areas.

The aerodynamic analysis of a Darrieus wind turbine is very complex due to the angle of attack of blade changes significantly in one revolution. Therefore, it's was influence on two aspect in Darrieus wind turbine operation. First, positive torque of Darrieus turbine mostly generate at upstream area and decreasing power generation at downstream area due to wake effect. Second, the phenomenon called dynamic stall, which is a major aspect of the unsteady aerodynamics of the Darrieus wind turbine at a low tip speed ratio. The dynamic stall of a blade can produce lift force and pitching

moment values that are much larger than static values. The dynamic stall process depends both on the amplitude and the history of the airfoil's angle of attack. The presence of dynamic stall at low TSRs can have a positive impact on power generation due to the formation of vortices, which reduce the static pressure on the suction side of the rotor blade. However, the formation of vortices can have negative consequences during VAWT operation, such as vibration, noise, and a reduction in fatigue life of the VAWT's components.

Drag- based type turbine has positive torque generation at advising blade position or lower side wind area. The drawback of drag- based type turbine is negative power in upper wind area due to reverse force on the returning blade. The concept of the orthopter wind turbine is combination of both lift and drag-based power generation. The purpose of the design is to eliminate negative drag and thus positive power contribution of each blade in one rotational cycle. Therefore, the orthopter expected to create positively contributing torque on each blade at every azimuth position due to a rotating movement around its own axis.

The present study describes of a numerical study on the performance of a Darrieus with variable-pitch straight blades and the Orthopter wind turbine. A two-dimensional numerical simulation of the Darrieus and Orthopter wind turbine were performed using the commercial computational fluid dynamics (CFD) software ANSYS FLUENT 13.0. The effects of the variable pitch angle, the TSR, and the turbulent model on the performance of the Darrieus wind turbine and the unsteady flow around the blades were investigated. The variable aspect ratio and number of blades effect on the performance of orthopter wind turbine by conducting experiment wind tunnel and numerical analysis had investigated.

1.4 Content of the dissertation

As described in the research, to understand physical phenomenon in wind turbines with variable pitch angle blade, such as power performance and aerodynamic behavior affected by variable pitch angle amplitude, tip speed ratio for Darrieus model and aspect ratio, number of blades for orthopter wind turbine. This dissertation is organized as follows;

Chapter 2 presents the aerodynamic of Vertical Axis Wind turbines. This chapter describes aerodynamic of VAWTs based drag type such as Savonius model, aerodynamic based lift type such as Darrieus model, and aerodynamic of VAWTs based lift-drag type such as orthopter model. The aerodynamic analysis of the blade rotor is developed from principal lift and drag force on the airfoil. Performance of wind turbine result from moment of blade rotor due to lift and drag force on the blade.

Chapter 3 presents numerical simulation method of vertical Axis Wind Turbines. This chapter describes prediction power performance of VAWTs by numerical simulations especially Computational Fluid Dynamics base (CFD) model include the flow around of rotor blade of VAWT. There are four underlying principal of turbulence modeling which i.e. Reynolds (Ensemble) Averaging to applied on VAWTs simulations.

Chapter 4 presents performance and aerodynamic on straight – bladed Darrieus wind turbines. The numerical simulation and experimental were carried out on the VAWT with fixed- and variable-pitch straight blades. A two-dimensional numerical simulation of the flow around a VAWT was performed using the commercial CFD software ANSYS FLUENT 13.0. The effects of the variable-pitch angle, TSR, and the turbulent models turbulent models, on the performance of the VAWT were investigated

Chapter 5 presents performance and aerodynamic on Flat-Plate Blades Orthopter Wind Turbine. The purpose of this chapter is to investigate of the effects of various parameters such as; aspect ratio, number of blade and tip speed ratio corresponding to performances by experiments and numerical study.

Chapter 6 presents of summary all chapters.

Chapter 2 Aerodynamic of VAWTs

2.1 Wind Turbine Parameters

Velocity is one aspect in wind turbine which i.e., Wind velocity, Tangential velocity, Induced velocity, and Relative velocity. Wind velocity or free-stream velocity (V_∞) is uniform flow speed of wind. Induced velocity (V_i) is inlet velocity of the rotor blade, it depends on wake condition. The vertical axis wind turbine has difference of inlet velocity between upstream and downstream area. Tangential velocity define velocity of blade which the result of multiplying the angular velocity and the radius of rotor wind turbine ($V_t = \omega . R$). Relative velocity ($\boldsymbol{W}$) is sum of vector velocity of inlet velocity and tangential velocity ($\boldsymbol{W = V_i + V_t}$).

Tip speed ratio (λ) is defined ratio tangential velocity of blade rotor to free-stream velocity ($\lambda = V_t / V_\infty$). Aspect ratio (AR) is defined ratio chord length of blade to length of span blade ($AR = C/ L$). Solidity (σ) is defined ratio of total blade area to circumference area for VAWT and swept area for HAWT ($\sigma = n .C /A$). Swept area (A) equals the projected frontal area of the wind turbine given by the height of rotor times the diameter of the rotor ($A = L. D$) for the VAWT and ($A = \pi R^2$) for the HAWT.

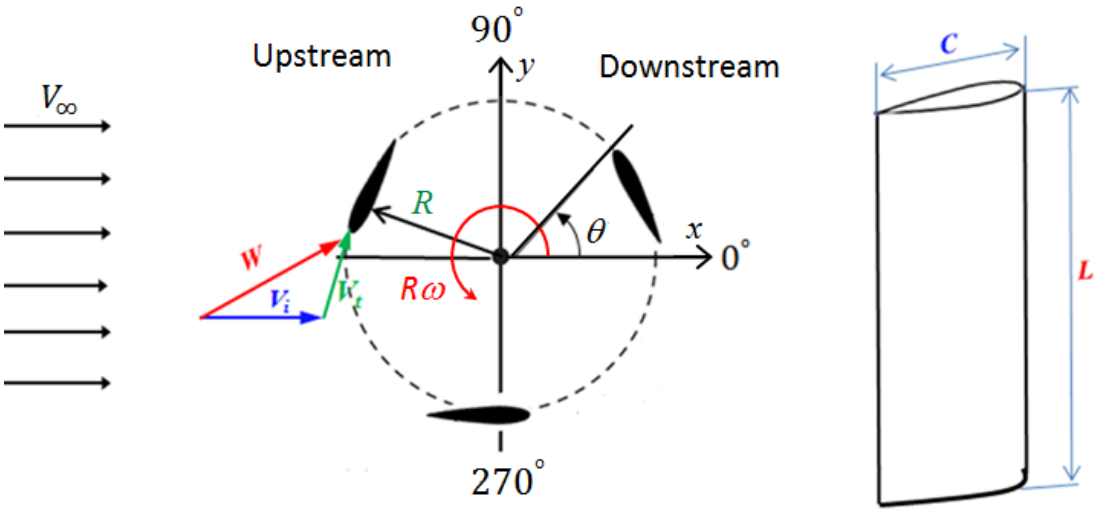

Figure 2-1 Parameter on the VAWT

The power coefficient (C_P) is performance of wind turbine. This coefficient represents ratio the produced energy of the wind turbine to the total wind energy passing through the swept area of the wind turbine. This coefficient is normally plotted against the tip speed ratio λ at a certain free-stream velocity or Reynolds number based on diameter rotor or chord length blade.

Equation 2-1

$$C_P = \frac{P}{0.5\rho A V^3}$$

$$P = T.\omega$$

T = torque of rotor shaft wind turbine (measured by torque transducer)

ω = rotational speed of rotor shaft wind turbine

C_T = Torque coefficient

Equation 2-2

$$C_T = \frac{T}{0.5\rho A V^2}$$

2.2 Basic aerodynamic of power generation

2.2.1 Power of VAWTs based on drag type

The power extraction from free-stream airflow can be determines using the axial momentum theory [Rankine 1865, W. Froude 1878, R. Froude 1889]. The wind turbine open flow capture the wind energy and extracted it for calculation the maximum power by German physicist Albert Betz [1918] . The thrust and power of wind turbine can be calculated by applying requirements for continuity, momentum, and energy equation with assume the flow to be entirely axial, with no rotational motion. Two thrust equations can be obtained and it's were expressed in Eq.2-3 and Eq. 2-4. First equation, from the momentum theorem, the thrust is

Equation 2-3

$$T = \dot{m}_a(V_\infty - V_e) = \rho A V(V_\infty - V_e)$$

The second equation from pressure drop

Equation 2-4

$$T = A(p_u - p_d)$$

where p_u, p_d= pressures upwind and downwind of the disk, respectively (N/m2)

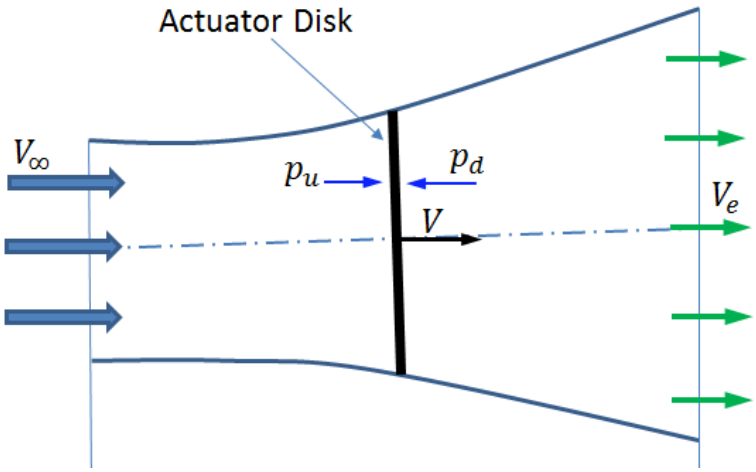

Figure 2-2 Flow through a wind turbine represented by actuator disk

Bernoulli equation is applied for between the free-stream and the upstream side and it's also used between downstream side of the turbine and far wake, so that
Equation (2-3) becomes

Equation 2-5

$$T = 0.5\ \rho\ A(V_\infty^2 - V_e^2)$$

Combining Equations (2-2) and (2-3) we obtain

Equation 2-6

$$V = 0.5\ (V_\infty - V_e)$$

Thus, the wind velocity at the disk is the average of the free-stream and far-wake velocities, the total velocity change from free-stream to far-wake is twice the change from free-stream to the disk.

Equation 2-7

$$V_\infty - V = a\,V_\infty$$

Then

Equation 2-8

$$V_\infty - V_e = 2\,a\,V_\infty$$

The term *a* is known as the *axial induction factor* and is a measure of the influence of the turbine on the wind. Because the minimum far-wake velocity is zero, according to equation (2.5b) the maximum value of the axial induction factor (*a*) is 0.5. From the *first law of thermodynamics*, assuming isothermal flow and ambient pressure in the far wake, power is equal to

Equation 2-9

$$P = 0.5\ \rho\ AV(V_\infty^2 - V_e^2) = 0.5\ \rho\ AV(V_\infty + V_e)(V_\infty - V_e)$$

Combining Equations (2-5) and (2-6), the power coefficient for the actuator disk, according to the Rankine-Froude theory, is

Equation 2-10

$$C_p = \frac{P}{0.5\,A\rho V_\infty^3} = 4a\,(1-a)^2$$

The C_p is maximum if *a* = 1/3 and then the value $C_p = {}^{16}/_{27} = 0.593$

Therefore, the extraction power from wind energy has maximum efficiency is 0.593.

The important factor which influences the actual power of wind turbine are drag force and lift force that contribute of torque generation.

For single blade the equation can be defined as

Equation 2-11

$$D = C_D\,0.5\ \rho\ A\,(V_\infty - v)^2$$

Equation 2-12

$$P = D.\,v$$

$$P = C_D\,0.5\ \rho\ A\,(V_\infty - v)^2.\,v$$

Equation 2-13

$$Cp = \frac{P}{0.5A\ \rho V_\infty^3}$$

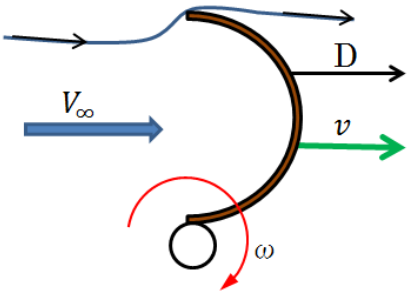

Figure 2-4 Single blade rotor

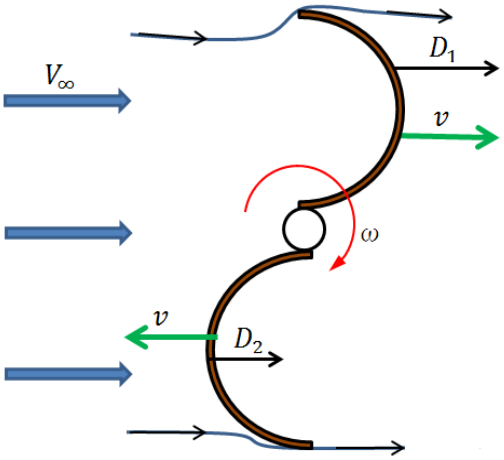

Figure 2-4 Double blade rotor

For double blade rotor the equation becomes

Equation 2-14

$$D_1 = 0.5 C_{D1}\, \rho\, A\, (V_\infty - v)^2$$

Equation 2-15

$$D_2 = 0.5 C_{D2}\, \rho\, A\, (V_\infty + v)^2$$

$$P = (D_1 - D_2).\, v$$

$$= 0.5.\, \rho\, Av[C_{D1}\ (V_\infty - v)^2 - C_{D2}\ (V_\infty + v)^2]$$

$$C_P = \frac{P}{0.5A\ \rho {V_\infty}^3}$$

$$= \frac{0.5.\rho\, Av\left[\ {V_\infty}^2 (C_{D1} - C_{D2}) - 2V_\infty v\ (C_{D1} + C_{D2}) + v^2\ (C_{D1} - C_{D2})\ \right]}{0.5A\ \rho V_\infty}$$

For Circular plate C_D = 1.11

Square plate C_D = 1.1

Semi-sphere (open back) C_{D2} = 0.34

Semi-sphere (open front) C_{D1} = 1.33

2.2.2 Power of VAWTs based on lift type

The Darrieus wind turbines use airfoil on the rotor blade. It is operate by the action of aerodynamic forces on the rotating blades which created by the relative wind (induced flow and tangential velocity caused by rotor rotation speed). Generally, the aerodynamic force on the rotor blade can be grouped into *lift- forces* and *drag- forces.* Lift forces created by generation of circulation which perpendicularly with relative wind on come on the blade. The drag force is parallel and opposite to relative wind and caused by form drag or pressure drag that depend on blade shape and skin friction due to viscous effect on the surface that derived from wall shear stress. For the 3D airfoil induced drag effect generated by favorable pressure gradient on upper side (low pressure) and lower side (high pressure) at tip airfoil. The flow separation on the blade can influence on the drag force. The lift force and drag force vary depend on incident angle on the blade or airfoil and its known an angle attack. "When considering the potential impact of wakes on the total output of a wind power station, a lift-type device is again preferred, since a drag-type unit develops a greater wake and less energy is available to downwind units. Thus, the array efficiency of a cluster of drag-type units will be lower than that of lift-type turbines" (Spera, 2009).

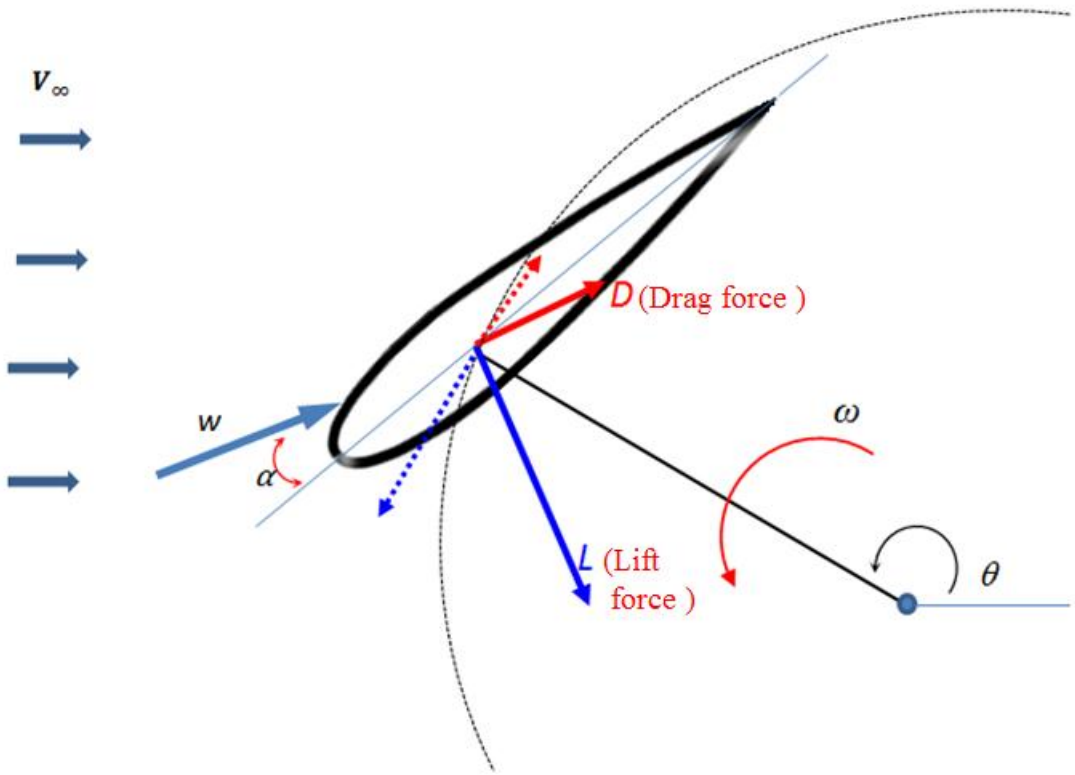

Figure 2-5 Lift and drag force on the blade rotor

2.3 Angle of attack of rotor blade

2.3.1 Angle of attack of Darrieus rotor blade wind turbine

Rotor blades of Darrieus wind turbine have variation of angle of attack in one revolution experience. The variation of angle of attack is depending on three factors; induced velocity, tip speed ratio due to angular velocity of rotor blade, and blade position relative to azimuthal angle. Figure 2-6 show two different angle of attack due to variable pitch and tip speed ratio effects.

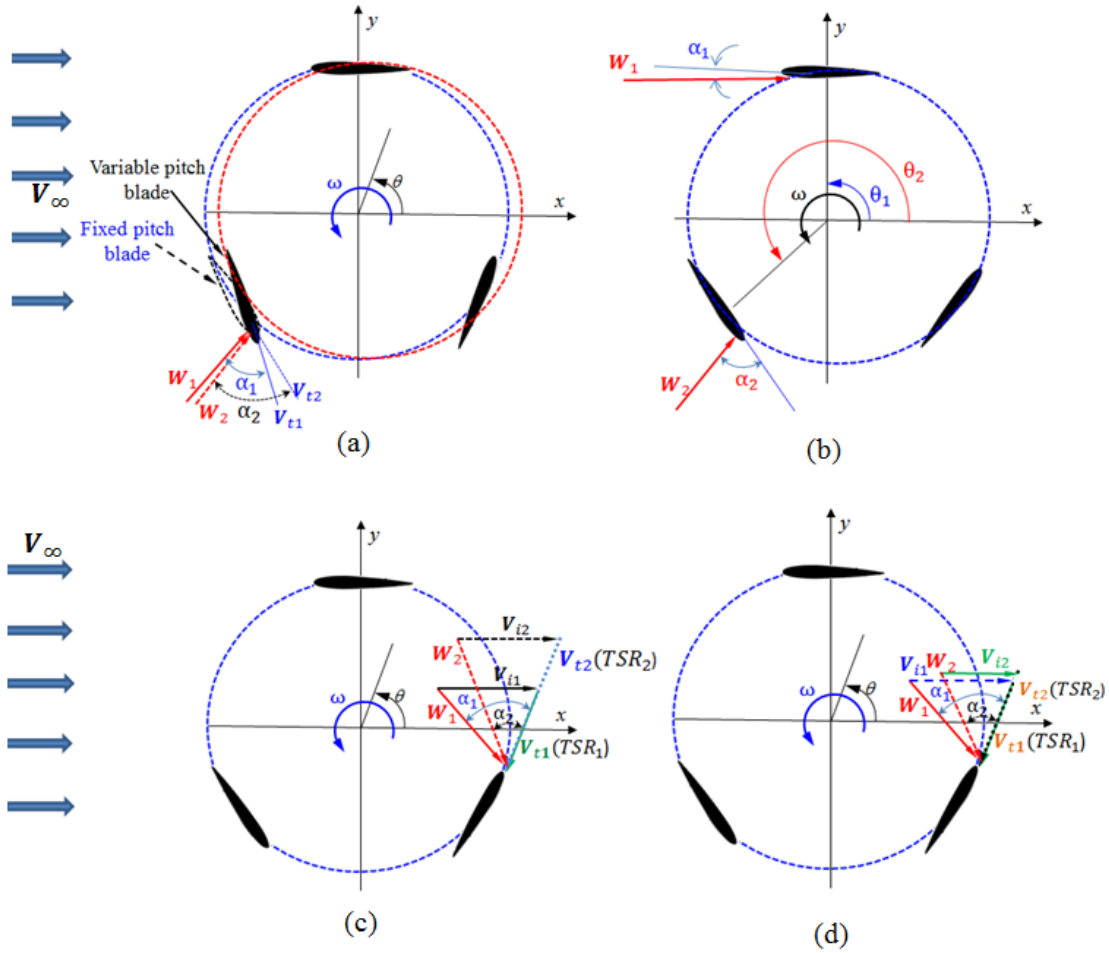

Figure 2-7 Angle of attack of blade rotor types influence by a. pitch angle, b. azimuth angle, c. tip speed ratio, and d. wake effect

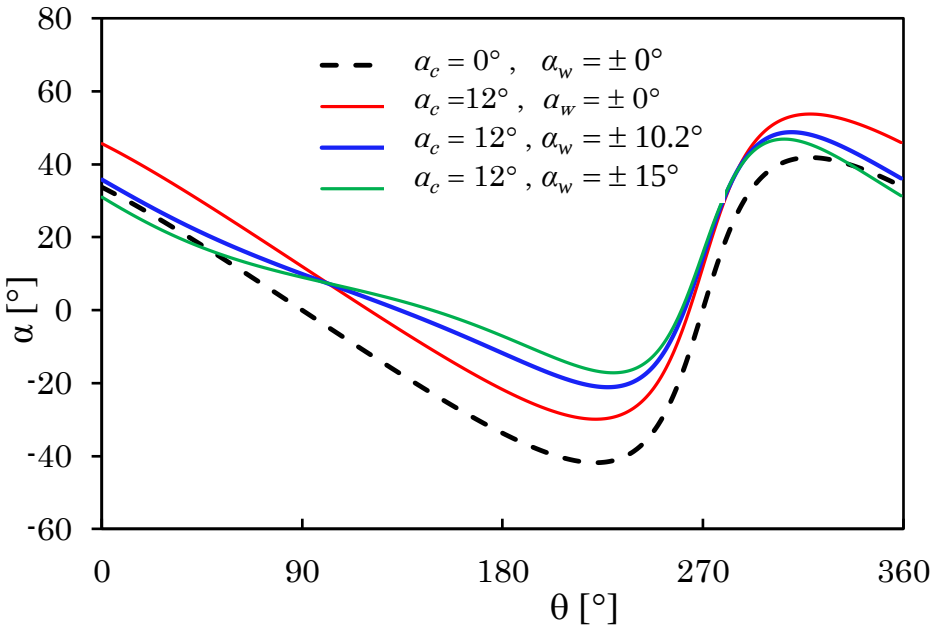

Figure 2-8 Pitch angle and angle of attack

2.3.2 Angle of attack of Orthopter rotor blade

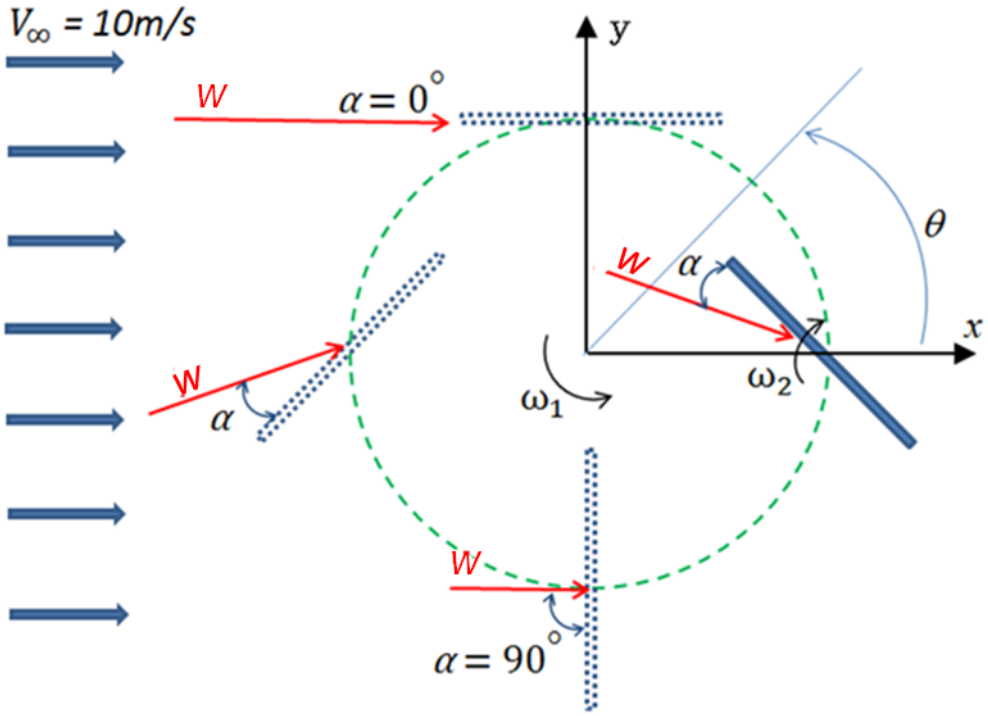

Figure 2-9 Blade position at various azimuth angle corresponding to AoA

Chapter 3 Numerical Simulation Method of VAWTs

3.1 Momentum theory base model

There are many different momentum models such as Blade Element/Momentum or BEM model. By applied Bernoulli's equation, the momentum models are based on calculation of flow velocity through turbine by equating the streamwise aerodynamic force on the blades with the rate of change of momentum of air, which is equal to the overall change in velocity times the mass flow rate. , the average pressure difference across the rotor is equivalent with the force. These models are become invalid for high tip speed ratios and high rotor solidities because the momentum equations in these particular cases are inadequate [Paraschivoiu, 2002, Islam, 2008].

There are two type of streamtube models which, i.e. single streamtube and double streamtube model. In streamtube models the induced axial velocity is calculated at the rotor by equating the time-average force on the blade to the mean momentum flux through a streamtube of fixed location and dimensions. Aerodynamic forces are calculated from local angles of attack and local relative velocities, using airfoil lift and drag coefficients which may include post-stall behavior. Both of single and double streamtube were splitting in a number streamtubes, resulting in the multiple streamtube models. These models were eventually combined in the Double Multiple Streamtube (DMS) model. One disadvantage of this model is that the interference factors are fixed for the upwind and downwind side, as such it's cannot be adjusted for each streamtube. By modifying the DMS model this is made possible.

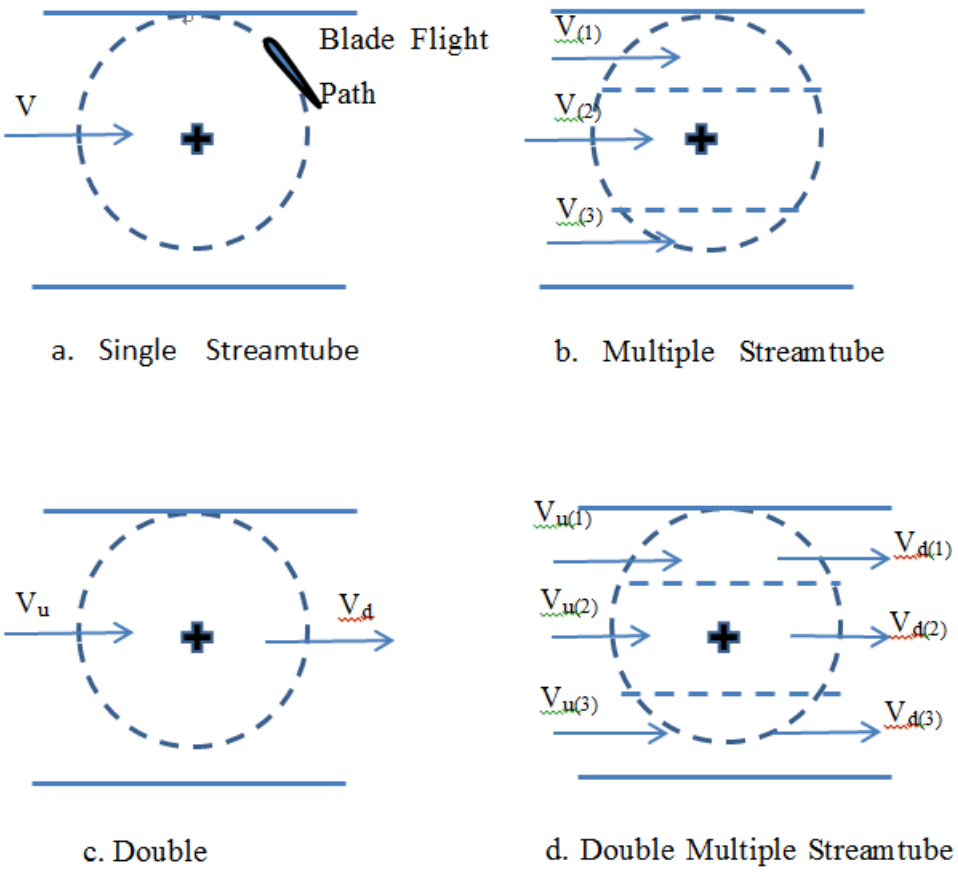

Figure 3-1 Single and Double multiple streamtube

3.2 Computational Fluid Dynamics base model

3.2.1 Equation of Conservation Law

Computational fluid dynamics (CFD) is numerical process to predicting fluid flow phenomena, heat and mass transfer by solving the mathematical equations. In the numerical simulation of wind turbines, the governing equations are applied include the following two conservation laws of physics:

– Continuity or mass conservation.

– Momentum conservation from Newton's second law application.

There are four underlying principal of turbulence modeling which i.e. Reynolds (Ensemble) Averaging to applied on VAWTs simulations. In Reynolds averaging, the solution variables in the instantaneous (exact) Navier-Stokes equations are decomposed into the mean (ensemble-averaged or time-averaged) and fluctuating components. For the velocity components:

Equation 3-1

$$u_i = \bar{u}_i + u_i'$$

Where $\bar{u}_i$ and u_i' are the mean and fluctuating velocity components (i= *1,2,3*) respectively.

Similar, for pressure, energy, and other scalar quantities:

Equation 3-2

$$\phi = \bar{\phi} + \phi'$$

Where ϕ denotes a scalar such as pressure, energy, or species concentration and $\bar{\phi}\, and\, \phi'$ are defined the mean and fluctuating of ϕ respectively. Substituting of this equation for the flow variables into the instantaneous continuity and momentum equations and taking a time average yields the ensemble-averaged momentum equations. For two dimensional and incompressible flows the conservation of mass and momentum can be written in in Cartesian tensor form as;

Equation 3-3

$$\frac{\partial u_j}{\partial x_j} = 0 \quad \rightarrow \frac{\partial u}{\partial x} + \frac{\partial v}{\partial y} = 0$$

Equation 3-4

$$\frac{\partial u_i}{\partial t} + u_j \frac{\partial u_i}{\partial x_j} = -\frac{1}{\rho}\frac{\partial p}{\partial x_i} + \frac{\mu}{\rho}\frac{\partial^2 u_i}{\partial x_j \partial x_j} - \frac{\partial}{\partial x_j}\left(\overline{u_i' u_j'}\right) + g_i$$

Equation 3-3 and 3-4 are called Reynolds-averaged Navier-Stokes (RANS) equation. Where $\overline{u_i' u_j'}$ is the Reynolds stresses and its must be modeled in order to close equation 3-4.

3.2.2 Renormalization Group k-ε turbulence model

A turbulence model is a computational procedure to close the system which allows the calculation of *mean flow* equations (Patel, 2014). Two-equation turbulence models allow the determination of both, a turbulent length and time scale by solving two separate transport equations. The RNG-based turbulence model is derived from the

instantaneous Navier-Stokes equations, using a mathematical technique called "renormalization group" (RNG) methods. It was derived using a statistical technique. The RNG model is a model based on model transport equations for the turbulence kinetic energy (k) and its dissipation rate (ε). The model transport equation for is derived from the exact equation, while the model transport equation for was obtained using physical reasoning and bears little resemblance to its mathematically exact counterpart (Nazary, 2011). The RNG model has similar form to the standard model, but includes the following refinements such as; additional term in equation, provides an analytical formula for turbulent Prandtl numbers and derived differential for effective viscosity for low-Re number (ANSYS FLUENT 12.0 Theory Guide). The RNG model has improves the accuracy for rapidly strained flows and swirling flows. Therefore, the RNG model more accurate and reliable for a wider class of flows than the standard model.

The turbulence kinetic energy, k, and its rate of dissipation, ε, are obtained from following equation;

Equation 3-5

$$\frac{\partial k}{\partial t} + u_j \frac{\partial k}{\partial x_j} = -\frac{1}{\rho}\frac{\partial p}{\partial x_j}\left(\alpha_k \mu_{\text{eff}} \frac{\partial k}{\partial x_j}\right) + \frac{G_k}{\rho} - \varepsilon,$$

Equation 3-6

$$\frac{\partial \varepsilon}{\partial t} + u_j \frac{\partial \varepsilon}{\partial x_j} = -\frac{1}{\rho}\frac{\partial p}{\partial x_j}\left(\alpha_\varepsilon \mu_{\text{eff}} \frac{\partial \varepsilon}{\partial x_j}\right) + \frac{1}{\rho} C_{\varepsilon l} G_k \frac{\varepsilon}{k} - \left(C_{\varepsilon 2} + \frac{C_\mu \rho \eta^3 \left(1 - {}^{\eta}/_{\eta_0}\right)}{1 + \beta \eta^3}\right)\frac{\varepsilon^2}{k}$$

The term of G_k is the production of turbulence kinetic energy and use for the standard, RNG, and Realizable k- ε models. The term of G_k may be defined as

Equation 3-7

$$G_k = -\rho \overline{u_i' u_j'} \frac{\partial u_j}{\partial x_i}$$

To evaluate G_k in manner consistent with the Boussinesq hypothesis

$$G_k = \mu_t S^2$$

Where S is the modulus of the mean rate-of-strain tensor, defined as

$$S \equiv \sqrt{2 S_{ij} S_{ij}} \qquad S_{ij} \equiv \frac{1}{2}\left(\frac{\partial U_j}{\partial x_i} + \frac{\partial U_i}{\partial x_j}\right)$$

The scale elimination procedure in RNG theory results in a differential equation for turbulent viscosity;

Equation 3-8

$$d\left(\frac{\rho^2 k}{\sqrt{\varepsilon\mu}}\right) = 1.72\,\frac{\hat{v}}{\sqrt{\hat{v}^3 - 1 + C_v}}\,d\hat{v}$$

Where

$$\hat{v} = \frac{\mu_{eff}}{\mu}$$

in the high-Reynolds number limit, equation 3-9 gives ;

$$\mu_t = \rho C_\mu \frac{k^2}{\varepsilon}$$

with C_μ = 0.0845, $C_{1\varepsilon} = 1.42$ $C_{2\varepsilon} = 1.68$ $\sigma_k = 1.0$ $\sigma_\varepsilon = 1.2$ derived using RNG theory.

3.2.3 Realizable *k*-ε turbulence model

The RNG *k*-ε model and the Realizable *k*-ε model has modified compare the standard *k*-ε model to improve the performance. The realizable *k*-ε model contains an alternative formulation for the turbulent viscosity. A modified transport equation for the dissipation rate, ε, has been derived from an exact equation for the transport of the mean-square vorticity fluctuation the realizable *k*-ε model, consider combining the Boussineq relationship and the eddy viscosity definition to obtain the following expression for the normal Reynolds stress in an incompressible strained mean flow:

Equation 3-10

$$\overline{u^2} = \frac{2}{3}k - 2v_t\frac{\partial U}{\partial x}$$

Both the realizable and RNG *k*-ε models have shown substantial improvements over the standard *k*-ε model where the flow features include strong streamline curvature, vortices, and rotation. Since the model is still relatively new, it is not clear in exactly which instances the realizable *k*-ε model consistently outperforms the RNG model. However, initial studies have shown that the realizable model provides the best performance of all the *k*-ε model versions for several validations of separated flows and flows with complex secondary flow features (Wang, 2011, ANSYS FLUENT 12.0 Theory

Guide, 2009).

One limitation of the realizable *k-ε* model is that it produces non-physical turbulent viscosities in situations when the computational domain contains both rotating and stationary fluid zones (for example, multiple reference frames, rotating sliding meshes). This is due to the fact that the realizable *k-ε* & model includes the effects of mean rotation in the definition of the turbulent viscosity.

The modeled transport equations for and in the realizable *k-ε* model are;

Equation 3-11

$$\frac{\partial k}{\partial t} + u_j \frac{\partial k}{\partial x_j} = -\frac{1}{\rho}\frac{\partial}{\partial x_j}\left[\left(\mu + \frac{\mu_t}{\sigma_k}\right)\frac{\partial k}{\partial x_j}\right] + \frac{G_k}{\rho} - \varepsilon,$$

Equation 3-12

$$\frac{\partial \varepsilon}{\partial t} + u_j \frac{\partial \varepsilon}{\partial x_j} = -\frac{1}{\rho}\frac{\partial}{\partial x_j}\left[\left(\mu + \frac{\mu_t}{\sigma_\varepsilon}\right)\frac{\partial \varepsilon}{\partial x_j}\right] + C_1 S_\varepsilon - C_2 \frac{\varepsilon^2}{k + \sqrt{v\varepsilon}}\varepsilon + C_{1\varepsilon}\frac{\varepsilon}{k}\, C_{3\varepsilon} G_b + S_\varepsilon$$

where,

$$C_1 = \max\left[0.43, \frac{\mu}{\mu + 5}\right], \mu = S\frac{k}{\varepsilon}, S = \sqrt{2S_{ij}S_{ij}}$$

Modeling the turbulent viscosity

$$\mu_t = \rho C_\mu \frac{k^2}{\varepsilon}$$

The model constants are;

C_2 = 1.9, $C_{1\varepsilon} = 1.44$ $\sigma_k = 1.0$ $\sigma_\varepsilon = 1.2$

3.2.4 Shear-Stress Transport (SST) *k-ω* turbulence model

Low Reynolds number modifications have been proposed by Wilcox for the *k-ω* model. It is important to note that all *k-ω* models can be integrated through the viscous sub layer without these terms. The terms were mainly added to reproduce the peak in the turbulence kinetic energy observed in DNS data very close to the wall. In addition, these terms affect the laminar turbulent transition process. The low-Reynolds number terms can produce a delayed onset of the turbulent wall boundary layer and constitute therefore a very simple model for laminar-turbulent transition. The shear-stress transport (SST) *k-ω* model was developed by Menter to effectively blend the robust and accurate formulation of the *k-ω* model in the near-wall region with the free-stream independence of the *k-ω* model in the far field. To achieve this, the model is converted

into a formulation. The SST *k-ω* model is similar to the standard model, but includes the following refinements ((ANSYS FLUENT 12.0 Theory Guide, 2009). The standard *k-ω* model and the transformed *k-ω* model are both multiplied by a blending function and both models are added together. The blending function is designed to be one in the near-wall region, which activates the standard *k-ω* model, and zero away from the surface, which activates the transformed model.

These features make the SST *k-ω* model more accurate and reliable for a wider class of flows (for example, adverse pressure gradient flows, airfoils, transonic shock waves) than the standard *k-ω* model.

Transport equation for the SST *k-ω* model;

Equation 3-13

$$\frac{\partial k}{\partial t} + u_j \frac{\partial k}{\partial x_j} = P_k - \beta^* k\omega + \frac{\partial}{\partial x_j}\left[(v + v_k v_T)\frac{\partial k}{\partial x_j}\right]$$

Equation 3-14

$$\frac{\partial \omega}{\partial t} + u_j \frac{\partial \omega}{\partial x_j} = \alpha S^2 - \beta\omega^2 + \frac{\partial}{\partial x_j}\left[(v + v_\omega v_T)\frac{\partial \omega}{\partial x_j}\right] 2(1 - F_1)\sigma\, \omega^2 \frac{1}{\omega}\frac{\partial k}{\partial x_i}\frac{\partial \omega}{\partial x_i}$$

The model constants are

$a_1 = 0.31,\ \beta_{i,1} = 0.075\quad \beta_{i,2} = 0.0828\quad \sigma_{k,1} = 1.176\quad \sigma_{\omega,1} = 2.0\quad \sigma_{k,2} = 1.0$

$\sigma_{\omega,2} = 1.168$

3.3 Geometry and Meshing

The geometry and meshing are important in CFD which are the flow solved. The geometry describes the shape of the problem to be analyzed. It has consists of volumes, faces (surfaces), edges (curves) and vertices (points). The grid is needed due to discrete representation of the geometry of the problem and it has cells grouped into boundary zones where boundary conditions are applied. The grid has a significant impact on; rate of convergence, solution accuracy, and CPU time required. The importance of mesh quality which are; grid density, adjacent cell length/volume ratios, skewness, boundary layer mesh, and mesh refinement through adaption that contribute for good solutions. The quality of grid is important for achieved success of the CFD analysis. There are

many different cell/element and grid types in CFD. The cell or element types are; triangular (2D), quadrilateral (2D), prism with quadrilateral based (3D), prism with triangular based (3D), tetrahedron (3D), pyramid (3D), and arbitrary polyhedron (3D). The grid types are; structured grid, unstructured grid, and hybrid grid. The structured grid, grid lines must pass all through domain. The hybrid grid is combination of different grid types such as; triangles and quadrilaterals in 2D, tetrahedra, prisms and pyramids in 3D. The hybrid grid can be non-conformal or grids lines don't need to match at block boundaries. The quality of mesh are consists; Skewness, Smoothness (change in size), and Aspect ratio.

3.3.1 Model Geometry of Darrieus Wind Turbine with Variable Pith-Angle Blade Rotor

The Darrieus wind turbine conventional or fixed pitch angle was modified by control mechanism of blade rotor as shown in figure 3-2. There are three links such as; main link, secondary link and eccentric link. The length of links lead to blade pitch angle amplitude and pitch angle offset. The main geometrical features of this turbine are shown in Table. The wind turbine diameter of D (=2R) = 800 mm and a height of turbine rotor h = 800 mm. The length of main and second link set constant equal 0.373 m and 0.365 m respectively for three cases which blade offset pitch angle equal 12 degrees. In case 1, for blade pitch angle amplitude equal zero degrees or fixed pitch angle, the length of eccentric link equal zero. In case 2, for blade pitch amplitude equal ten point two degrees, the length of eccentric link equal 0.015 m and the last case, for blade pitch amplitude equal fifteen degrees, the length of eccentric link equal 0.022 m.

. The section of the VAWT that was analyzed was the symmetrical airfoil of its NACA0018 blade, which had a maximum lift coefficient $C_{L\max}$ at an angle of attack of $\alpha \approx 15°$ and a maximum lift-to-drag ratio C_L/C_D at an angle of attack of $\alpha \approx 5.5°$. The rotor of the VAWT was composed of three blades with a chord length of c = 200 mm and a main shaft with a diameter of 0.06 m. The solidity was σ (= $nc/\pi D$) = 0.239, which is defined as the ratio of the total blade area (nc) to the circumference area (πD). Figure 3-3 shows a top view of the VAWT and its variable-pitch mechanism, which consists of a four-bar linkage with an adjustable eccentric link l_e. This turbine had an eccentric rotational point O_e that was different from the main rotational point O. Point P_1 is near the leading edge of the blade, and point P_2 is near the trailing edge of the blade. The

angle between the main-link (l_m) and the x - axis is the azimuthal angle (θ). This mechanism is able to vary the pitch angle α_p according to the rotation of the main link without utilizing the actuators as shown figure 3-4. The geometry of the pitch angle (α_p) is the sum of the blade offset angle (α_c) and the blade pitch angle amplitude (α_w). The optimum blade offset pitch angle was chosen from the experimental results to be $\alpha_c = 11.9°$. The blade pitch angle amplitude was changed from $\alpha_w = \pm 0°$ to $\pm 15.0°$ by increasing the length of the eccentric link from l_e = 0 m to 22 mm.

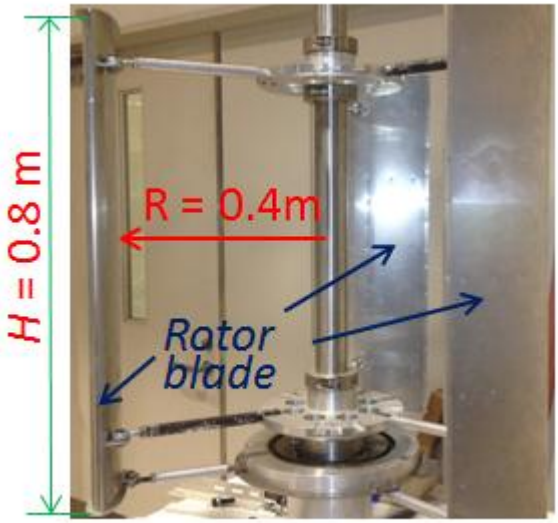

Figure 3-2 Darrieus wind turbine with variable pitch angle blade

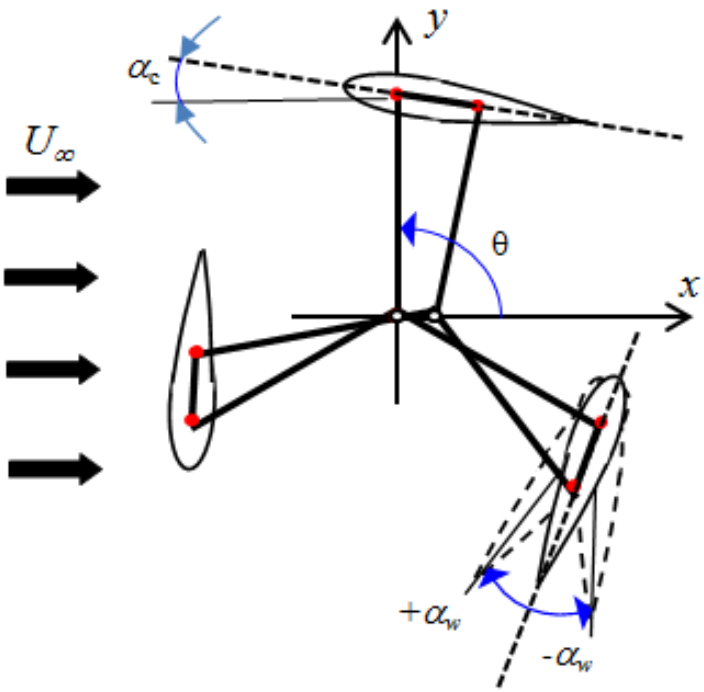

Figure 3-3 Top view of Darrieus variable pitch angle blade

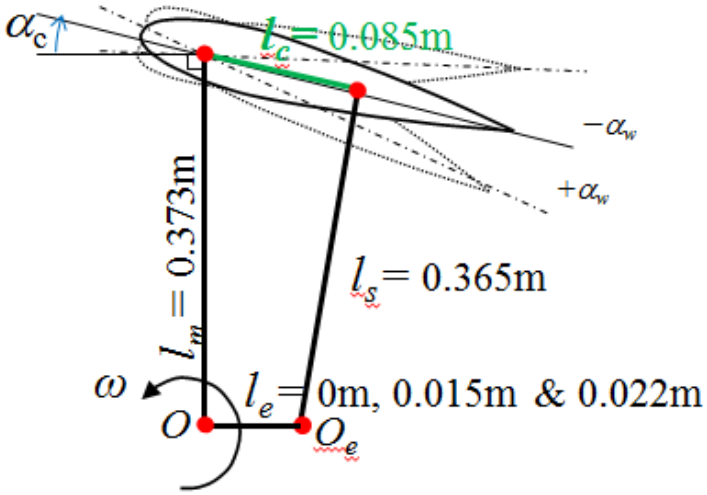

Figure 3-4 Schematic of blade linkage

3.3.2 Model Geometry of Orthopter Wind Turbine with Variable Pith-Angle Blade Rotor

The orthopter wind turbine is combination between a drag-type and a lift-type vertical axis wind turbine which each blade has a rotating movement around its own axis and turbine's shaft. The orthoptera is insects which have hind wings and chewing mouthparts. The pitch of the blades was controlled by using a chain and sprockets arrangement to ensure that the blades rotated around their own axis by 360 degrees during the each two full revolution of the main rotor. Figure 3-5 show the orthopter wind turbine. There are two configuration of orthopter wind turbine which i.e., the orthopter wind turbine with shaft and without shaft.

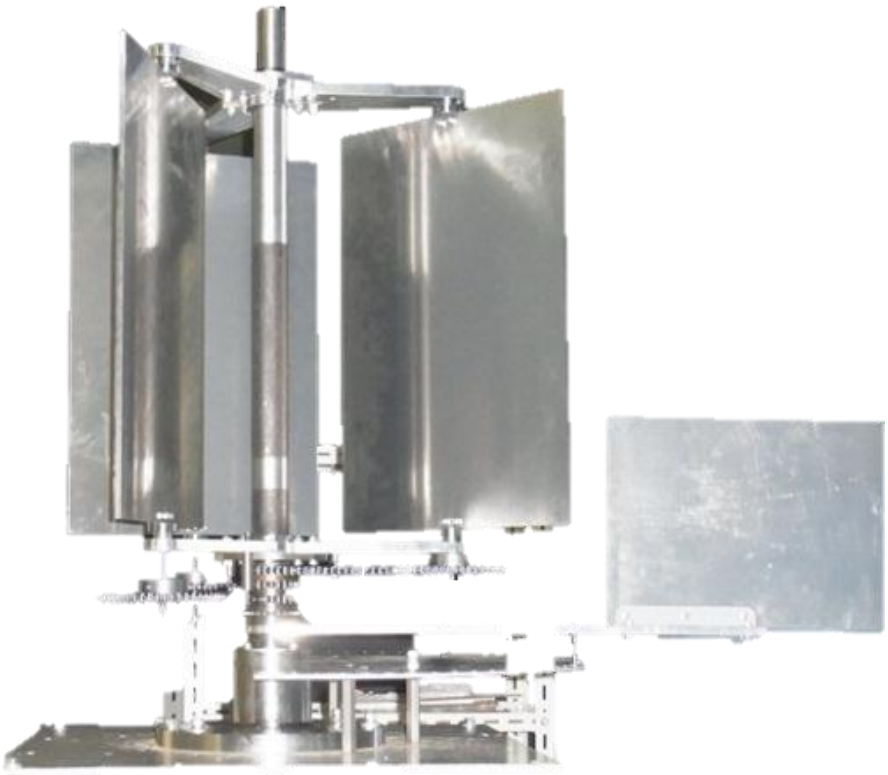

Figure 3-5 The Orthopter wind turbine

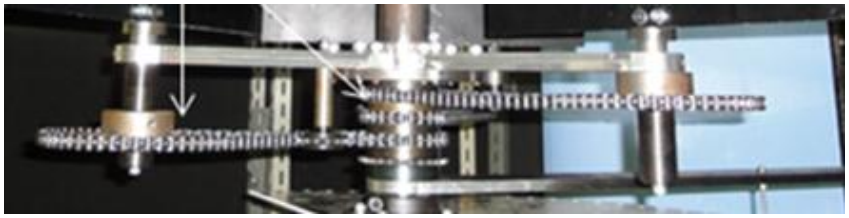

Figure 3-6 Side view of control mechanism

Figure 3-7 Top view of control mechanism

The figure 3-6 and 3-7 show side and top view of control mechanism respectively. The control mechanism consist gear and sprocket which gear have 1: 2 ratio to control rotation of blade relative main shaft rotation.

3.3.3 Meshing of Darrieus Wind Turbine with Variable Pith-Angle Blade Rotor

The meshing of Darrieus wind turbine composed of three part which are; outside of rotor, rotor, and around blade. The two-dimensional computational domain, boundary conditions, and the mesh structure are shown in Figs.3-8 – 3-9. The outside of rotor meshing had a radius of 24*R*, and the inlet and outlet boundary conditions were placed upstream and downstream of the rotor, respectively. The computational domain consisted of three mesh zones, i.e., one fixed sub-domain outside the rotor, one dynamic sub-domain around the rotor with a radius of 3*R*, and three dynamic sub-domains around the blades with a diameter of 3*c* and an equal spacing of 120°. The mesh interfaces consist of one mesh interface around the rotor and three around blades 1, 2, and 3. A dynamic mesh technique was used for this simulation. The dynamic meshes around the rotor and blades rotate according to the TSR, while the mesh on the exterior of the rotor remains stationary. The fixed sub-domain was meshed using quadrilateral grids, and the dynamic sub-domain around the rotor was meshed using triangular grids. The three dynamic sub-domains around the blades were meshed using a combination of triangular grids and quadrilateral grids, especially near the surfaces of the blades. In order to construct a high density mesh on the surfaces of the blades, the layers of the cells were generated by using an inflation tool that had a growth rate of 1.2. The distance of the first layer was 0.01 mm, and $y^+ < 1$ was obtained. The fixed sub-domain on exterior side of the rotor had 116,808 elements, the sub-domain around the rotor had 21,680 elements, and the three dynamic sub-domains around the blades had 66,389 elements. The total number of elements was about 3.37×10^5.

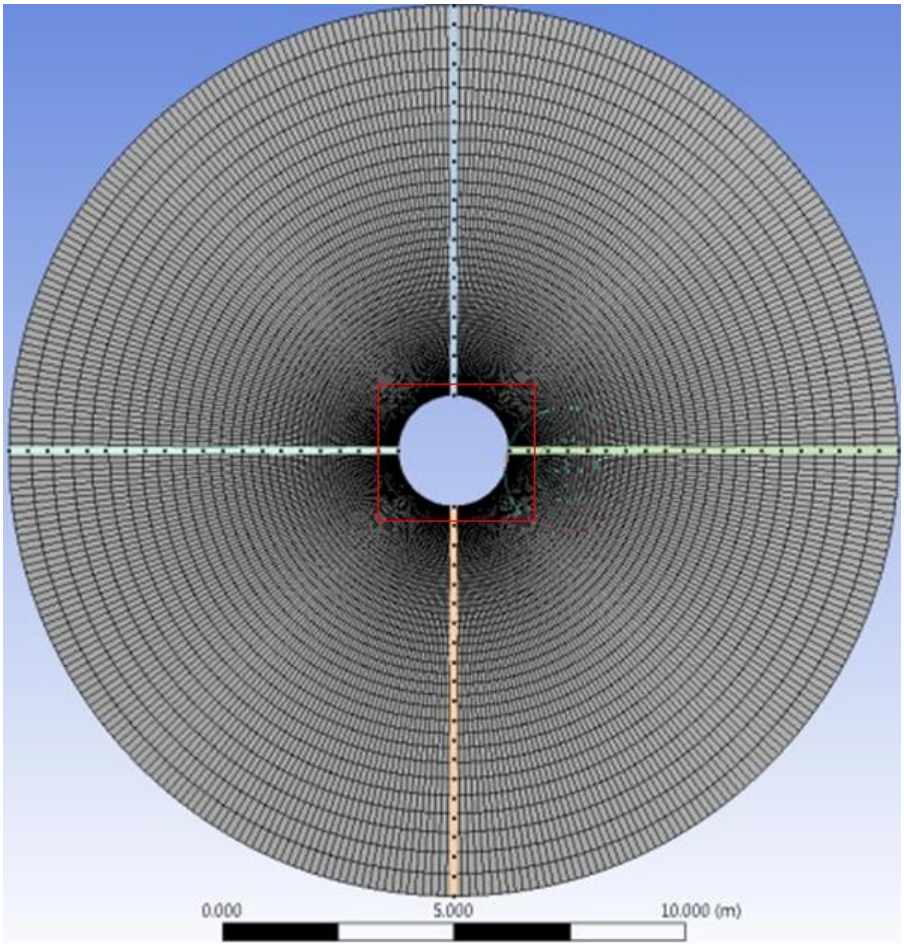

Figure 3-8 Meshing outside of the rotor

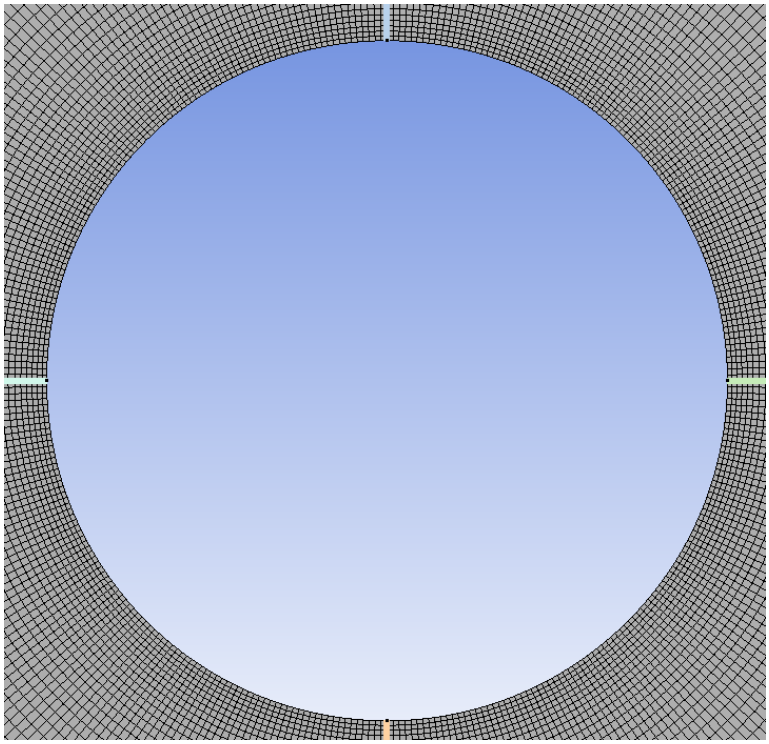

Figure 3-9 Structure of meshing outside of the rotor

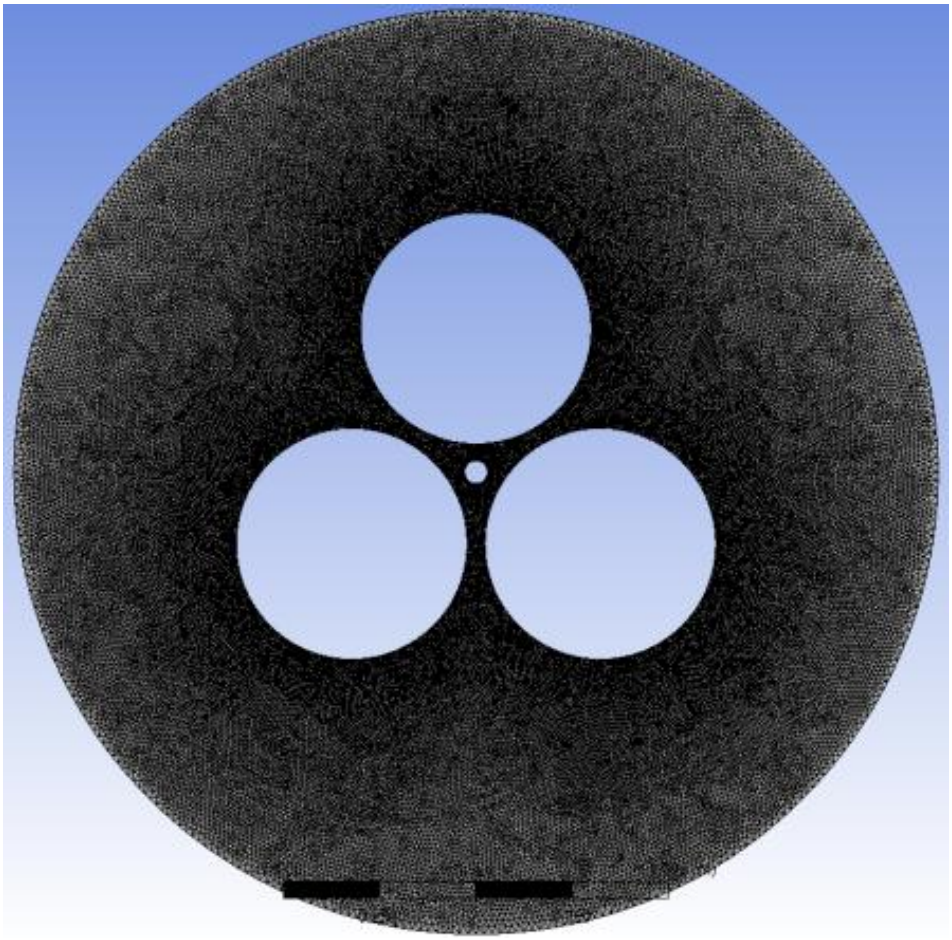

Figure 3-10 Meshing of rotation

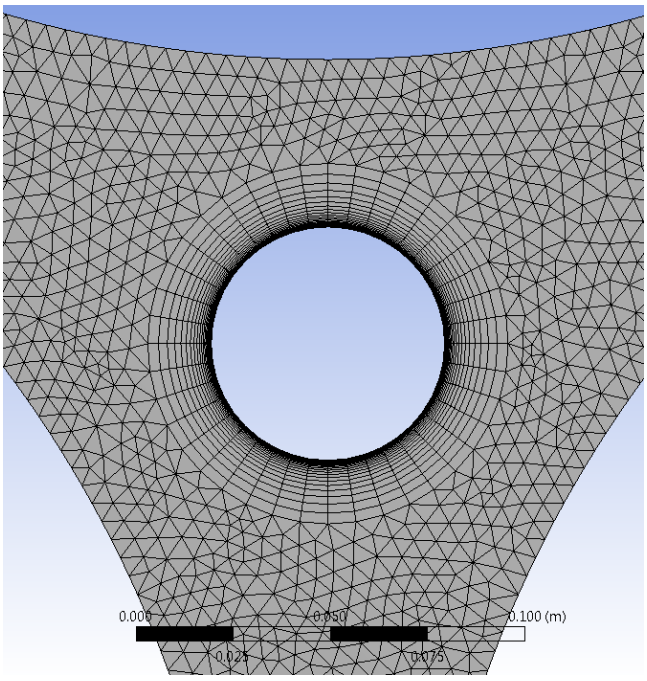

Figure 3-11 Structure of meshing rotation and fine grid near wall of shaft

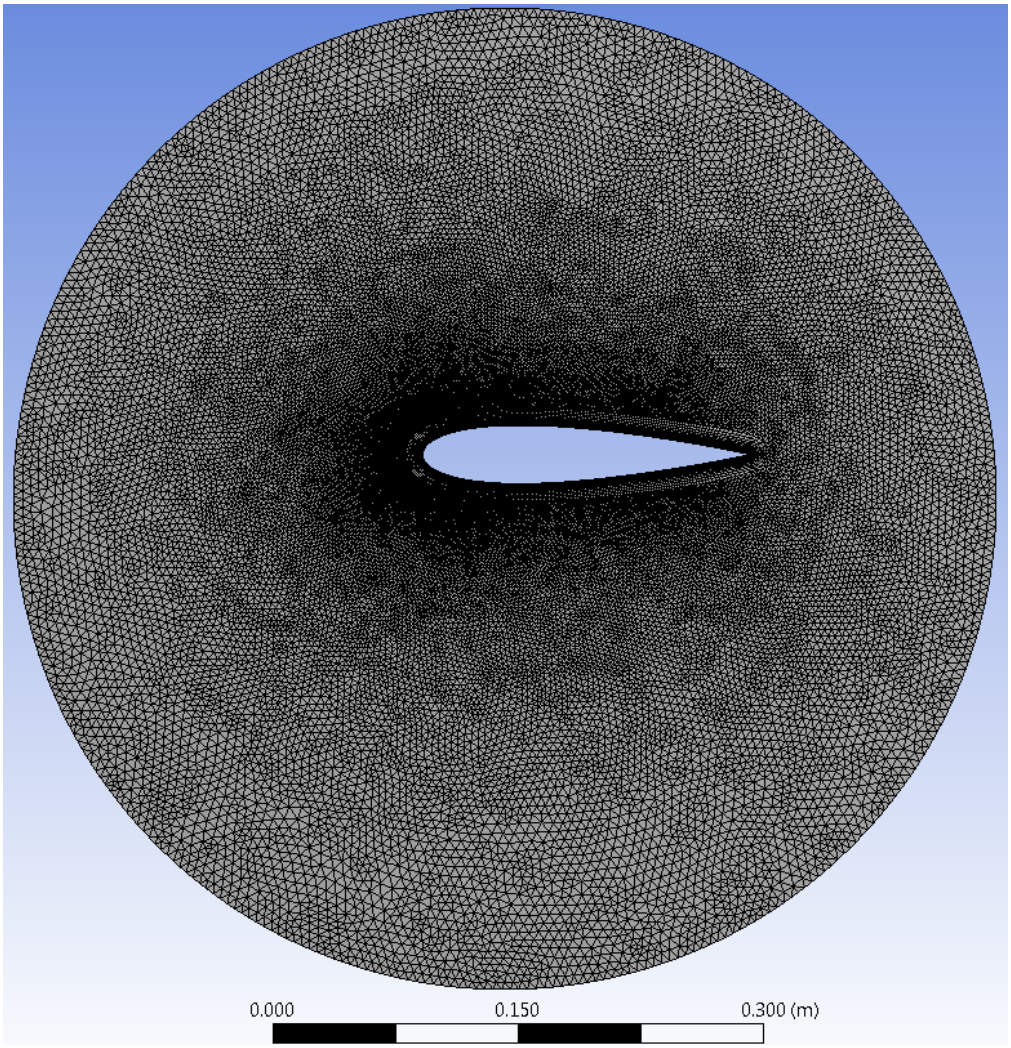

Figure 3-12 Meshing of around blade

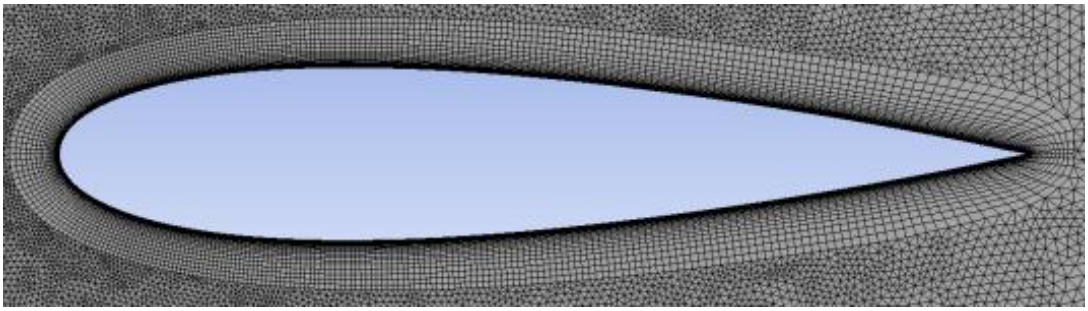

Figure 3-13 Structure meshing near wall blade

3.3.4 Meshing of Orthopter Wind Turbine with Variable Pith-Angle Blade Rotor

The meshing of Orthopter wind turbine composed of three part which are; outside of rotor, rotor, and around blade. The structure of outside the rotor grid is quadrilateral. the structure of rotation and around blade are combine structure and unstructured grid. The structure grid of rotation and around blade are on the wall in order refine grid or high dense. There are three type of rotation which are it's consist two, three and four hole that around blade lies. The computational domain consists of three mesh zones. one fixed sub-domain outside the rotor, one dynamic sub-domain around the rotor, and three dynamic sub-domains around the blades with equal spacing of 180°, 120°, and 90° for number of blade n=2, n=3, and n=4 respectively. The rotation of the four dynamic sub-domains can be controlled independently by a user-defined function (UDF), which is programmed in *C++* code.

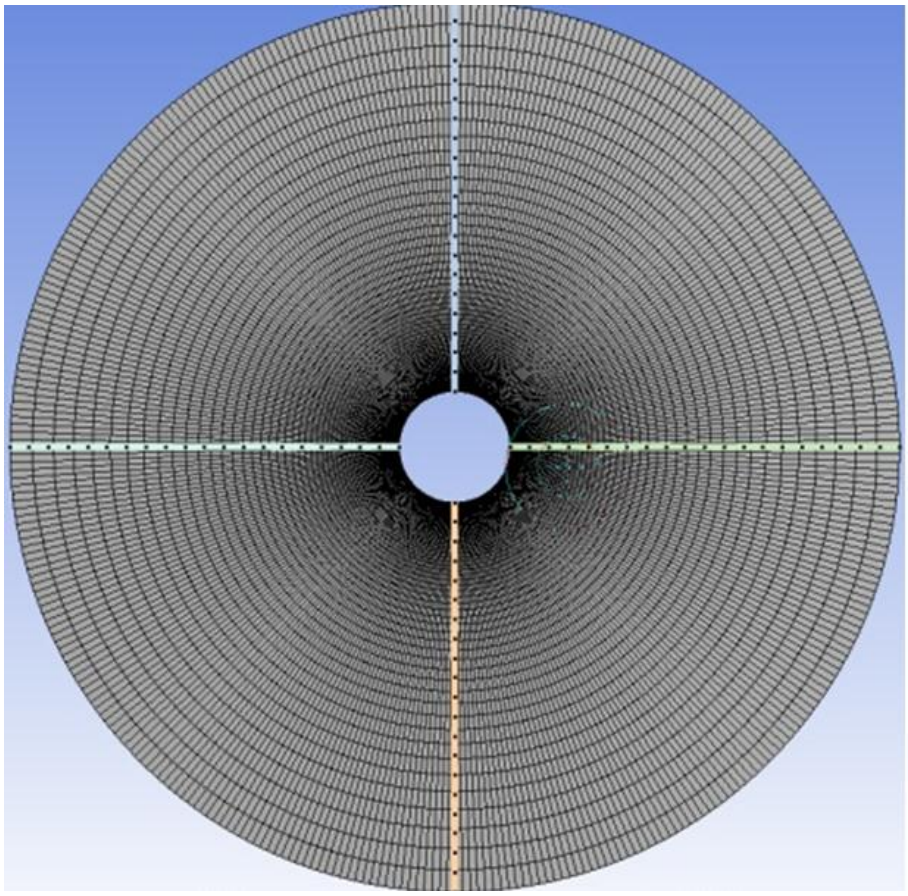

Figure 3-14 meshing of outside rotor

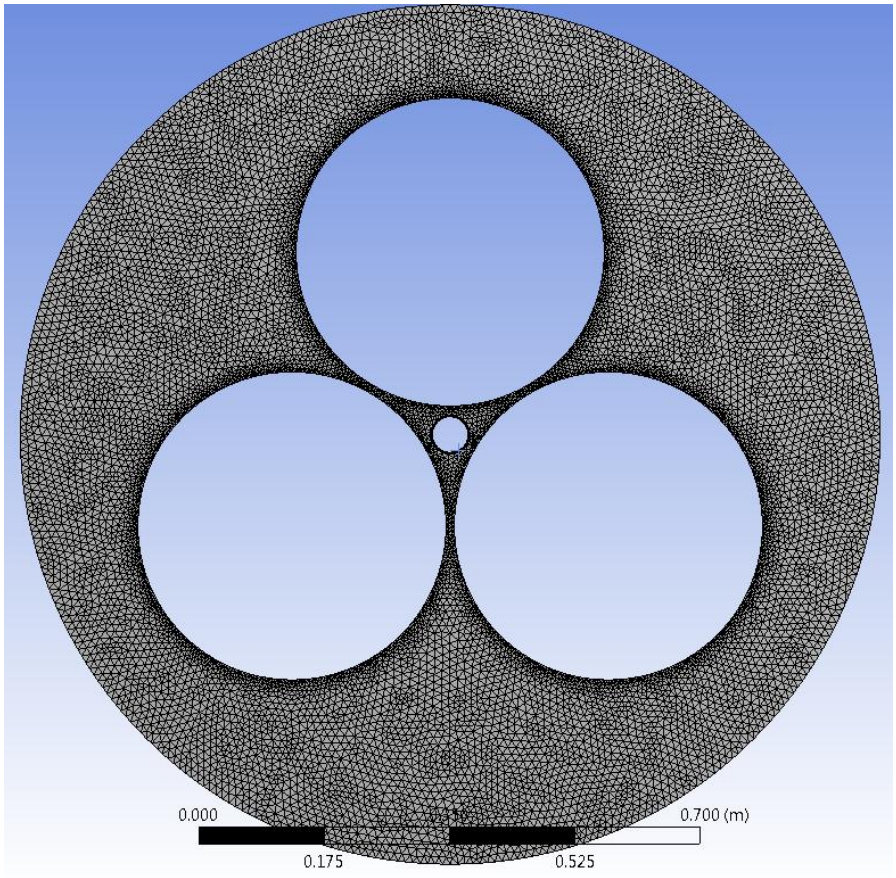

Figure 3-15 meshing of rotation for three blades

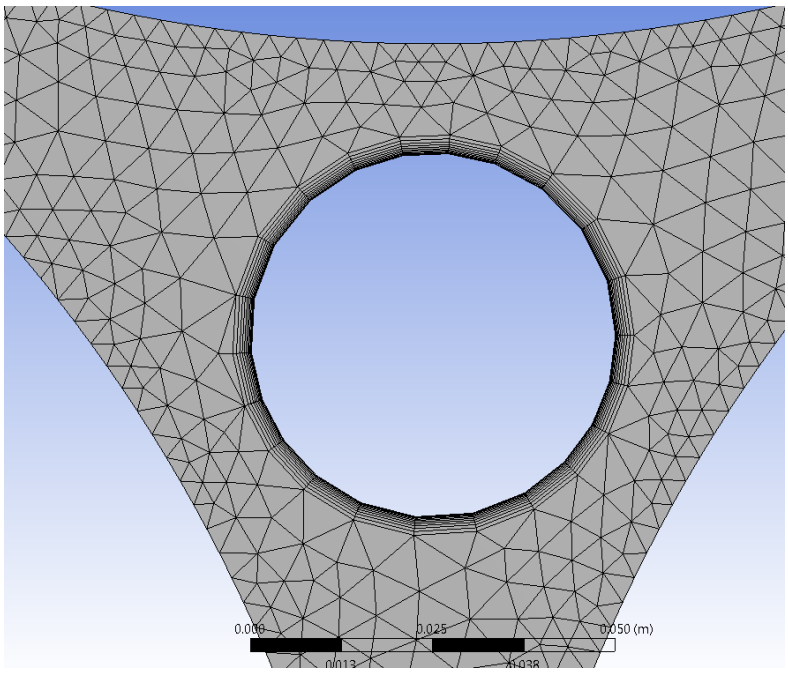

Figure 3-16 Structure of near wall shaft on rotation blade

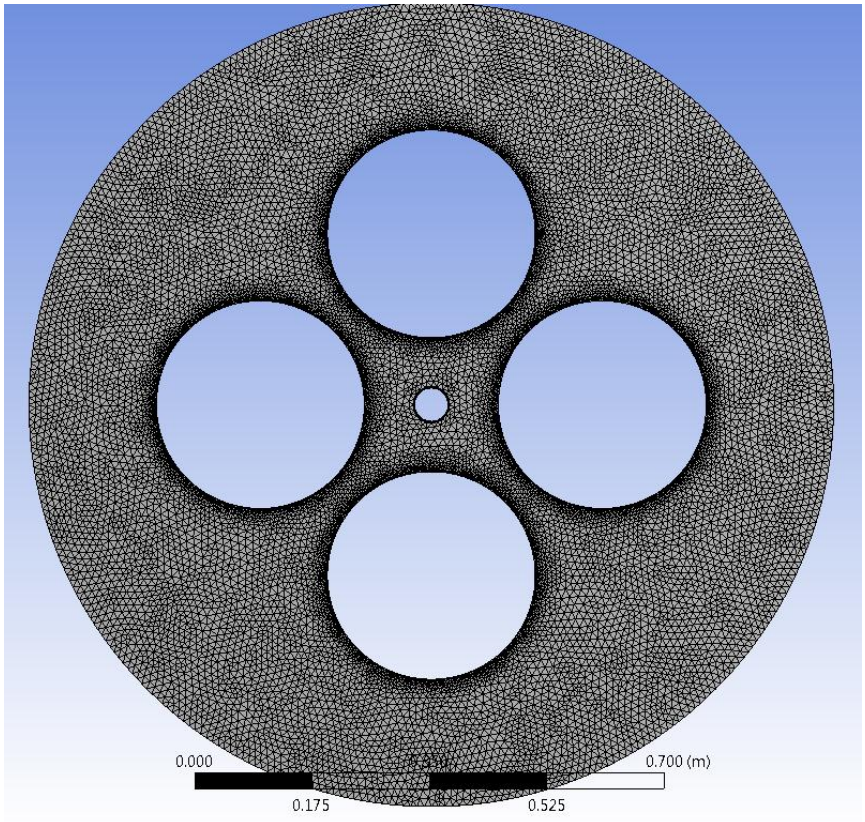

Figure 3-17 meshing of rotation for four blades

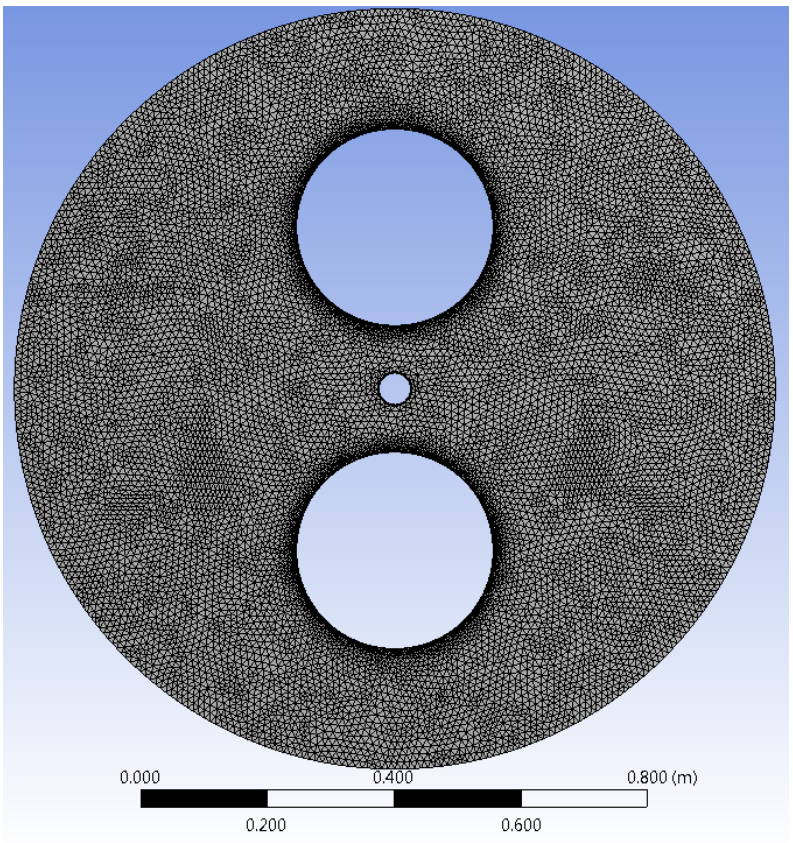

Figure 3-18 meshing of rotation for two blades

3.4 Solver and Setting

The ANSYS Fluent programs are based on finite volume method. In the finite volume method, the solution domain is subdivided into a finite number of small control volumes (cells) by a grid. The grid defines the boundaries of the control volumes while the computational node lies at the center of the control volume (Leifur Leifsson, 2011). The value of the integrand is not available at the control volume faces and is determined by interpolation as seen Fig 3-19

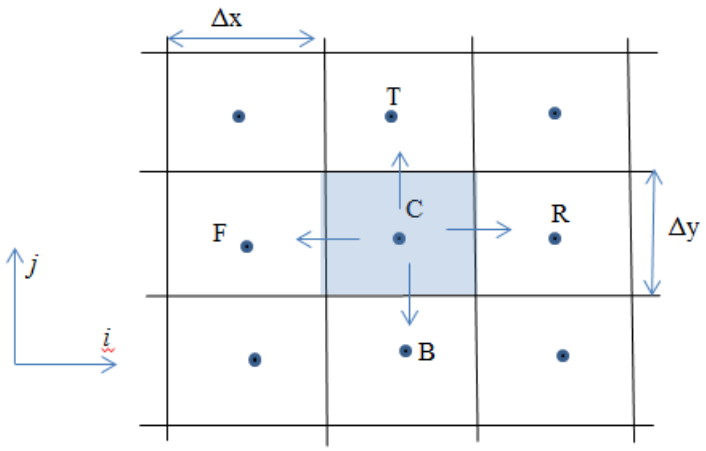

Figure 3-19 control volume face

The conservation equations used in CFD can be discretized involving the transport in a flow field. The discretization is this equation convert to a solveable algebraic form. The simple discretization is using the balance over the control volume. This contains values at the faces, which need to be determined from interpolation from the values at the cell centers.

The simplest way to determine the values at the faces is by using first order upwind differencing and followed by second order upwind differencing. In the numerical scheme, faces values of ϕ or $\frac{\partial \phi}{\partial x}$ are found by making assumptions about variation of ϕ between cell centers [Patankar & Spalding, 1972], which is based on a semi-implicit time discretization, or the QUICK scheme, which uses a higher order discretization [Leonard, 1979]

The different schemes can be classification;

- First-order upwind scheme.
- Central differencing scheme.

- Power-law scheme.
- Second-order upwind scheme.
- QUICK scheme.
- Third order MUSCL

First order upwind scheme;

The simplest numerical scheme is first order upwind. The value of ϕ at the face assume is the same as the cell centered value in the cell upstream of the face.

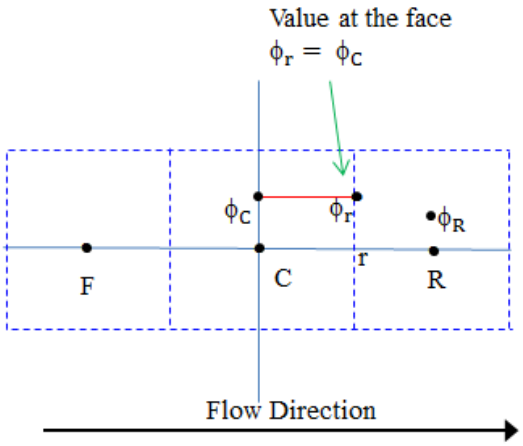

Figure 3-20 First order upwind scheme

Central differencing scheme;

Determine the value of ϕ at the face by linear interpolation between the cell centered values.

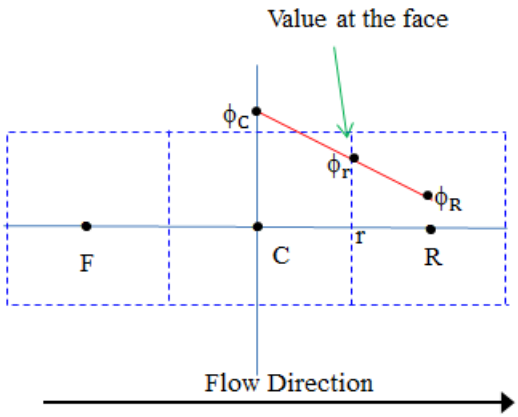

Figure 3-21 Central differencing scheme

Power law scheme;

This is based on the analytical solution of the one-dimensional convection-diffusion equation. The face value is determined from an exponential profile through the cell values which approximate with the power law equation:

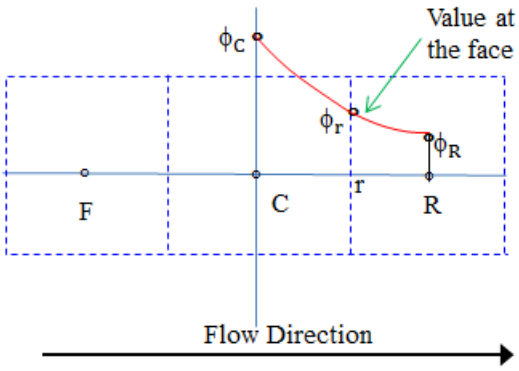

Figure 3-22 Power law scheme

Second-order upwind scheme;

The value of the cell is determined by values in the two cells upstream of the face. This is more accurate than the first order upwind scheme.

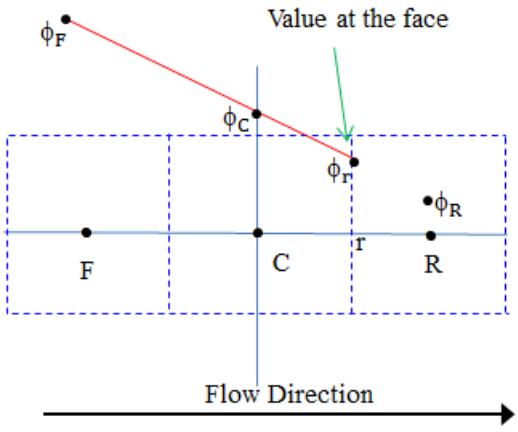

Figure 3-23 Second order upwind scheme

QUICK scheme;

QUICK scheme is Quadratic Upwind Interpolation for Convective Kinetics. A quadratic curve is fitted through two upstream nodes and one downstream node.

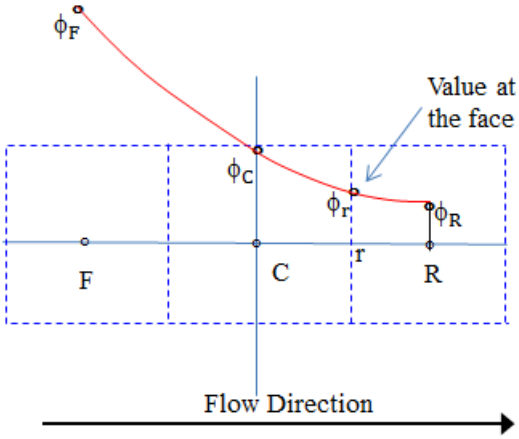

Figure 3-24 QUICK scheme

Pressure - velocity coupling;

The pressure is founded in all three momentum equations. The velocity field also has to satisfy the continuity equation. Even though there is no explicit equation for pressure, there are four equations for four variables, and the set of equations is closed. Therefore, it's called pressure-velocity coupling algorithms. It's is used to derive equations for the pressure from the momentum equations and the continuity equation. The SIMPLE is the default algorithm in most commercial finite volume codes. The improved versions are; SIMPLER (SIMPLE Revised), SIMPLEC (SIMPLE Consistent), and PISO (Pressure Implicit with Splitting of Operators).

Chapter 4 Performance and Aerodynamic on The Fixed and Variable Pitch Straight-Bladed Darrieus Wind Turbines

4.1 Background

There are two types of wind turbines: horizontal axis wind turbines (HAWTs), such as a propeller-type wind turbine, and vertical axis wind turbines (VAWTs), such as the Darrieus wind turbine. The power coefficient of HAWTs is generally larger than that of VAWTs, since the angle of attack of a VAWT blade changes significantly in one revolution. A majority of the large wind turbines that are used for power generation are HAWTs. However, VAWTs have many advantages, such as being omni-directional without needing a yaw control system, having better aesthetics for their integration into buildings, having more efficiency in turbulent environments, and having lower sound emissions (Mertens, 2006; Mewburn-Crook, 1990); therefore, VAWTs are expected to be used in urban areas.

Numerical and experimental studies of VAWTs have been carried out by several researchers, including Castelli et al. (2011), Takao et al. (2008), Howell et al. (2010), Sato et al. (2011) and Chong et al. (2013). Due to the improving performance of VAWTs with straight fixed-pitch blades, Tanaka et al. (2011) have studied the effects of blade profiles (NACA0018, NACA4418 with its camber facing outward, and NACA4418 with its camber facing inward) and setting angle on the performance of a small straight-bladed VAWT. They indicated that the starting performance of the VAWT with the NACA0018 can be further improved by setting the wings at an outward angle of 5 degrees. Yamada et al. (2011) have also studied the effects of the camber and thickness of a blade (NACA0020, 3520, 6518, 6520, 6525, 6530, and 8520) on the performance of a small straight-bladed VAWT. Their report showed the mean and temporal torque variation at any azimuth angle of one and two blades.

As part of a numerical simulation, Chen and Kuo (2013) have studied the effects of pitch angle and blade camber on the unsteady flow characteristics and the performance of a small-size Darrieus wind turbine with the NACA0012, 2412, and 4412 blade profiles. Their results indicated that the self-starting ability and the moment coefficients of

a VAWT that has blades with large cambers (NACA4412) are better than those with the other blades (NACA0012 and 2412). Chen and Zhou (2013) used the SST k-ω model to investigate the aerodynamic performance of a VAWT via a two-dimensional numerical simulation. The results showed the optimum pitch angle for the power coefficient of the VAWT. Aresti et al. (2013) conducted two- and three-dimensional numerical simulations of the performance and flow through a small scale H-type Darrieus wind turbine by using the RNG k-ε, standard k-ε, and standard k-ω turbulence models. The self-starting capabilities of the VAWT were found to increase with the increasing mount angle of attack of the blades. Almohammadi et al. (2013) investigated the mesh independence of the predicted power coefficient of a VAWT with straight blades by employing a two-dimensional numerical simulation. Roh and Kang (2013) investigated the effects of a blade profile, the Reynolds number, and the solidity on the performance of a straight-bladed VAWT by using the numerical procedure of the multiple stream tube method. McNaughton et al. (2014) presented a two-dimensional numerical investigation of a VAWT, which had a high solidity of 1.1, and investigated the effects of the original and a modified version of the SST models for low Reynolds numbers on the flow structure, dynamic stall, and blade-vortex interaction.

The development of VAWTs with variable-pitch straight blades has been carried out to obtain a high starting torque and high efficiency during operating speeds. A few of these VAWTs include the ASI/PINSON wind turbine (Noll and Zvara, 1981), a Giromill wind turbine (Anderson, 1981), a straight-bladed cycloturbine (Nattuvetty and Gunkel, 1982), a VAWT with a self-acting variable pitch system (Pawsey, 1999), and the Orthoptere wind turbine (Shimizu et al., 1997). Kiwata et al. (2010) and Yamada et al. (2012) developed a VAWT with variable-pitch straight blades that have a slight camber using a four-bar linkage without actuators. It was found that the power coefficient of this VAWT is better than that with fixed-pitch blades. Furthermore, this VAWT can direct itself towards the wind, which enables it to utilize the rotational speed control in the turbine via its tail vanes.

4.2 Motivation and Objectives

Due to the phenomenon called a dynamic stall, which is a major component of the unsteady aerodynamics of a Darrieus wind turbine with a low tip speed ratio (TSR)

(Nobile et al., 2011; Paraschivoiu, 2002), an aerodynamic analysis of a VAWT is complex. The dynamic stall of a blade can produce a lift force and pitching moment values that exceed static values. The dynamic stall process depends on both the amplitude and the history of angles of attack of the airfoil (Spera, 2009). Due to the formation of vortices, which reduce the static pressure on the suction side of the rotor blade, the presence of a dynamic stall at low TSRs can have a positive impact on power generation; however, the formation of vortices can have negative consequences such as vibration, noise, and a reduction in the fatigue life of the components of the VAWT (Fujisawa and Shibuya, 2001) during operation. A VAWT with straight variable-pitch blades can change the amplitude and the rate of increase of the angle of attack in one revolution, compared to a VAWT with straight fixed-pitch blades. Simão Ferreira et al. (2007, 2009, and 2010) investigated the dynamic stall of a two-dimensional single-bladed VAWT via PIV and evaluated the differences between the commonly used turbulence models. Zhang et al. (2013) predicted the aerodynamic performance and the flow field of a straight-bladed VAWT. The power coefficient of the two-dimensional computational fluid dynamics (CFD) agreed well with the experimental data, and it was demonstrated that the RNG k-ε turbulent model is a useful resource to predict the tendency of aerodynamic forces; however, the model requires a high estimate value of the turbulence viscosity coefficient.

The present paper describes the results of our numerical and experimental studies on the performance of a VAWT with variable-pitch straight blades, which are symmetrical airfoils (NACA0018). A two-dimensional numerical simulation of the flow around a VAWT was performed using the commercial CFD software ANSYS FLUENT 13.0. The aim of this paper is to clarify the reason, in terms of aerodynamics, for improving the performance of a straight-bladed VAWT that will be installed with a variable-pitch mechanism. The effects of the variable-pitch angle, TSR, and the turbulent models, i.e., the RNG k-ε (Yakhot and Orszag, 1986), Realizable k-ε (Shih et al., 1995), and SST k-ω (Menter, 1994) turbulent models, on the performance of the VAWT were investigated. In addition, a numerical simulation of the unsteady flow around the blades was conducted to predict the occurrence of a dynamic stall for the VAWTs with fixed- and variable-pitch straight blades.

4.3 Methodology

4.3.1 Model geometry

A VAWT with variable-pitch straight blades utilizing a linkage mechanism was designed and built as shown in Fig. 4-1 (Kiwata et al., 2010). The main geometrical features of this turbine are shown in Table 2. The wind turbine had a diameter of D (=2R) = 800 mm and a height of h = 800 mm. The section of the VAWT that was analyzed was the symmetrical airfoil of its NACA0018 blade, which had a maximum lift coefficient $C_{L\max}$ at an angle of attack of $\alpha \approx 15°$ and a maximum lift-to-drag ratio C_L/C_D at an angle of attack of $\alpha \approx 5.5°$ (Sheldahl and Klimas, 1981). The rotor of the VAWT was composed of three blades with a chord length of c = 200 mm and a main shaft with a diameter of 0.06 m. The solidity was σ (= $nc/\pi D$) = 0.239, which is defined as the ratio of the total blade area (nc) to the circumference area (πD). Figure 4-2 shows a top view of the VAWT and its variable-pitch mechanism, which consists of a four-bar linkage with an adjustable eccentric link l_e. This turbine had an eccentric rotational point O_e that was different from the main rotational point O. Point P_1 is near the leading edge of the blade, and point P_2 is near the trailing edge of the blade. The angle between the main-link (l_m) and the x - axis is the azimuthal angle (θ). This mechanism is able to vary the pitch angle α_p according to the rotation of the main link without utilizing the actuators. The geometry of the pitch angle (α_p) is the sum of the blade offset angle (α_c) and the blade pitch angle amplitude (α_w). The optimum blade offset pitch angle was chosen from the experimental results to be α_c = 11.9° (Kiwata et al., 2010). The blade pitch angle amplitude was changed from α_w= ±0° to ±15.0° by increasing the length of the eccentric link from l_e = 0 m to 22 mm.

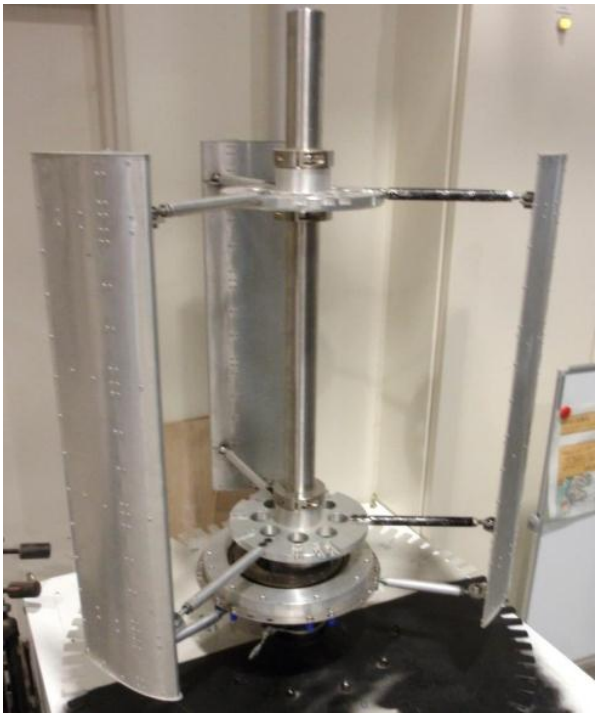

Figure 4-1 Vertical-axis wind turbine with variable-pitch straight blades

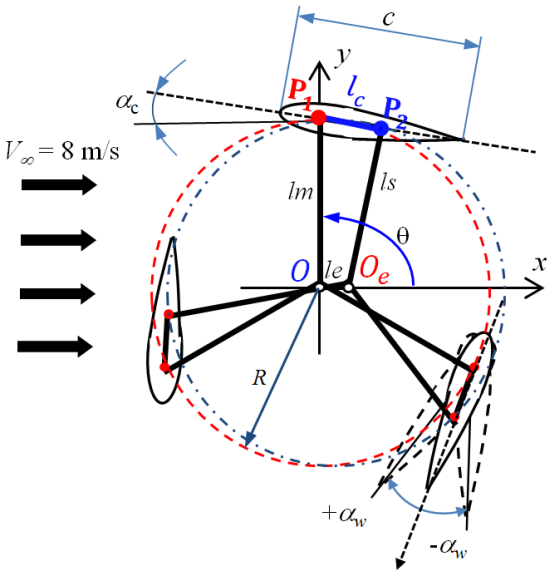

Figure 4-2 VAWT with variable-pitch blade mechanism utilizing a four-bar linkage

Table 2 Main Geometrical Features of the tested wind turbine

Turbine diameter, D	800 mm
Blade span length, h	800 mm
Blade chord length, c	200 mm
Blade airfoil	NACA0018
Number of blades, n	3
Aspect ratio, AR (= h/c)	4
Turbine solidity (= $nc/\pi D$)	0.239
Main link length, l_m	373 mm
Second link length, l_s	365 mm
Blade link length, l_c	85 mm
Eccentric link length, l_e	0 mm, 15 mm, 22 mm

4.3.2 Experimental apparatus

Figure 4-3.shows a schematic diagram of the experimental apparatus. The experiments were carried out in a circuit wind tunnel with an open test-section that had a cross-sectional area of 1250 mm × 1250 mm. The open test-section has the capability to allow the conditions inside the test section to be largely unaffected by larger blockage percentage models because of the ability to leak flow and expand the flow around objects within the test-section (Ross and Altman, 2011).The uniform flow in the analyzed area was measured by an ultrasonic anemometer (Kaijo Sonic, DA-650-3TH (TR-90AH)). The turbulence and non-uniform level variation in the exit of nozzle at a wind speed V_∞ = 8 m/s was less than 0.5% and ±1.0%, respectively. A geared motor (Mitsubishi Electric, GM-S) and a frequency inverter with aerodynamic breaking resistor (Hitachi Industrial Equipment Systems, SJ200) were used to drive the wind turbine. The torque T and rotation speed N of the wind turbine were measured in each case in order to calculate the power coefficient C_P (=$T\omega/0.5\rho DhV_\infty^3$; ρ, air density; ω, turbine angular velocity) by using a torque transducer (TEAC TQ-AR5N with a rate capacity of 5 N·m) and a digital tachometer (ONO SOKKI HT-5500) under a constant wind velocity of V_∞ = 8 m/s. The wind velocity setting of (V_∞ = 8 m/s) is the best performance of wind turbine with NACA0018 airfoil blade at pith angle off set α_c = 11.9°. The power

performance increase as increase wind speed until V_∞ = 10 m/s and not significant increase when wind speed more than V_∞ = 10 m/s.

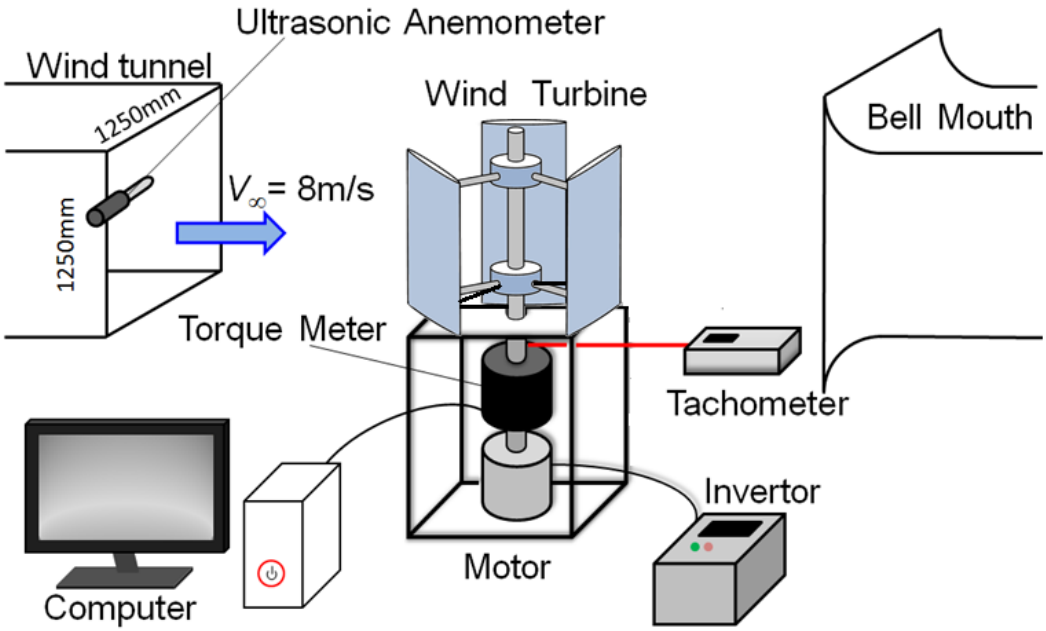

Figure 4-3 Open circuit wind tunnel of the experimental apparatus

4.3.3 Mechanical loss

The performance of wind turbine installed is total performance include losses such as mechanical losses, electrical losses. Mechanical loss consist gear box losses and losses from bearing. In experimental result, the calculating of performance is sum of total power include of mechanical losses except electrical losses and gear box losses. Figure 4-4 shows mechanical loss of total torque production of wind turbine

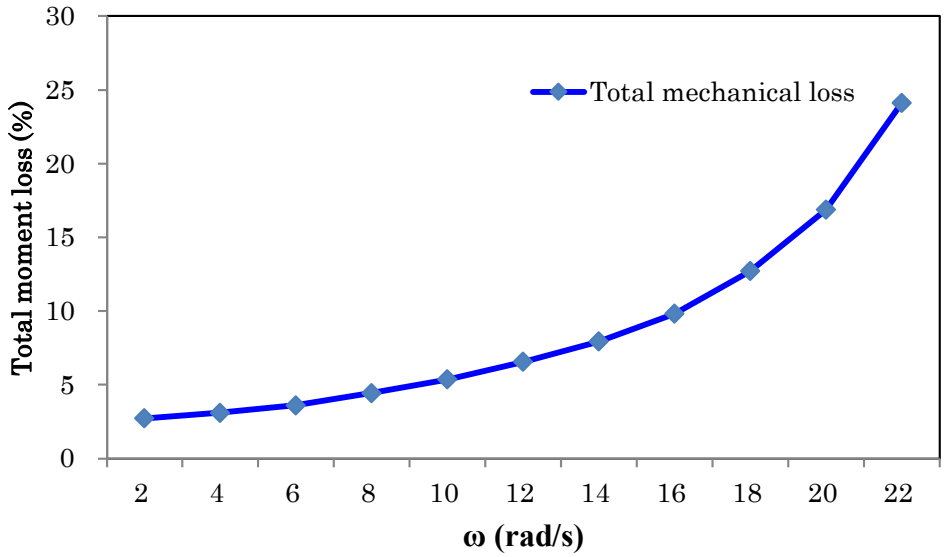

Figure 4-4 Mechanical losses of wind turbine torque

4.4 Numerical Simulation

4.4.1 Computational domain and meshing

The two-dimensional computational domain, boundary conditions, and the mesh structure are shown in Figs. 4-5 and 4-6. The computational domain had a radius of 12*R*, and the inlet and outlet boundary conditions were placed upwind and downwind of the rotor, respectively, as shown in Fig. 4-5. The inlet of the computational domain corresponded to the uniform flow condition at V_∞ = 8 m/s with a turbulence intensity of 1.0% and turbulence viscosity ratio of 5.0 %. The pressure outlet condition for $\Delta p = 0$ was specified at the downstream boundaries of the computational domain. The computational domain consisted of three mesh zones, i.e., one fixed sub-domain outside the rotor, one dynamic sub-domain around the rotor with a radius of 3*R*, and three dynamic sub-domains around the blades with a diameter of 3*c* and an equal spacing of 120°, as shown in Fig. 4-6. The mesh interfaces consist of one mesh interface around the rotor and three around blades 1, 2, and 3. A dynamic mesh technique was used for this simulation. The dynamic meshes around the rotor and blades rotate according to the TSR, while the mesh on the exterior of the rotor remains stationary. The rotation of the four dynamic sub-domains can be controlled independently by a user-defined function (UDF), which was programmed in *C++* code. The surfaces of the blades and main shaft were set as a wall, i.e., no-slip boundary conditions. The fixed sub-domain was meshed using quadrilateral grids, and the dynamic sub-domain around the rotor was meshed

using triangular grids. The three dynamic sub-domains around the blades were meshed using a combination of triangular grids and quadrilateral grids, especially near the surfaces of the blades. In order to construct a high density mesh on the surfaces of the blades, the layers of the cells were generated by using an inflation tool that had a growth rate of 1.2. The distance of the first layer was 0.01 mm, and $y^+ < 1$ was obtained. The fixed sub-domain on exterior side of the rotor had 116,808 elements, the sub-domain around the rotor had 21,680 elements, and the three dynamic sub-domains around the blades had 66,389 elements. The total number of elements was about 3.37×10^5.

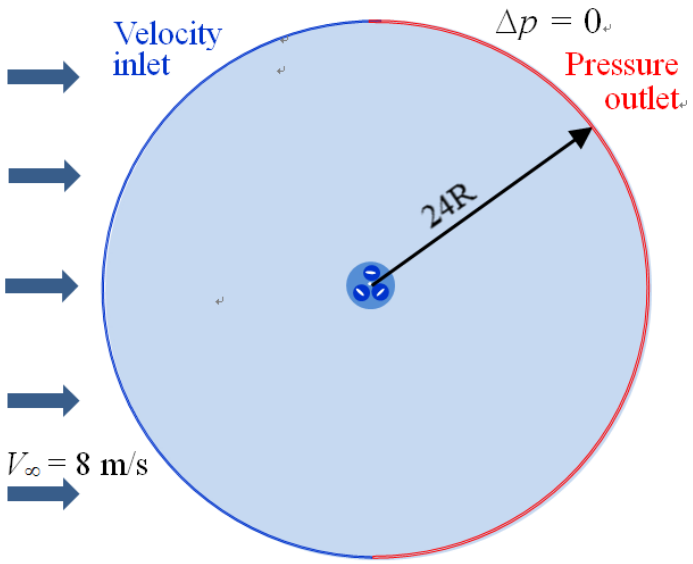

Figure 4-5 Computational domain and boundary condition

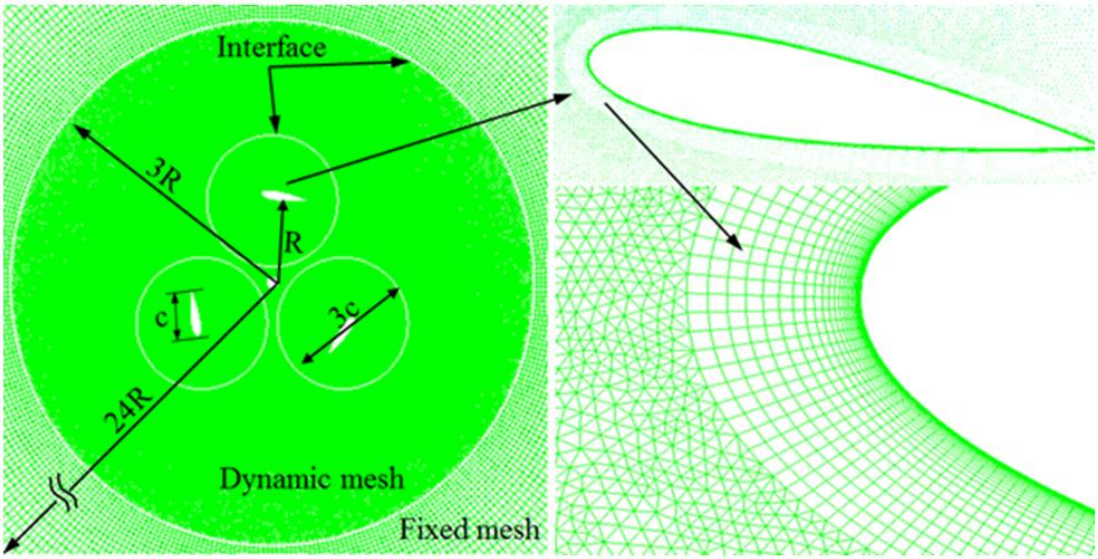

Figure 4-6 Mesh structure in the computational domain

4.4.2 Turbulence model and solver setting

A two-dimensional numerical simulation of the VAWT was performed using FLUENT 13.0 software with the flow conditions corresponding to the experiment. The governing equations were the continuity equation and the unsteady Reynolds-averaged Navier-Stokes (URANS) equation, in which the Reynolds stresses were solved by using the three different turbulence models (the RNG k-ε, Realizable k-ε, and SST k-ω models). The computational domain was discretized using the finite volume method. The convection terms of the governing equation were discretized using the second-order upwind discretization method. The implicit algorithm of the PISO method was applied for the pressure-velocity coupling. Table 3 shows a summary of the parameters employed in the six different cases where different time steps and TSRs were defined. The TSR ($\lambda = R\omega/V_\infty$) was varied from λ = 0.5 to 2.0. For all of the transient simulations, the total time was defined to allow enough time for the formation of flow to develop around the rotor. Consequently, the fluctuating torque coefficient became periodically stable when the turbine minimum operated more than of three revolutions.

4.4.3 Numerical conditions

Three different rotor blade configurations were evaluated. Case 1 had a fixed-pitch blade with a pitch angle of $\alpha_w = 0^\circ$. Case 2 had a blade pitch angle of $\alpha_w = \pm 10.2°$; this blade pitch angle changed from $\alpha_p = 1.8°$ to $\alpha_p = 22.1°$ in one revolution. Case 3 had a

variable-pitch blade with an angle of $\alpha_w = \pm 15.0°$; this blade pitch angle changed from $\alpha_p = -3.1°$ to $\alpha_p = 26.9°$ in one revolution. The blade offset pitch angle was chosen to be $\alpha_c = 11.9°$ from the experimental data. The variation of pitch angle, α_p will be show in next section.

Table 3 Input data for the six cases

Tip speed ratio, λ	Turbine rotational speed, N (min^{-1})	Number of time steps for one cycle	Time step size (s)	Time for one cycle (s)	Time steps for total unsteady calculation (Minimum)
0.5	95.5	720	8.73×10^{-4}	0.628	2160
1.0	191.0		4.36×10^{-4}	0.314	
1.2	229.2		3.67×10^{-4}	0.262	
1.5	286.5		2.91×10^{-4}	0.209	
1.7	324.7		2.57×10^{-4}	0.185	
2.0	382.0		2.18×10^{-4}	0.157	

4.4.4 Convergence and Accuracy

The convergence of steady simulation must be achieved as shown in figure 4-7. A number of iterations is needed to obtain the convergence.

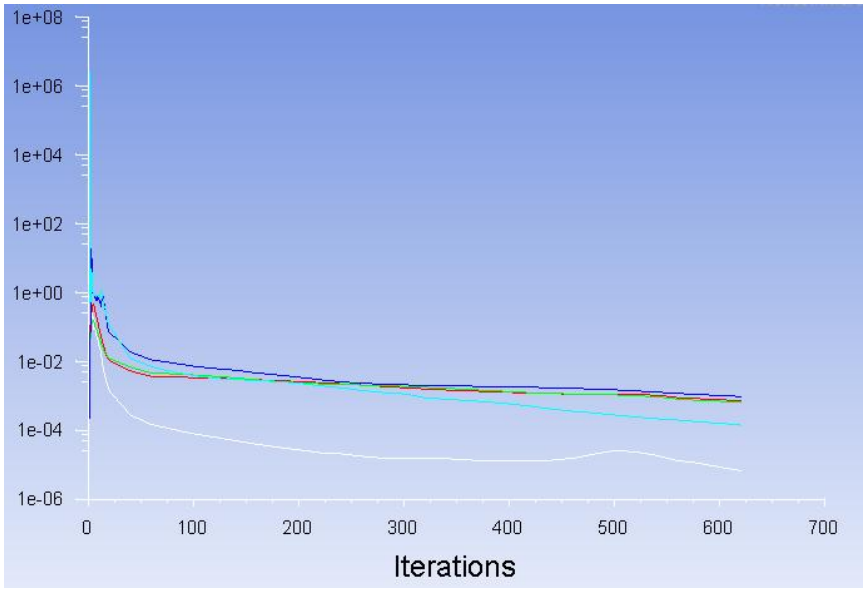

Figure 4-7 Scaled residuals of steady simulation

For unsteady simulation, a number of time steps should be enough to achieve stability of value of performance such as; moment, lift, drag, etc., of blade rotor.

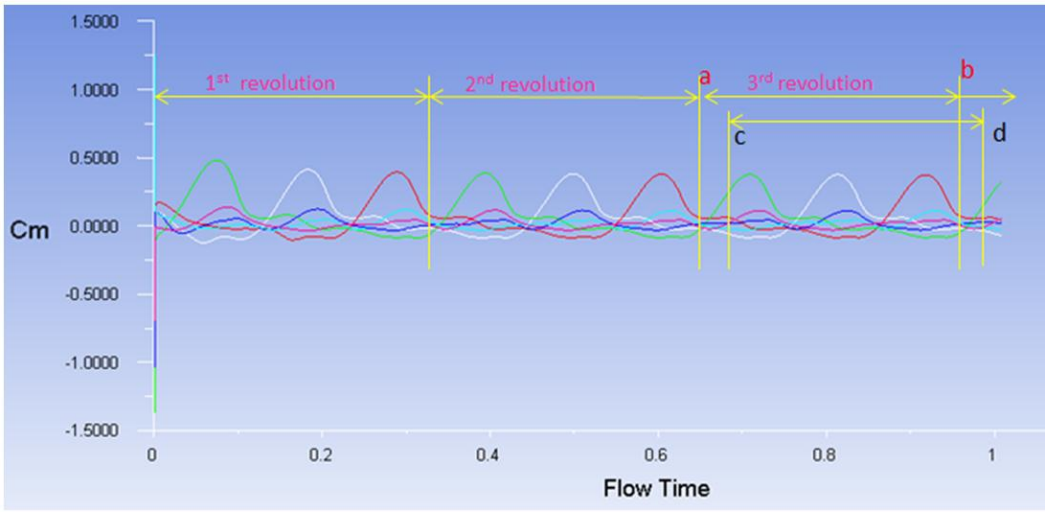

Figure 4-8 Moment of each blade of rotor of unsteady simulation

4.5 Characteristics of variable-pitch blades

4.5.1 Variations of the angle of attack and pitch angle of a blade

Figure 4-9 shows the local velocity vectors and the transient aerodynamics forces exerting on the rotating blade. The local relative velocity vector of blade $\boldsymbol{W}$ is dependent on both the local wind velocity vector $\boldsymbol{V_i}$ ($|\boldsymbol{V_i}| = V_i$) and the tangential velocity vector $\boldsymbol{V_t}$ ($|\boldsymbol{V_t}| = R\omega$), as shown in the following equations.

Equation 4-1

$$\boldsymbol{W} = \boldsymbol{V_i} + \boldsymbol{V_t}$$

The length of the local velocity vector (relative inflow velocity) $|\boldsymbol{W}(\theta)|$ at an arbitrary azimuthal angle θ is defined as

Equation 4-2

$$|\boldsymbol{W}(\theta)| = [V_\infty^2 \, (a^2 + \lambda^2 + 2a\cos(\theta - 90)]^{0.5}$$

where a ($=V_i/V_\infty$) is the ratio of the induced velocity to the free-stream velocity, and λ ($=R\omega/V_\infty$) is the TSR.

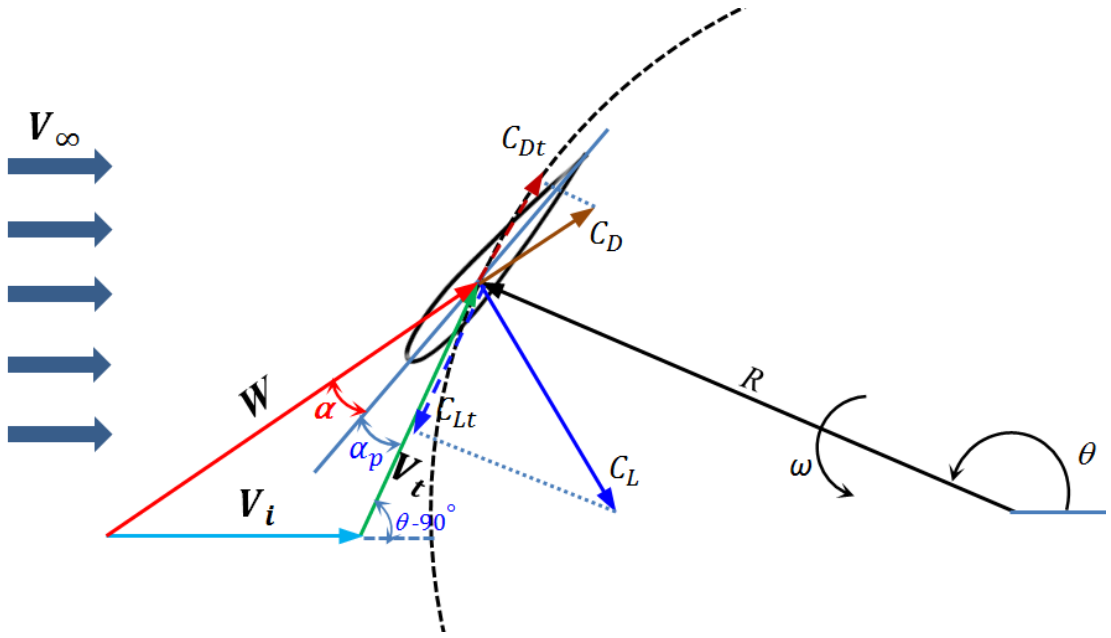

Figure 4-9 Schematic diagram of the angles and vectors of the velocity, drag, and lift coefficient of a rotating blade

The variation of the relative velocity of the blade with the azimuth angle (θ) is shown in Fig. 4-10 with the assumption that a = 1. The relative velocity has a maximum value at θ = 90° and a minimum value at θ = 270°.

The torque coefficient of each blade was calculated by the moment of the blade, which is the difference between the tangential component of lift and the drag of the blade against the center point of the rotor. The tangential component of lift and drag are perpendicular to the radius of the rotor. The expression of the torque coefficient is given by

Equation 4-3

$$C_t = C_L \sin(\alpha + \alpha_p) - C_D \cos(\alpha + \alpha_p)$$

The blade pitch angle α_p depends on the blade offset pitch angle α_c and the blade pitch angle amplitude α_w. The geometrical angle of attack of the blade α is defined as a function of the TSR λ and the azimuthal angle θ, as given by

Equation 4-4

$$\alpha = \tan^{-1}[\cos\theta / (\sin\theta + \lambda/a)] + \alpha_p$$

In the upstream area ($90° \leq \theta \leq 270°$), the value of a is greater than in the downstream area ($-90° \leq \theta \leq 90°$).

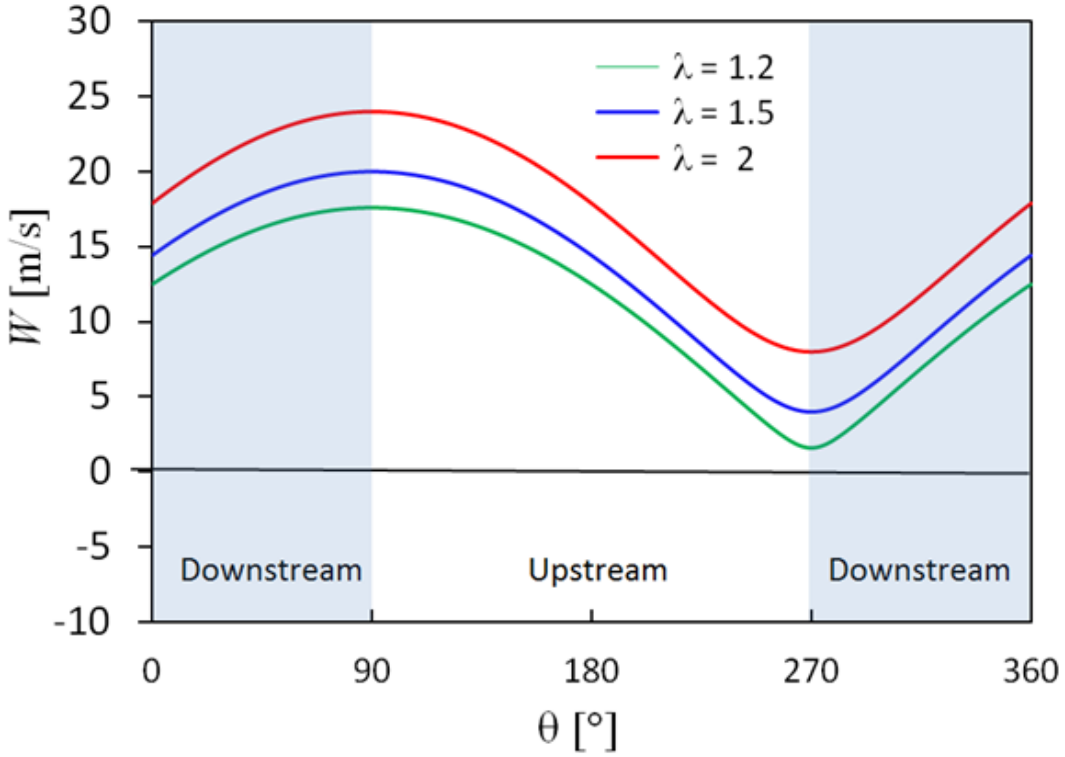

Figure 4-10 Variation in the relative inflow velocity for a = 1 and V_∞=8m/s

Figure 4-11 shows the variations in the blade pitch angle α_p and the geometrical angle of attack α in a uniform flow at a constant TSR of λ = 1.5, on the assumption that a = 1. The blue and green dashed lines show the variations in the blade pitch angle amplitudes α_w = ±10.2° and ±15.0° with the blade offset pitch angle of α_c = 11.9°, respectively. The red solid line shows the variations in the geometrical angle of attack α of α_w = ±0°. The amplitude of the geometrical angle of attack of the fixed-pitch blade is larger than that of the variable-pitch blade. If the variable-pitch mechanism is installed in a straight-bladed VAWT, the amplitude of the geometrical angle of attack of the variable-pitch blade will become small. The variable-pitch mechanism has potential to reduce the peak angles of attack of the blades, alleviating the time it spends in stalls. Figure 4-12 shows the geometrical angle of attack of three different TSRs for α_w = ±10.2°. The amplitude of the geometrical angle of attack of the variable-pitch blade

decreases as the TSR increases. The geometrical angle of attack of λ =1.2 varies from $\alpha = -37.3°$ to $+65.5°$.

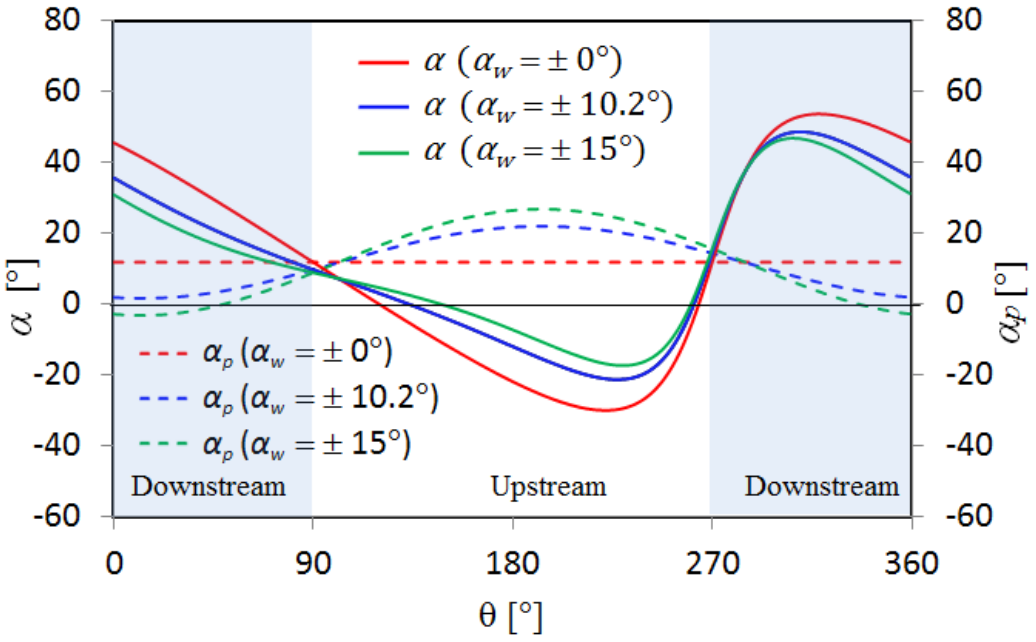

Figure 4-11 Variation in the blade pitch angle and geometrical angle of attack of a blade at λ = 1.5 for α_c = 11.9° and a =1

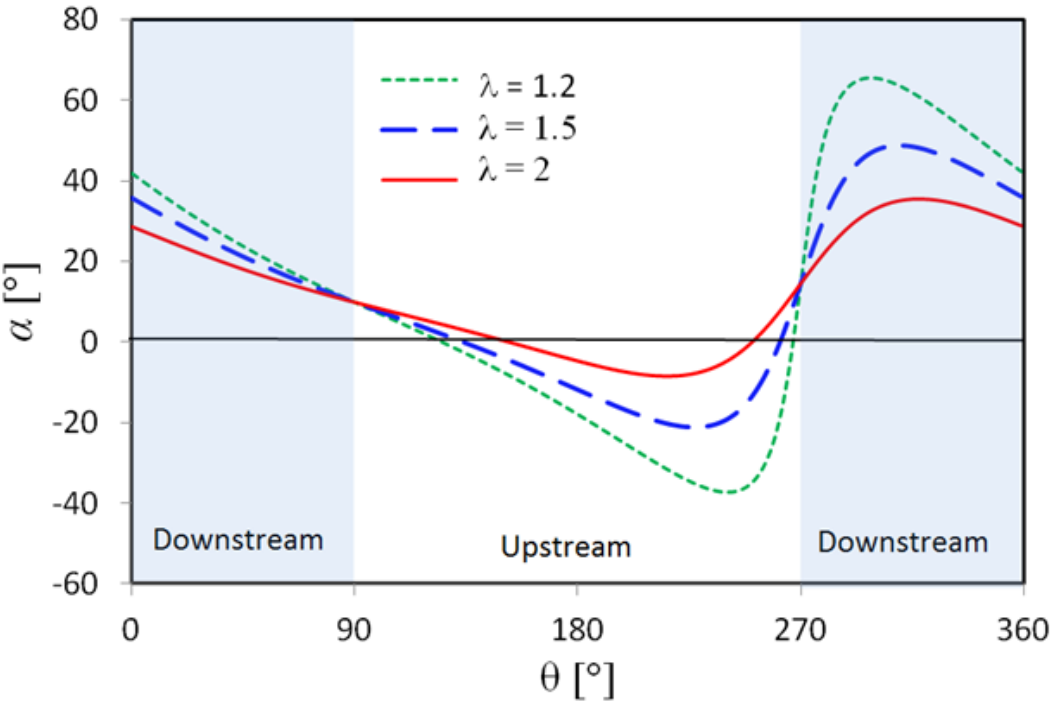

Figure 4-12 Variation in the blade pitch angle and geometrical angle of attack of a blade for α_w = ±10.2° and a =1

4.6 Results and Discussion

4.6.1 Evaluation of the turbulence model in numerical simulations

Three types of turbulence models, i.e., the RNG k-ε, Realizable k-ε and SST k-ω, were examined for the two-dimensional numerical simulation of flow and performance of a VAWT with variable-pitch blades. Figures 4-13 and 4-16 show the contours of the velocity and pressure coefficient obtained by using the three models for the VAWT with variable-pitch blades for α_w = ±10.2° at λ = 1.5. Although a slight difference is evident in the wake of the main shaft between the SST k-ω model, and the RNG k-ε and Realizable k-ε models, no significant difference is apparent in the flow pattern around the rotor among the models.

Figure 4-21 shows the prediction of the torque coefficient C_{TBK} (θ) for one of the variable-pitch blades with α_w = ±10.2° at λ = 1.5 for one revolution. One of the important advantages of using a numerical simulation is the ability to predict the generation of torque on one blade rotor despite the simultaneous operation of multiple rotors, which is difficult to obtain when using experimental results. The torque coefficient predicted by using the SST k-ω model is higher at any azimuthal angle than those

of the RNG and Realizable k-ε models. The maximum torque was generated at $\theta = 200°$ for the variable-pitch blade with $\alpha_w = \pm 10.2°$ at $\lambda = 1.5$. A positive torque was generated except when $90° < \theta < 135°$ and $270° < \theta < 360°$. The torque has a high positive value in the upper range of $135° < \theta < 270°$, which is referred to as the high-torque zone (HTZ). The range and peak value of the positive torque coefficient in the HTZ depends on the relative velocity and amplitude of the angle of attack of the blade. Negative and low torques were generated in the downstream areas and when $90° \leq \theta \leq 135°$ even though the largest relative velocity of the rotating blade occurred at an azimuth angle of $\theta = 90°$ due to both of low angle of attack and domination of drag. Therefore, to increase the performance of a straight-bladed VAWT, the angle of attack of the blades is one of the most important factors. The angle of attack can be controlled by varying the blade pitch angle α_p with the azimuthal angle θ.

Figure 4-24 shows the power coefficients C_p of the VAWT with variable-pitch blades with $\alpha_w = \pm 10.2°$. The power coefficients of the SST k-ω and the Realizable k-ε models were predicted to be higher than those of the RNG k-ε model. The power coefficient of the RNG k-ε model is comparatively close to the experimental value. Qin et al. (2011) reported that the predicted torque of the VAWT with fixed-pitch straight blades obtained by using the Realizable k-ε model was much higher than that when using the RNG k-ε model. The Realizable k-ε model has a limitation to produce non-physical turbulent viscosities when the computational domain contains both rotating and stationary fluid zones (ANSYS Theory Guide, 2012). However, they found that the RNG model predicted the flow fields to be relatively more compact than the standard k-ε model, but with strong vortices downstream of the trailing edge of the blade. Howell et al. (2010) also showed that the RNG k-ε model is able to predict flow fields that include large flow separations more accurately than the standard k-ε model. The aerodynamic performance prediction of a straight-bladed VAWT was investigated by Zhang et al. (2013). It was demonstrated that the RNG k-ε model is able to predict the tendency of aerodynamic forces, but with a high estimate value of the turbulence viscosity coefficient. Almohammadi et al. (2013) showed that the predicted maximum power coefficient obtained using the SST k-ε model was higher than that obtained using the RNG k-ε model. Thus, although turbulence models have an influence on the resultant flow field and performance of the VAWT, the effect of blade pitch angle amplitude

on the performance of a VAWT with variable-pitch blades was investigated in the present study using the RNG k-ε model.

4.6.2 Power coefficients of the VAWTs with variable- and fixed-pitch blades

The power coefficients C_P of the VAWTs with variable- and fixed-pitch blades for the numerical simulation and experiment are shown in Figs. 4-24 and 4-25, respectively. These figures present the effects of the blade pitch angle amplitude α_w on the power coefficient of the wind turbine. The effects of the blade pitch angle amplitude qualitatively agree with the two-dimensional numerical simulation using the RNG k-ε

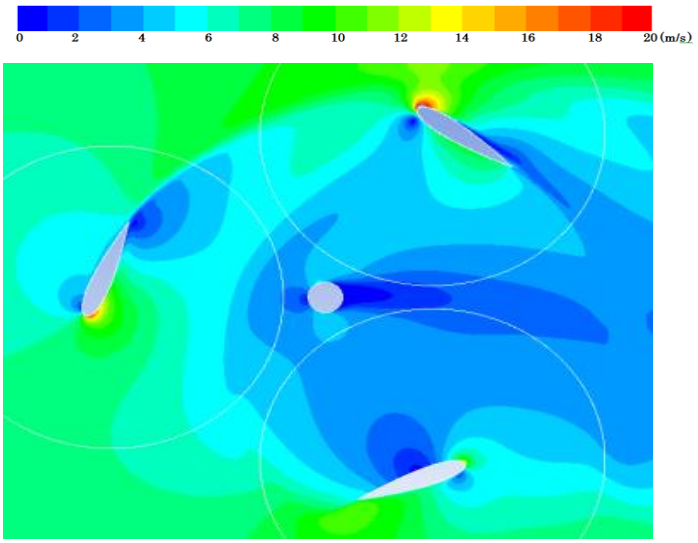

Figure 4-13 Velocity contours (RNG k-ε model)

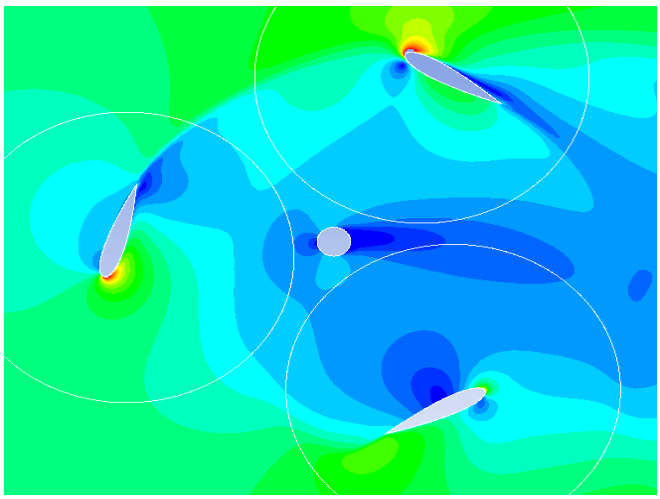

Figure 4-14 Velocity contours (Realizable k-ε model)

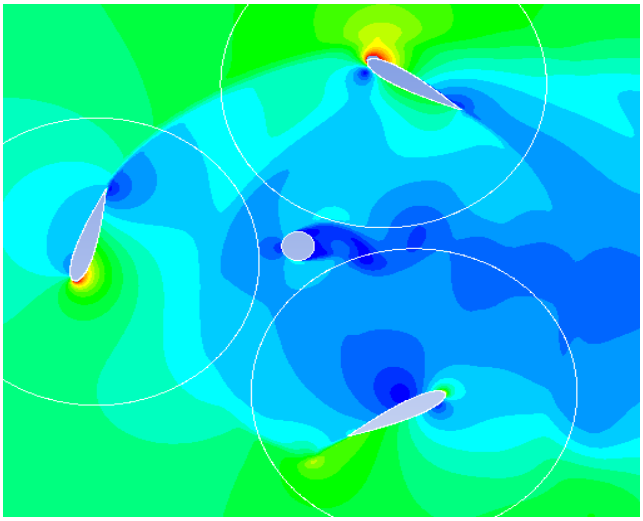

Figure 4-15 Velocity contours (SST *k*- ω model)

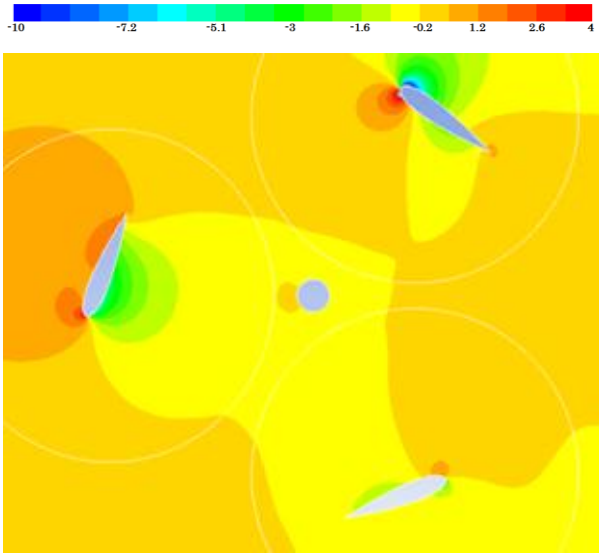

Figure 4-16 Pressure coefficient contours (RNG *k*-ε model)

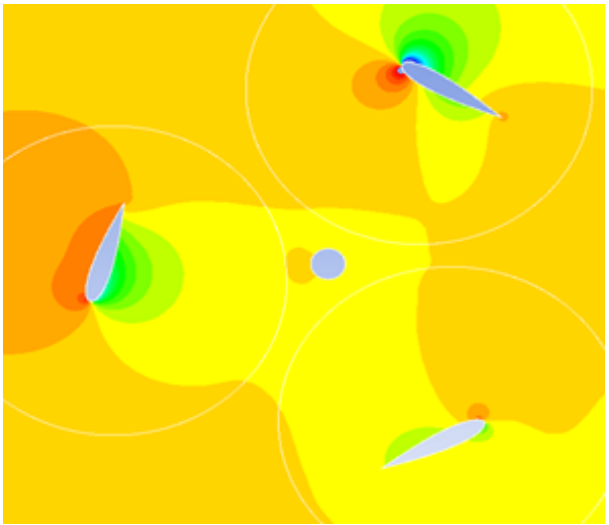

Figure 4-17 Pressure coefficient contours (Realizable *k*-ε model)

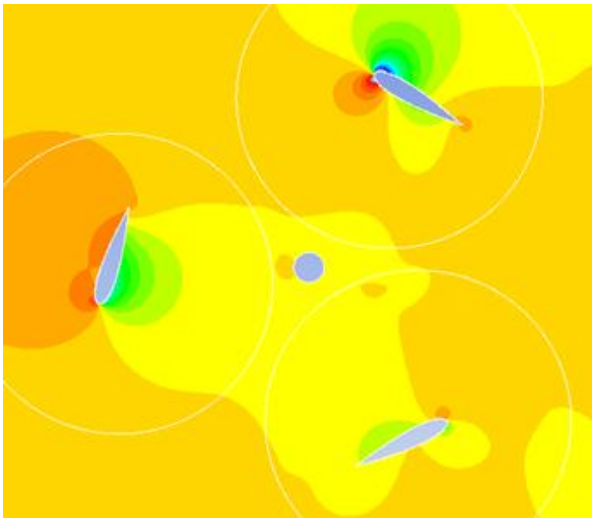

Figure 4-18 Pressure coefficient contours (SST *k*- ω model)

turbulence model and the experiment. The power coefficient of the VAWT with variable-pitch blades with α_w = ±10.2° is higher than that with fixed-pitch blades. The peak power coefficients of the variable-pitch blades with α_w = ±10.2° and the fixed-pitch blades occur at a higher TSR when compared to those with variable-pitch blades with α_w = ±15.0°. With a low TSR of λ < 1.0, the power coefficient C_P for a wind turbine with a large amplitude of α_w = ±15.0° becomes slightly larger or the same as one with α_w = ±10.2°. With a high TSR of λ > 1.2 in the numerical simulation or λ > 1.8 in the experiment, the power coefficient C_P for a wind turbine with fixed-pitch blades (α_w = ±0°) become larger than one with variable-pitch blades with α_w = ±10.2°. The power coefficient of the variable-pitch blade with α_w = ±15.0° rapidly decreases at a high TSR compared to those of the other cases. The differences between the power coefficients at a low and a high TSR are due to the angle of attack, which is affected by the pitch angle amplitude and TSR of the rotor, as shown in Figs.4-10 and 4-11. A VAWT with limited-span blades was also investigated by Howell et al. (2010), and their results showed that the presence of vortices along the tips of the blades in their 3D simulation was responsible for producing an efficiency that was significantly different compared to the 2D simulation. The difference in the power coefficient between the 2D numerical simulation and the experiment in the present study is considered to be an effect of the blade tips, i.e., the small aspect ratio of the blade [AR (= h/c) = 4] and the additional loss from the support arms.

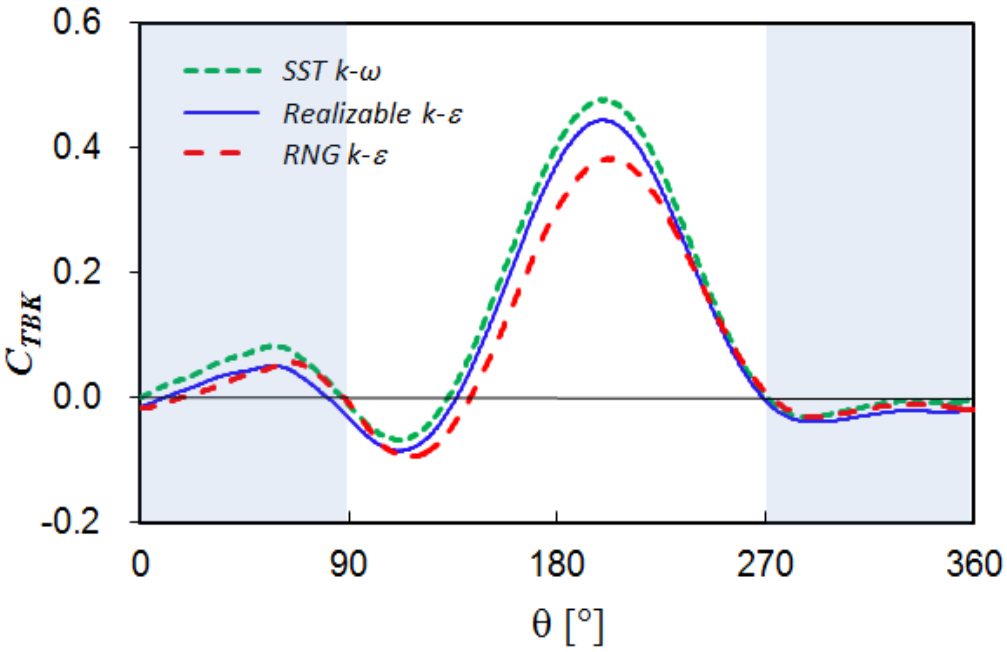

Figure 4-19 Torque coefficients (C_{TBK}) of one blade with α_w = ±10.2° at λ = 1.5

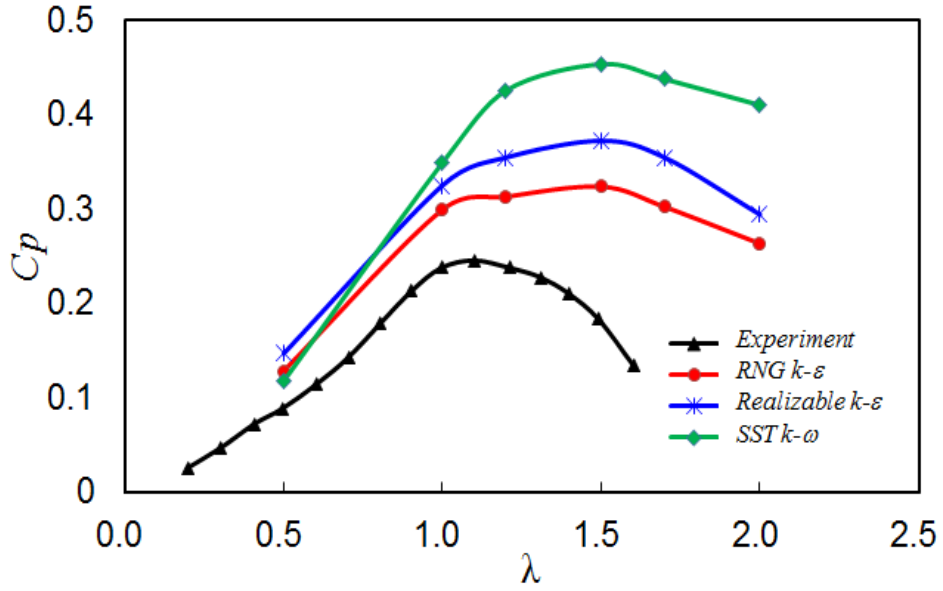

Figure 4-20 Power coefficients of the simulations that used the *RNG k-ε*, *SST k-ω*, and Realizable *k*-ε turbulence models, and the wind tunnel test for α_w = ±10.2

4.6.3 Effect of variable pitch angle on torque coefficients

The torque of a straight-bladed VAWT is generated by the moment of the rotating blades, which results from the tangential component of lift and drag forces on the air-foil. The generation of fluid forces on the blades depends on the relative inflow velocity and the angle of attack, i.e., the azimuthal angle position. The variation of the torque

coefficients C_{TBK} (θ) for one of the blades at λ = 1.5 with an azimuthal angle θ is shown in Fig. 4-26. The maximum torque for the variable-pitch blade with α_w = ±10.2° was generated at λ = 1.5. The generated torque on a blade of a straight-bladed VAWT varies for one cycle. The variation of the torque coefficient is classified into two zones for one cycle: an upstream zone at 90 ≤ θ ≤ 270° and a downstream zone at 270° ≤ θ ≤ 360° and 0° ≤ θ ≤ 90°. For the fixed-pitch blades (α_w = ±0°), a negative torque was generated at azimuthal angles of 0° ≤ θ ≤ 105° and 240° ≤ θ ≤ 360°. The maximum positive torque value occurred at θ ≈ 190°. On the other hand, for the variable-pitch blades (α_w = ±10.2° and ±15.0°), the azimuthal angle of the maximum torque increased slightly at θ ≈ 200° as compared to that of the fixed blades. The difference in the azimuthal angle of the maximum torque between the fixed- and variable-pitch blades is related to the azimuth angle at the optimum angle of attack, which approaches an angle of attack of the maximum lift coefficient of about α = 15° for the NACA0018 airfoil ($Re \approx 1.5\times10^5$). The maximum and minimum

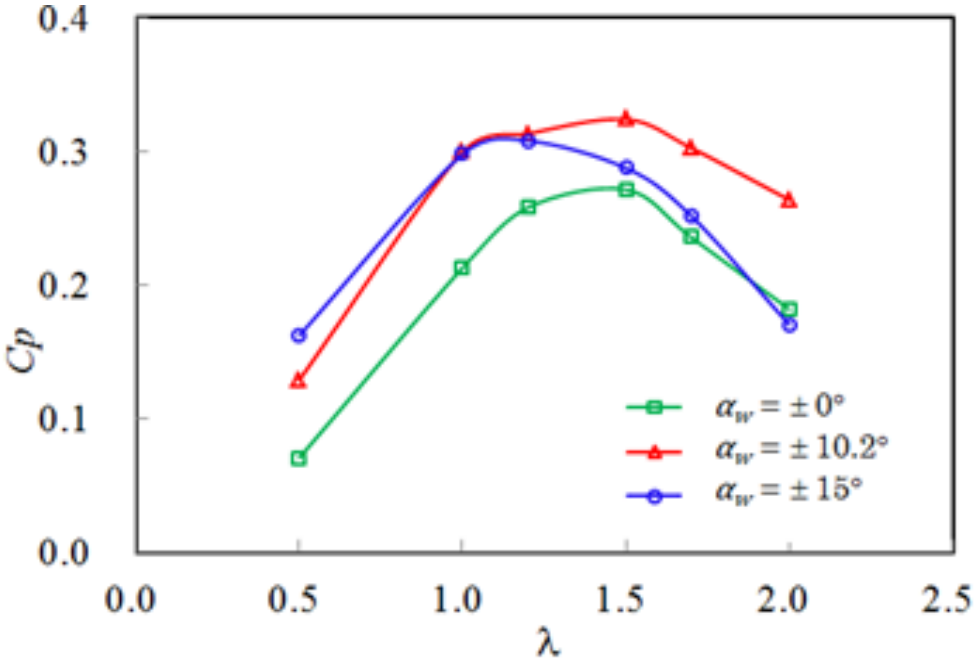

Figure 4-21 Effects of the blade pitch angle amplitude on the power coefficients (C_p) for the numerical simulation using the RNG k-ε model

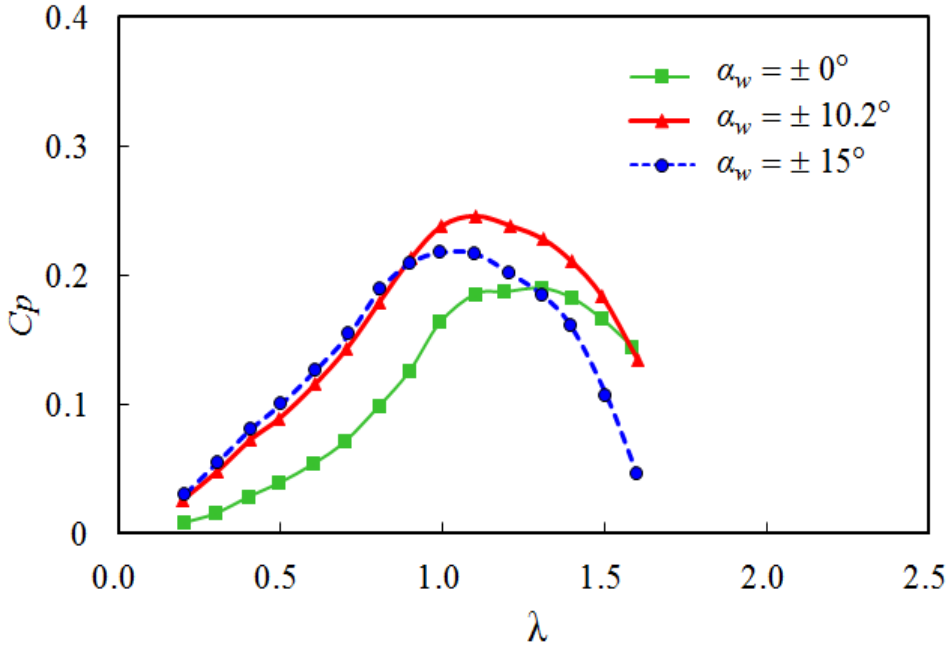

Figure 4-22 Effects of the blade pitch angle amplitude on the power coefficients (C_p) for the wind tunnel test

torques of the variable-pitch blades with α_w = ±15.0° are smaller than those with α_w = ±10.2°. However, there is only a slight difference in the torque coefficients between α_w = ±10.2° and ±15° at 55° ≤ θ ≤ 140°. Negative torque occurred for 90° ≤ θ ≤ 135° for all cases. However, for the fixed-pitch blade, the negative torque decreased due to the contribution of the lift force, as seen in Fig. 4-31.

Figure 4-30 shows the velocity contours around the rotor at λ = 1.5. For the fixed-pitch blade with α_w = 0°, the low velocity area (blue color) was more widely distributed than that of the variable-pitch blades. Figures 4-31 shows the pressure coefficient contours around the rotor at λ = 1.5. The difference in the pressure coefficient between the suction and pressure sides on the fixed-pitch blade at θ = 100° was smaller than that for the variable-pitch blade. Consequently, the negative torque of the fixed-pitch blade for 100° ≤ θ ≤ 140° decreased more than that of the variable-pitch blades with α_w = ± 10.2° and ± 15°, as shown in Fig. 4-29.

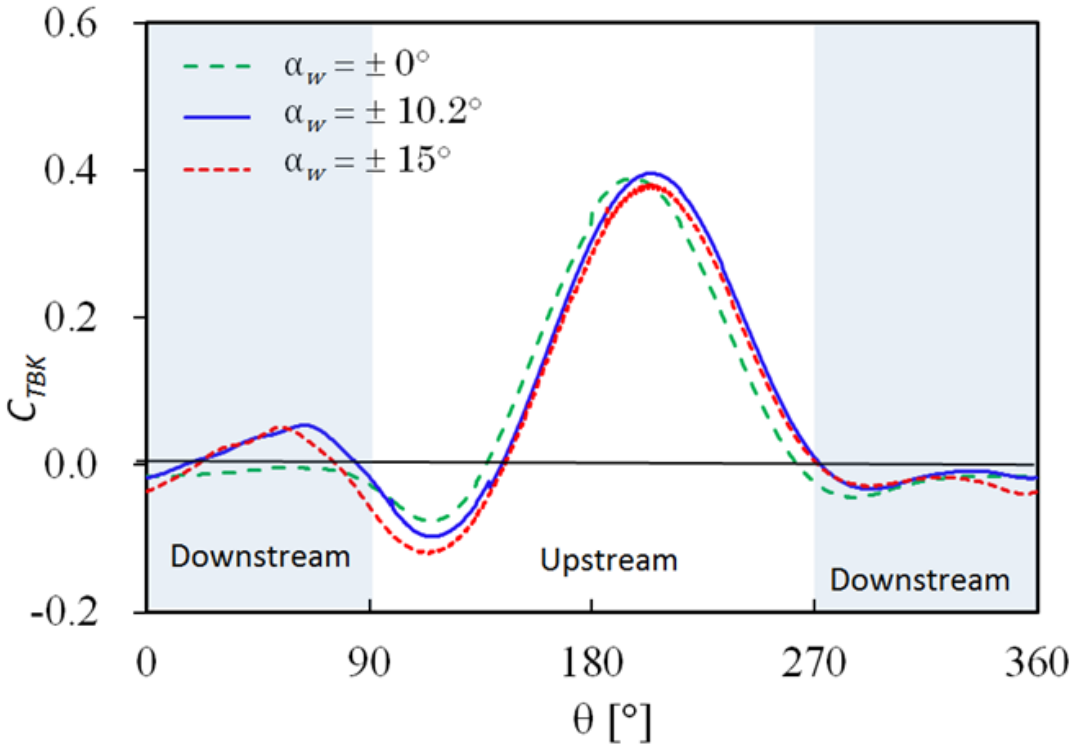

Figure 4-23 Effects of blade pitch angle amplitude on torque coefficients C_{TBK} (θ) for one of the blades at λ = 1.5 (RNG k-ε model)

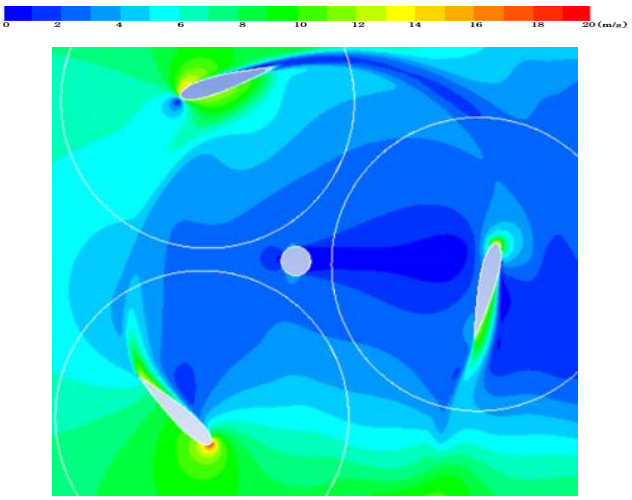

Figure 4-24 Effects of blade pitch angle amplitude on torque coefficients C_{TBK} (θ) for one of the blades at λ = 1.5 (RNG k-ε model) $\alpha_w = \pm 0°$

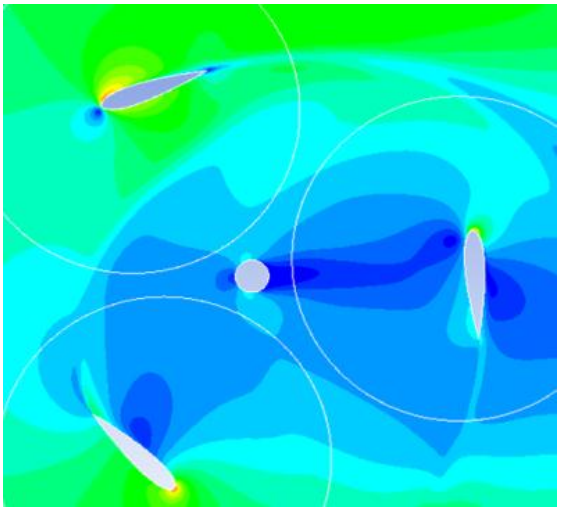

Figure 4-25 Effects of blade pitch angle amplitude on torque coefficients C_{TBK} (θ) for one of the blades at λ = 1.5 (RNG k-ε model) $\alpha_w = \pm$ 10.2°

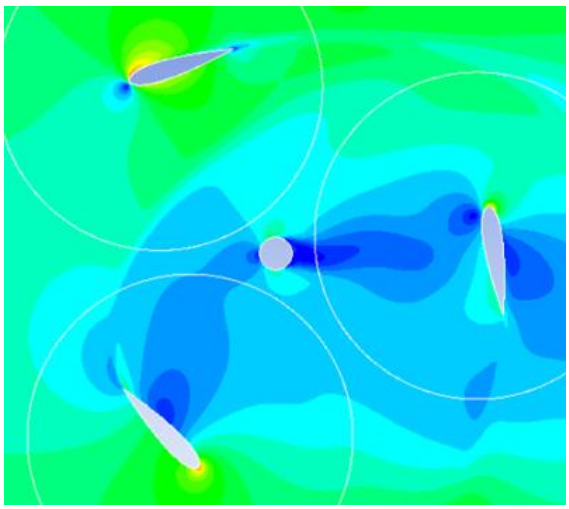

Figure 4-26 Effects of blade pitch angle amplitude on torque coefficients C_{TBK} (θ) for one of the blades at λ = 1.5 (RNG k-ε model) $\alpha_w = \pm$ 15°

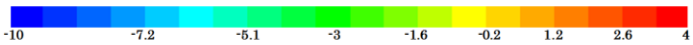

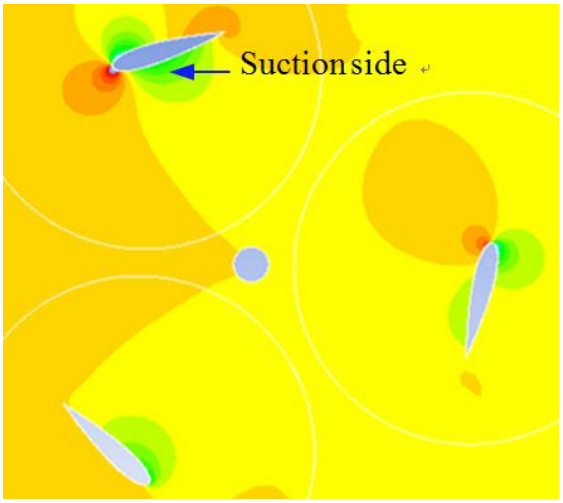

Figure 4-27 Pressure coefficient contours around the rotor at λ = 1.5 (RNG k-ε model) $\alpha_w = \pm 0°$

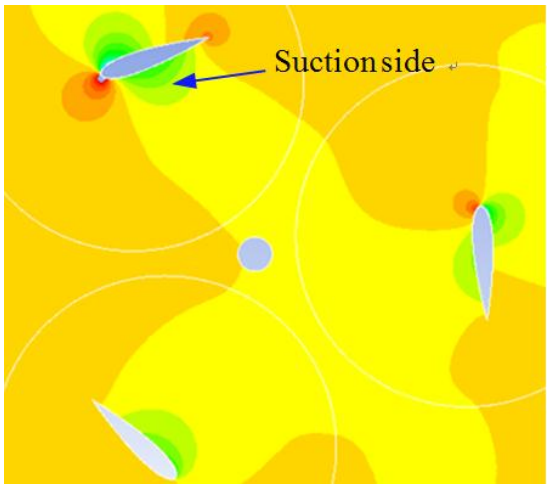

Figure 4-28 Pressure coefficient contours around the rotor at λ = 1.5 (RNG k-ε model) $\alpha_w = \pm 10.2°$

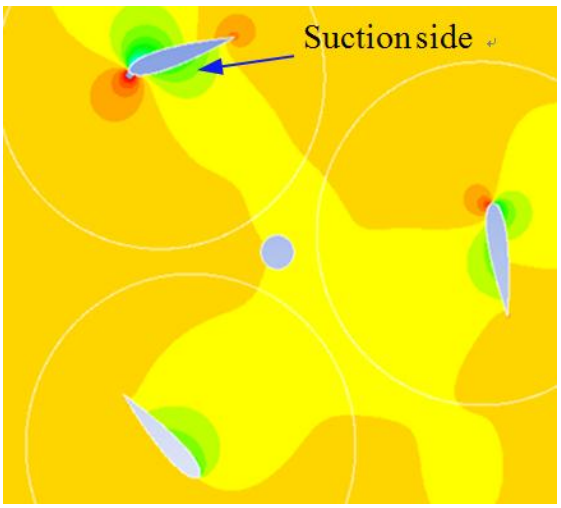

Figure 4-29 Pressure coefficient contours around the rotor at λ = 1.5 (RNG k-ε model) $\alpha_w = \pm 15°$

4.6.4 Effect of TSR on torque coefficients

The power and torque coefficients of the VAWT with variable-pitch blades with α_w = ±10.2° are shown in Fig.4-33. The total power and torque coefficients are divided into two components in the upstream and downstream areas. The power coefficient in the upstream area (curve C_{pu}) increases as the TSR increase. However, the total power coefficient (curve C_{pt}) was increase until a TSR of λ = 1.5, then decreases as the power coefficient in the downstream area decreases (curve C_{pd}). The torque coefficient for $\lambda \leq 1.5$ is positive in both the upstream and downstream areas (curves C_{tu} and C_{td}). However, for $\lambda > 1.5$, the torque coefficient in the downstream area becomes negative, and the torque coefficient decreases with an increase in the TSR. The total torque coefficient (curve C_{tt}) increases until a TSR of λ = 1.0, then decreases due to the decrement of the torque coefficient in both the upstream and downstream areas.

Figure 4-34 shows the effects of the TSR on the torque coefficient C_{TBK} (θ) for one cycle of the variable-pitch blades with α_w = ±10.2°. The torque coefficient fluctuations of one blade at four different TSRs are also presented. For a TSR of λ = 0.5, the maximum torque coefficient was generated at $\theta \approx 180°$, and the torque coefficient is nearly positive at all azimuth angles (except $90° < \theta < 125°$). The maximum value and peak angle of the torque coefficient varies with the TSR (shown as the inside of circle *b* in Fig. 4-34). For a low TSR of λ = 0.5, the maximum value of the torque coefficient was higher than that for a high TSR and shifted to a large azimuth angle as the TSR increased. The azimuth angle for the maximum torque coefficient increases as the TSR increases. The shift of the azimuthal angle for the maximum torque coefficient is related to the angle of attack of the rotating blade, i.e., the azimuthal angle where the angle of attack becomes the maximum lift coefficient ($\alpha \approx 15°$) or the minimum angle of attack (see Figs. 4-10 and 4-11).

Figures 4-32, 4-33, 4-34, and 4-35 show the velocity vectors, the velocity contours, and pressure coefficient contours around variable-pitch blades for TSRs of λ = 0.5 and 2.0. For a low TSR of λ = 0.5, the high velocity vectors are observed near the blade at $\theta \approx 200°$ (see Fig. 4-36 and 4-37). The separated flow and high velocity from the leading edge of blade caused low pressure coefficient, as shown in Figs. 4-35(a) and 4-38(a). Consequently, the maximum torque coefficient is generated at $\theta \approx 200°$, as shown in Fig. 4-34 (circle b). For the blade at θ = 320°, the flows from suction and pressure side of the blade are observed, because the rotating velocity of the blade is smaller than the

velocity of the uniform flow (see Fig. 4-35(a)). The pressure decreases at the suction side of the blade, and a positive torque is generated near θ = 320° for λ = 0.5 as shown in Fig. 4-34 (circle c). Although the wake of the blades is generated in the upstream area for λ = 0.5, this wake has a smaller influence on the blades in the downstream area compared to that with λ = 2.0. For a high TSR at λ = 2.0, the blade in the upstream area creates a wider wake region (blue areas in Fig. 4-35 (b)) in the downstream area compared to that with λ = 0.5. The wake from the blades has influence pressure coefficient on pressure and suction side. Therefore, the torque at λ = 2.0 is not generated in the downstream area (see Fig. 4-34). It was confirmed by Nobile et al. (2011) that the wakes from the blades in the upstream area develop in the downstream area and a mast interacts with the downstream blades.

A negative torque coefficient was generated at an azimuth angle of 90° ≤ θ ≤ 135° for all TSRs. It can be seen in Fig. 4-38(b) that the difference in the pressure coefficient around a blade at θ = 130° between λ = 0.5 and 2.0 becomes large. The lift force is generated at a low TSR of λ = 0.5 and it is reduced to a tangential force. In contrast, for a high TSR of λ =2.0, there is a slight difference between the pressure coefficients on the suction and pressure sides of the blade due to the low angle of attack, and a negative torque coefficient was consequently generated.

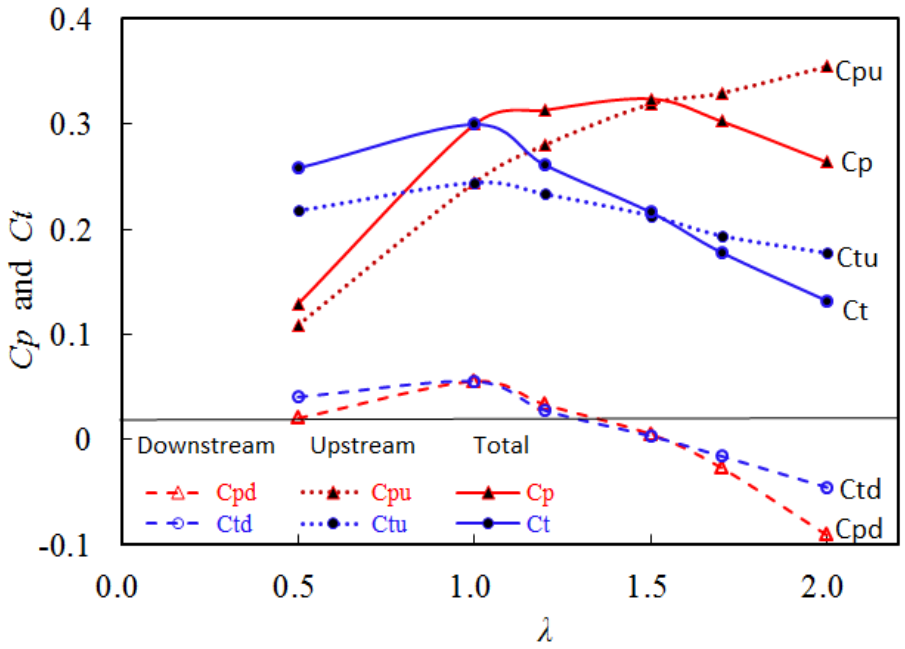

Figure 4-30 Total power coefficient, and the power coefficients in the upstream and downstream areas α_w = ±10.2° (RNG *k-ε* model)

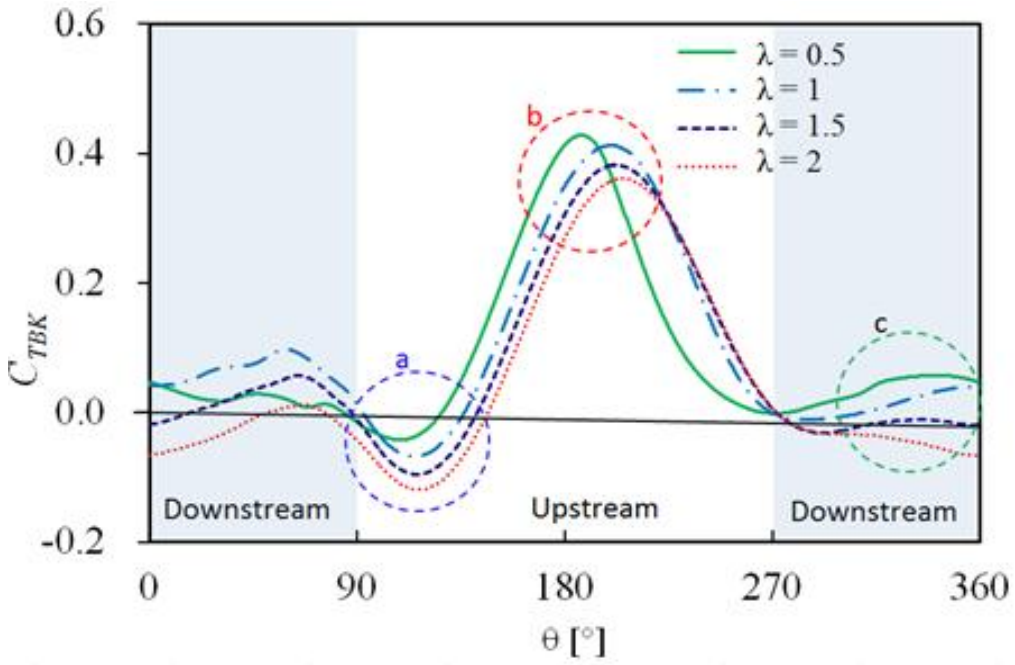

Figure 4-31 Effects of the TSR on the torque coefficients C_{TBK} (θ) for one of the variable-pitch blades with α_w = ±10.2° (RNG k-ε model)

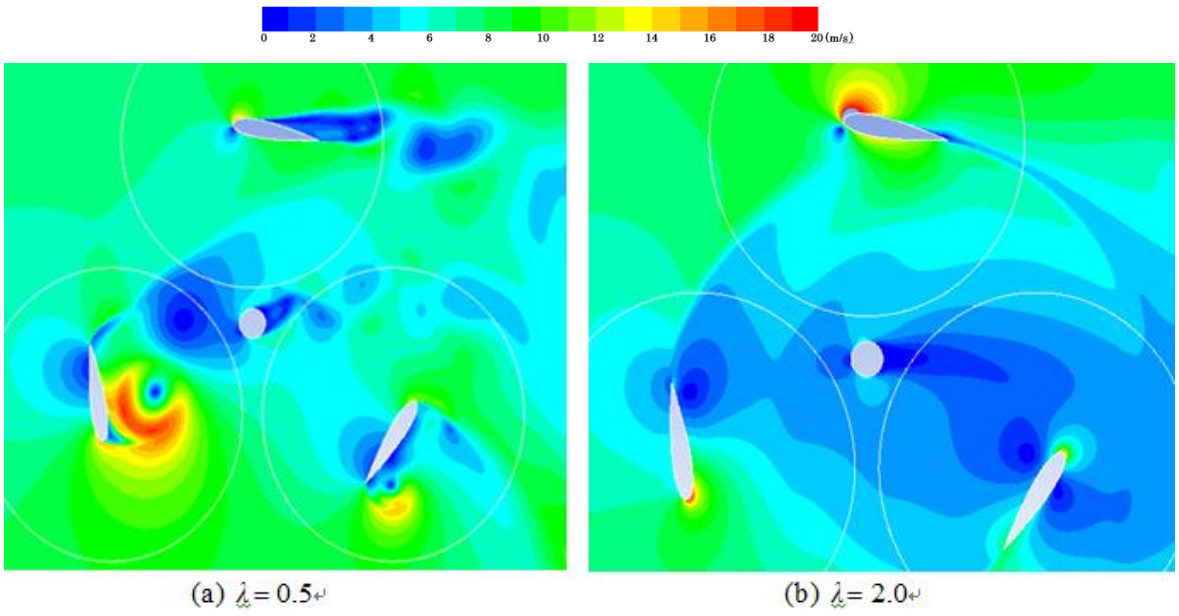

Figure 4-32 Velocity contours around the VAWT with α_w = ±10.2° (RNG k-ε model; θ = 80°, 200°, and 320°)

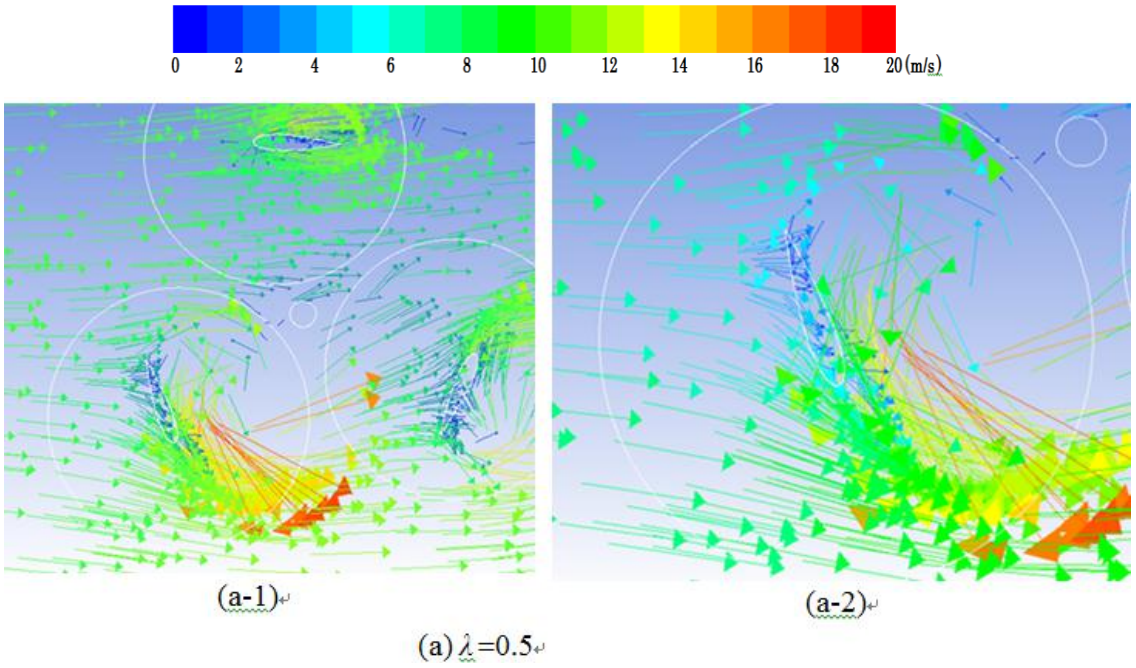

Figure 4-33 Velocity vectors around the VAWT with $\alpha_w = \pm 10.2°$ for low TSR (RNG k-ε model; $\theta = 80°$, 200°, and 320°)

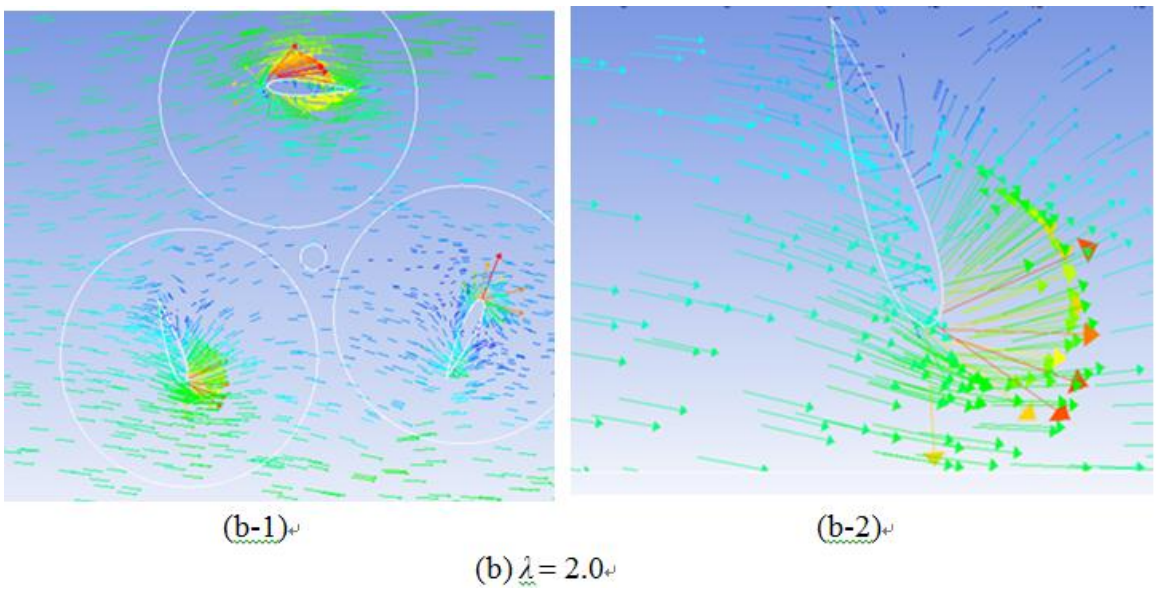

Figure 4-34 Velocity vectors around the VAWT with $\alpha_w = \pm 10.2°$ for high TSR (RNG k-ε model; $\theta = 80°$, 200°, and 320°)

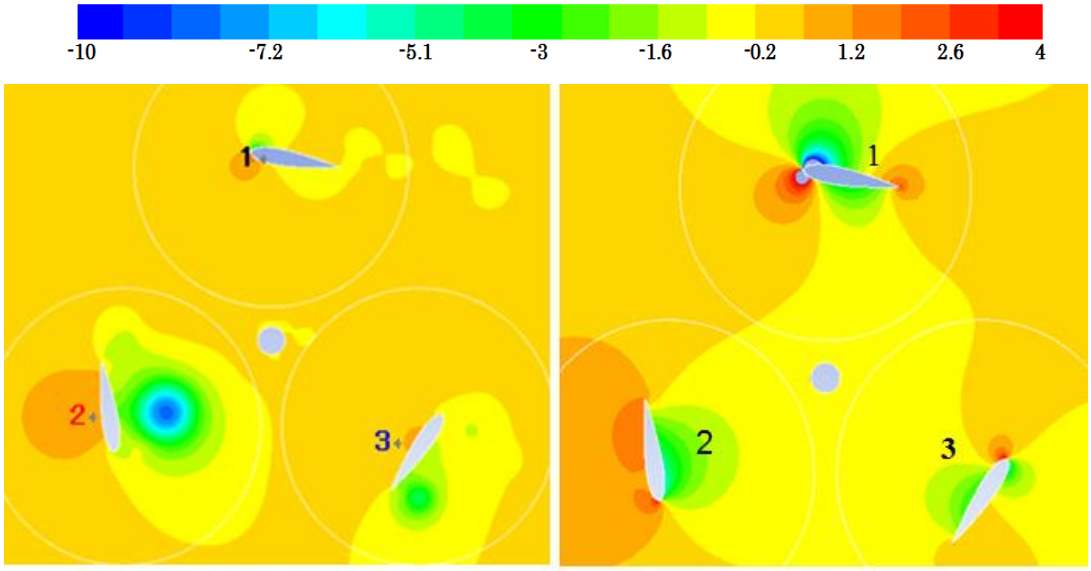

(a-1) $\lambda = 0.5$ (a-2) $\lambda = 2.0$

(a) $\theta = 80°$, 200° and 320°

Figure 4-35 Pressure coefficient contours around the VAWT with $\alpha_w = \pm 10.2°$ (RNG k-ε model)

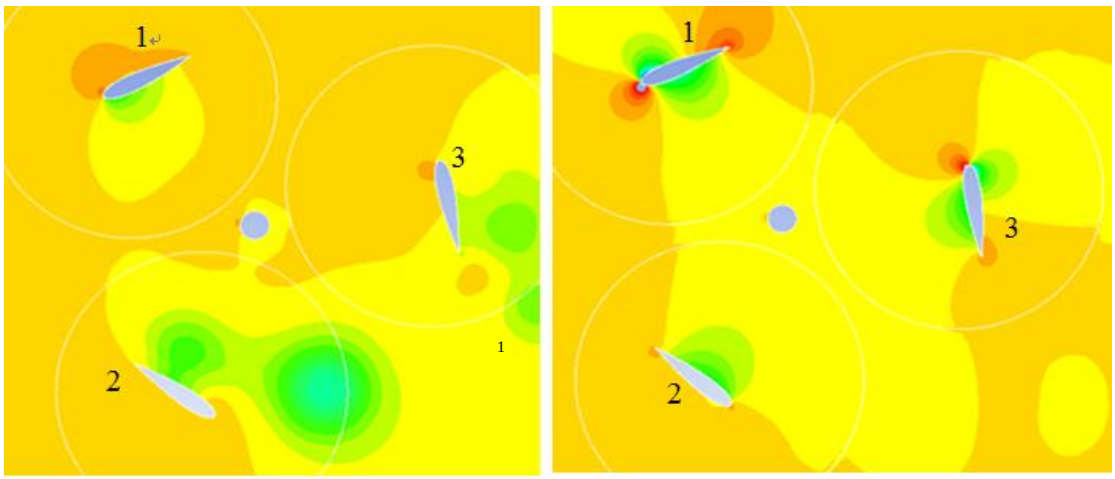

(b-1) $\lambda = 0.5$ (b-2) $\lambda = 2.0$

(b) $\theta = 10°$, 130° and 250°

Figure 4-36 Pressure coefficient contours around the VAWT with $\alpha_w = \pm 10.2°$ (RNG k-ε model)

4.6.5 Dynamic stall on a blade

Figures 4-40 show the vorticity contours around the VAWT with fixed- and variable-pitch blades with $\alpha_w = \pm 10.2°$ at an operating TSR of $\lambda = 1.0$, 1.5, and 2.0 as obtained by using the SST k-ω model. There are four stages of a dynamic stall: initiation of a leading-edge separation, vortex build-up at the leading edge, detachment of the leading-

edge vortex (LEV) and build-up of the trailing-edge vortex (TEV), and detachment of the TEV and breakdown of the LEV (Soerensen et al., 1999). The presence of a vortex on the suction side of a blade creates a low pressure, and consequently, the lift force increases (Larsen et al., 2007). The feature of the dynamic stall that distinguishes it from a static stall is the shedding of significant concentrated vorticity from the leading-edge region. This vortex disturbance subsequently sweeps over the airfoil surface causing a change in pressure and results in a significant increase of the airfoil lift and large nose-down pitching that exceeds static values (Paraschivoiu, 2002).

The dynamic stall flow field at a low TSR can be seen in Figs. 4-40(a) and 4-40(b). An LEV and TEV can be observed on the blades. Fujisawa and Shibuya (2011) showed via PIV that two pairs of counter-rotating vortices develop in the wake of a NACA0018 blade in a straight-bladed VAWT. It was confirmed by Nobile et al. (2011) that the performance of a VAWT at a low TSR is subjected to the phenomenon of a dynamic stall. In contrast, for a high TSR, the absence of both LEV and TEV on the blades leads to the absence of a dynamic stall. Figure 4-40(d) shows the absence of a vortex at a TSR of λ = 1.5 on variable-pitch blades with $\alpha_w = \pm 10.2°$. On the other hand, Fig. 4-40(c) shows the presence of a vortex on fixed-pitch blades with $\alpha_w = \pm 0°$ for a TSR of λ = 1.5. The difference between the presence and absence of vortices at the same TSR for variable- and fixed-pitch blades is due to the amplitude and the rate of increase of the angle of attack. A numerical simulation using the SST k-ω model can also predict the dynamic stall phenomenon, which can identify the presence of vorticity behavior on the rotor blade.

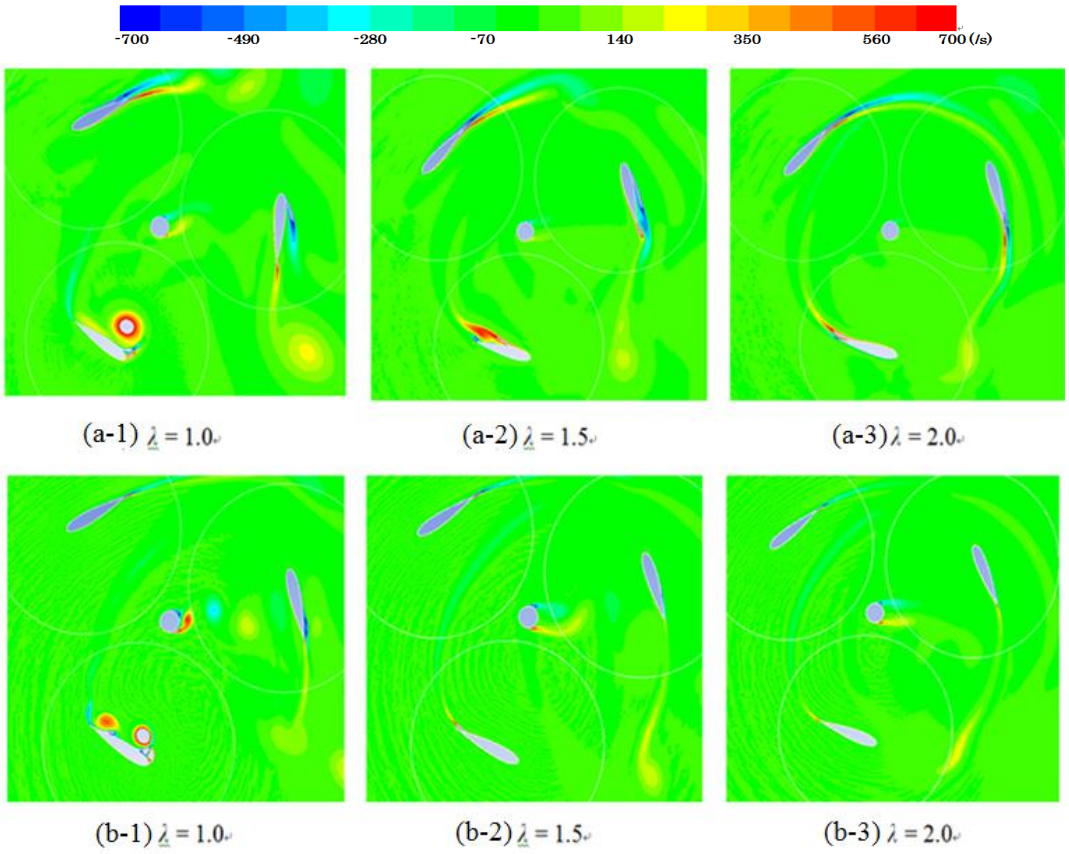

Figure 4-37 Vorticity contours around the VAWT with fixed and variable-pitch blade (SST *k-ω* model, a. $\alpha_w = \pm 0°$ b. $\alpha_w = \pm 10.2°$)

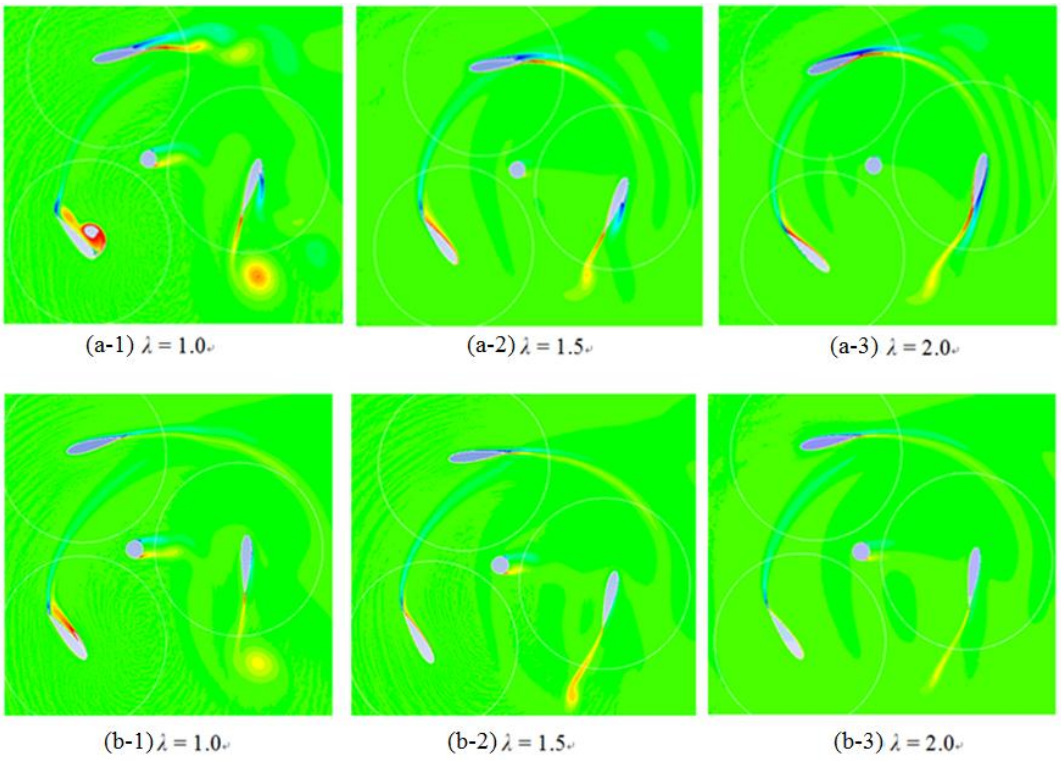

Figure 4-38 Vorticity contours around the VAWT with fixed and variable-pitch blade (RNG *k-ε* model, a. $\alpha_w = \pm 0°$ b. $\alpha_w = \pm 10.2°$)

Chapter 5 Performance and Aerodynamic on Flat-Plate Blades Orthopter Wind Turbines

5.1 Introduction

The world market for small wind turbine has seen further strength growth and common applications of one include; residential, hybrid system, fishery, commercial and industrial [WWEA, 2013]. The vertical axis wind turbine can be classified into two groups according to the method of power generation. The first group is called lift-based power generation such as; Darrieus wind turbine and its variants. The second group is called drag-based power generation such as; Savonius wind turbine and its variants. Generally, HAWTs have higher efficiency than all VAWTs followed by Darrieus turbine and Savonius turbine, [Hau, 2001]. Darrieus turbine has better efficiency than Savonius turbine. However, Savonius turbine has better self-starting than Darrieus turbine and suitable for low speed wind region.

Due to many advantages of both Darrieus turbine and Savonius turbine, it attracts many studies to improvement of both turbines model. [Mohammed M.H., 2010] by optimization of Savonius turbines using an obstacle shielding the returning blade, the power coefficient increase more than 27% and configuration involving a two-blade rotor is better than the three-blade design. The performance analysis of Savonius rotor with twisted blades by [Saha U.K., 2006], showed the potential of the twisted bladed rotor in terms of smooth running, higher efficiency and self-starting capability as compared to that of the conventional bladed rotor. [Hwang et.al, 2006] by optimizing the pitch angle of Darrieus turbine, the lift force increased and power generation increased by 30 percent compared to fixed pitch angle. The author has found that the power coefficient of a VAWT with variable-pitch straight blades that utilize a linkage mechanism is better than one with fixed-pitch blades [Shimizu, 1999].

5.2 Motivation and Objectives

Torque generation of rotor blade of Darrieus and Savonius turbine are vary correspondent to azimuth position. Positive torque of Darrieus turbine mostly generate at upstream area and decreasing power generation at downstream area due to wake effect [Spera, D.A., 2009]. Savonius turbine has positive torque generation at advising blade position or lower side wind area. The drawback of Savonius turbine is negative power in upper wind area due to reverse force on the returning blade.

The vertical axis wind turbine lift-base power has wide range angle of attack (AoA) in one cycle experiences [Spera, D.A., 2009]. The angle of attack of blade rotor beyond the stall of AoA and reduce positive torque generation. One of modification of this type is pitch angle adjusting turbines which gave significant effect on the performance [Bayeul, 2010]. The concept of the orthopter wind turbine is combination of both lift and drag-based power generation. The purpose of the design is to eliminate negative drag and thus positive power contribution of each blade in one rotational cycle. Therefore, the orthopter expected to create positively contributing torque on each blade at every azimuth position due to a rotating movement around its own axis. A previous study by [Bayeul et, al, 2010] confirmed that the performance of this kind of turbine was better than those of classical VAWTs for some specific blade stagger. The arrangement of diffuser of the orthopter study by [Shimizu, 1999] confirmed that the arrangement of diffuser on the top and both sides has good performance. The purpose of the author's is

to investigate of the effects of various parameters such as; aspect ratio, number of blade and tip speed ratio corresponding to performances by experiments and numerical study.

5.3 Methodology

5.3.1 Experimental setup

Figure 5-1 and figure 5-2 shows the apparatus of experiments. The experiments were carried out in an open circuit wind tunnel which has cross section area 1250mm x 1250mm. Wind turbine connect with motor and torque meter. Wind speed measurement use to a thermal probe velocity anemometer. The torque is measured using the torque transducer and converter coupled with the main shaft. Turbine torque (T) was measured at required rotational speeds. A turbine was driven by the variable speed motor under constant wind velocity V_∞ = 10m/s. The rotor of blade using flat plate with thickness ratio 12.5 % at t = 50 mm. the number of blades are n=2, n=3, and n=4. The aspect ratios are AR_1 = 1.0, AR_2 = 1.5, and AR_3 = 2.0 with chord length and length of span are C_1 = 400 mm, C_1 = 400 mm, C_1 = 400 mm, L_1 = 400 mm, L_2 = 290 mm, and L_3 = 228 respectively. Experimental value is taken into account losses due to air resistance of the arm and mechanical loss. The component of the orthopter wind turbine is shown in Figure 5-2.

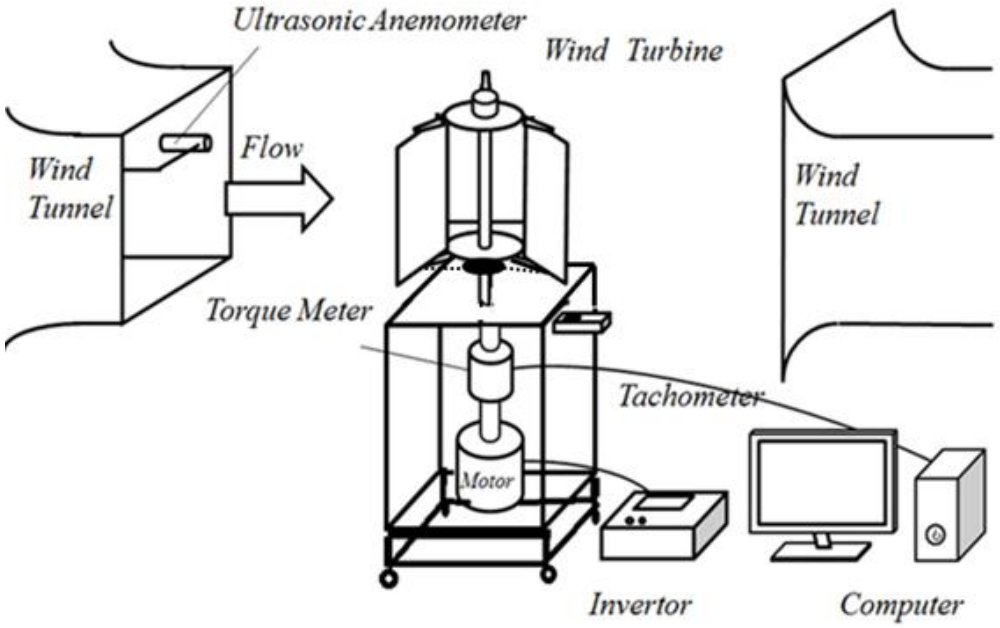

Figure 5-1 Schematic of Experiment Apparatus

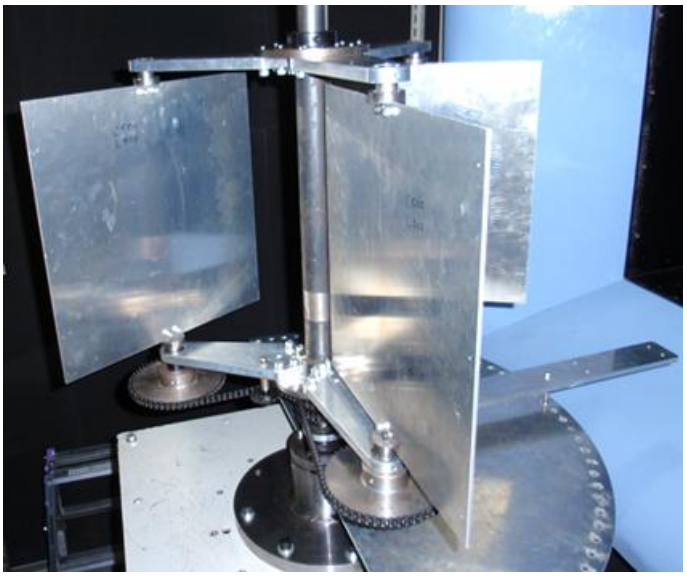

Figure 5-2 Orthopter wind turbine and component

5.3.2 Numerical Technique

The computational domain and the boundary conditions are shown in Figure 5-3. The computational domain consists of three mesh zones. one fixed sub-domain outside the rotor, one dynamic sub-domain around the rotor, and three dynamic sub-domains around the blades with equal spacing of 180°, 120°, and 90° for number of blade n=2, n=3, and n=4 respectively. The mesh was generated using Ansys Meshing. The fixed sub-domain outside the rotor was meshed using quadrilateral grids, and the dynamic sub-domain around the rotor was meshed using triangular grids. The two, three, or four of dynamic sub-domain around the blades were meshed using combination triangular grids and quadrilateral grids especially near surface blades. In order to smallest distance of first layer and high dense on the rotor surfaces, the layers of cells were generated by using an inflation tool which with a grow rate of 1.2. The first layer height is 0.01mm with dimensionless wall distance, $y^+ < 1$.

The numerical simulation of the orthopter wind turbine was performed using the FLUENT ANSYS 13.0 software at the flow conditions corresponding to the experiment. Assuming a two-dimensional, unsteady, incompressible, viscous flow, and no – slip condition on the surface rotor. The rotation of the four dynamic sub-domains can be controlled independently by a user-defined function (UDF), which is programmed in $C++$ code. The solver setting used Transient Pressure Based solver with absolute

velocity. The governing equations were the continuity equation and the Unsteady Reynolds-Averaged Navier-Stokes (URANS) which Reynolds Stresses equations solve using RNG *k*-*ε* (Yakhot V., and Orszag S.A., 1986). The implicit algorithm of the PISO method was applied for pressure-velocity coupling. Spatial Discretization scheme, Least Squares Cell Based was chosen for gradient with pressure set standard. QUICK discretization method was set for momentum, turbulent kinetic energy and turbulent dissipation rate

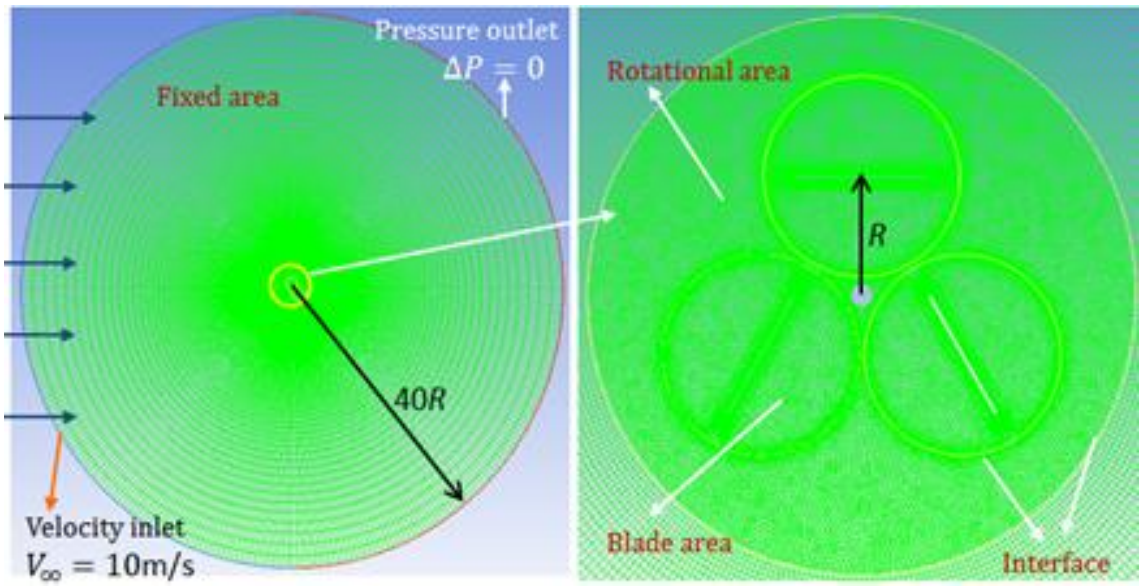

Figure 5-3 Meshing grid and boundary condition

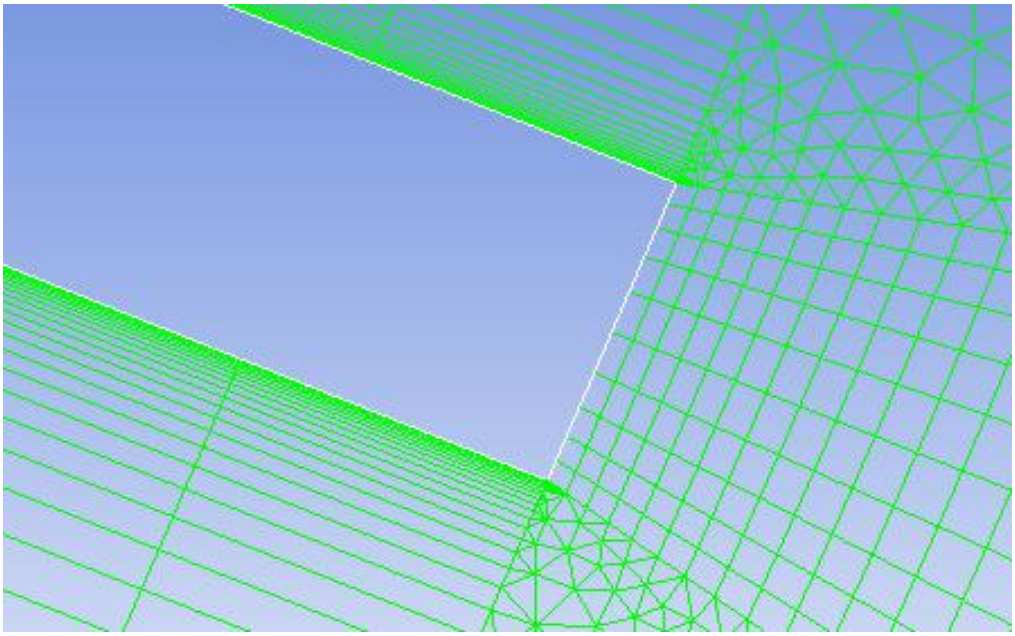

Figure 5-4 Refining of grid near surface blade

5.3.3 Experiment and Simulation Cases

Three different of aspect ratio configuration and number of blade were investigated. The aspect ratio is defined ratio span of blade to chord length of blade, $AR = L/c$. The swept area is defined effective area of wind incoming trough into the rotor, in this case total width is $(2R+0.5C)$ with height of rotor (L). Figures 5-5 and 5-6 show detail of aspect ratio and swept area of rotor blade. Case 1 is rotor blade using three of number of blade, n=3 with aspect ratio; $AR_1 = 1$, $AR_2=1.5$, and $AR_3 =2$ respectively. Case 2 is rotor blade using three different configuration of number of blade n= 2, n=3, and n= 4 respectively, with aspect ratio $AR = 1.5$

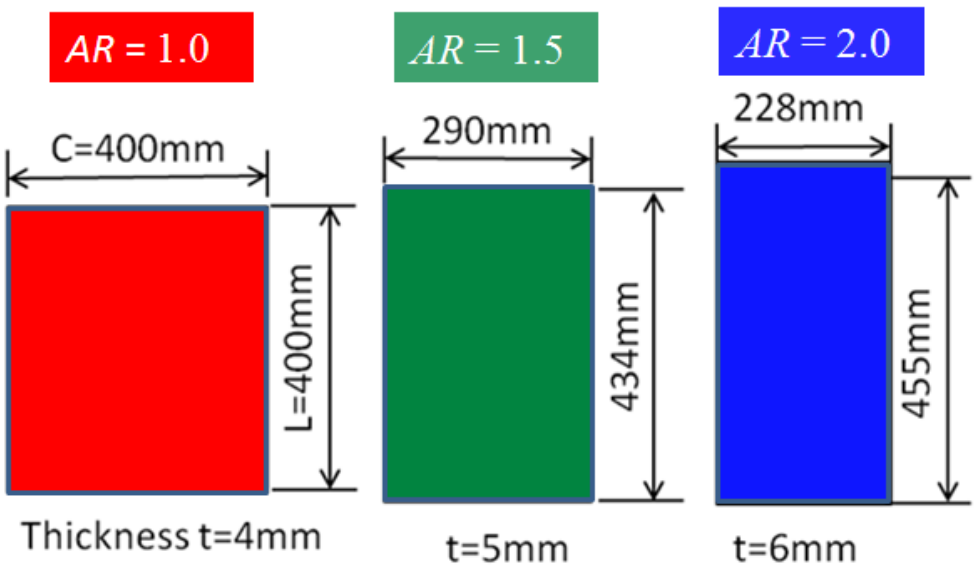

Figure 5-5 Aspect ratio of rotor blade

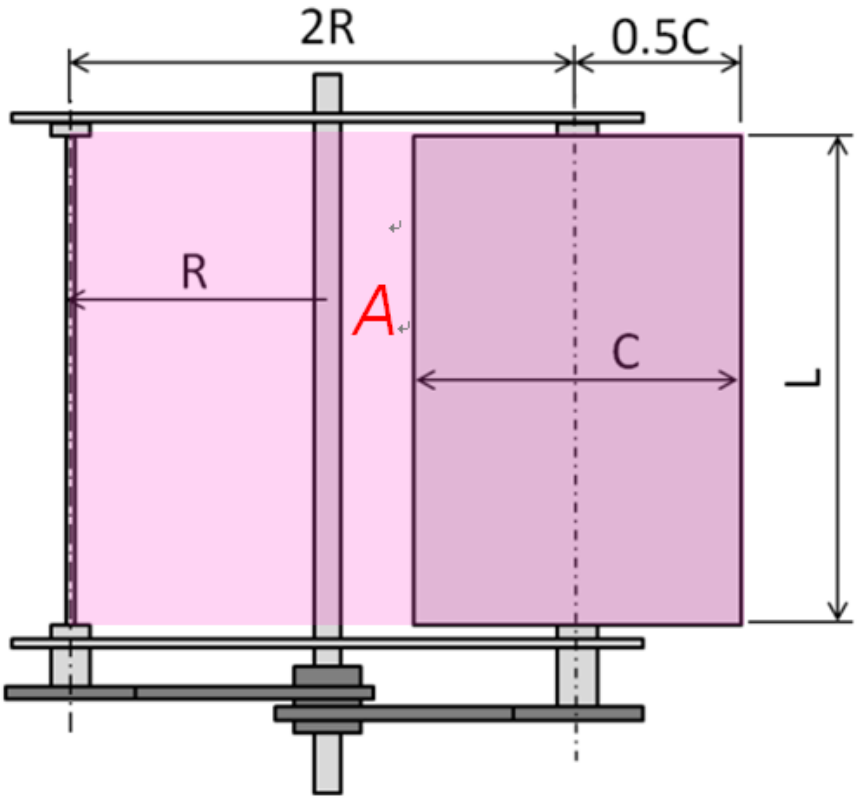

Figure 5-6 Swept area of rotor turbine

.

Result and Discussion

5.3.4 Effect of aspect ratio on the performance

Figure 5-7. presents aspect ratio leads to power and torque coefficients for rotor blade n=3. The highest of power coefficient at aspect ratio *AR* =1.0 followed by *AR* = 1.5 and *AR* = 2.0. The aspect ratio defined ratio chord length per length of blade span. In this study chord length and length of span are various. For instant *AR* =1.0 has chord length *c* = 400 mm, while for *AR* =1.5 and *AR* = 2.0 have *c* = 290 mm and *c* = 228 mm respectively. Consequently, the radius of rotor is more for low aspect ratio and lead to moment addition in positive torque generate area.

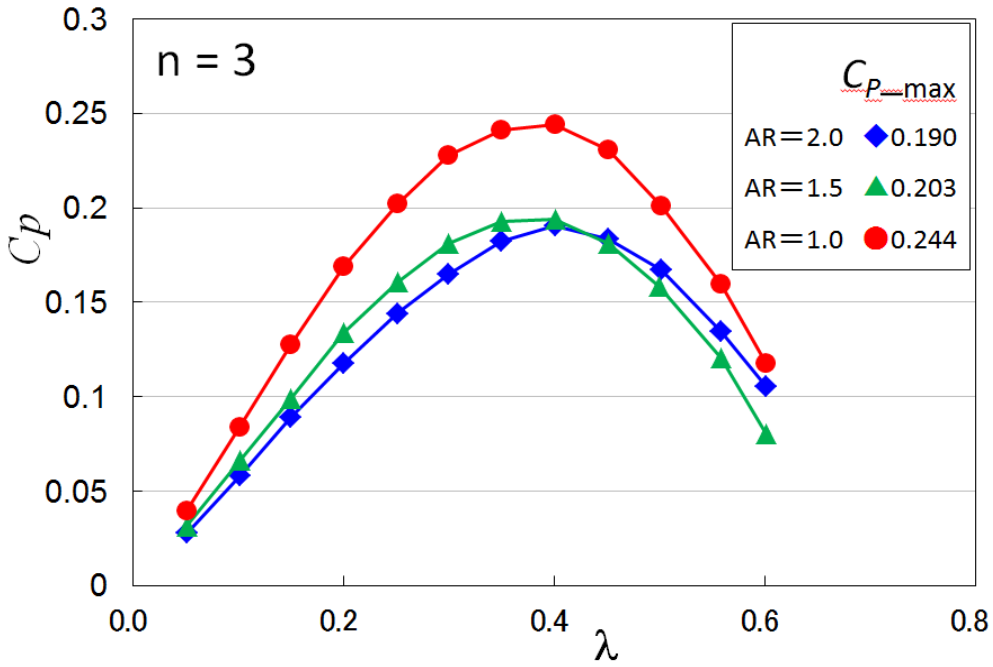

Figure 5-7 Effect aspect ratio on the coefficient of performance

5.3.5 Power coefficient of experiment and numerical results

Figure 5-8 shows the influences of number of blades of rotor and tip speed ratio corresponding to the coefficient performance due to revolution torque of numerical result. Figure 5-9 shows the influences of number of blades of rotor and tip speed ratio corresponding to the coefficient performance due to rotation torque of blade of numerical result. Figure 5-10 shows total the coefficient performance of numerical result due to revolution torque and rotation torque of blades. Figure 5-11 shows the influences of number of blades of rotor and tip speed ratio corresponding to the coefficient performance of experimental result. The highest performance is the rotors which have three

and four blades compared to the rotor have two blades. The peak of coefficient performance for the rotor have two, three, and four blades occur at $\lambda \approx 0.4$ which the rotor have two blades, the peak of performance coefficient shift to right slightly. The influence of number of blades was not significant for high tip speed ratio especially $\lambda \geq 0.4$ due to wake effects. The effect of number of blade of V-axis Sail wing was done by [Nemoto et al, 2002] which the highest performance was the rotor has four blades. The simulation can predict the performance of VAWT affected by number of blades rotor as shown in Figures 5-10. The patterns of performance coefficient have a good agreement with experiment result. However, there are small differences of performance affected by number of blades which the lowest performance is the rotor has two blades. The values of *Cp* of numerical results was higher compare with *Cp* of experiment result due to many factor such as two dimensional, effect tip vortices, smooth surface of blades, and etc. The power coefficients increased as increase tip speed ratio until $\lambda = 0.4$ and decrease as increase tip speed ratio for both experiment and numerical results. This confirmed by numerical results for straight blades with zero stagger angle by [Bayeul et al, 2011] which the peak of power coefficient occur at a tip speed ratio $\lambda = 0.4$.

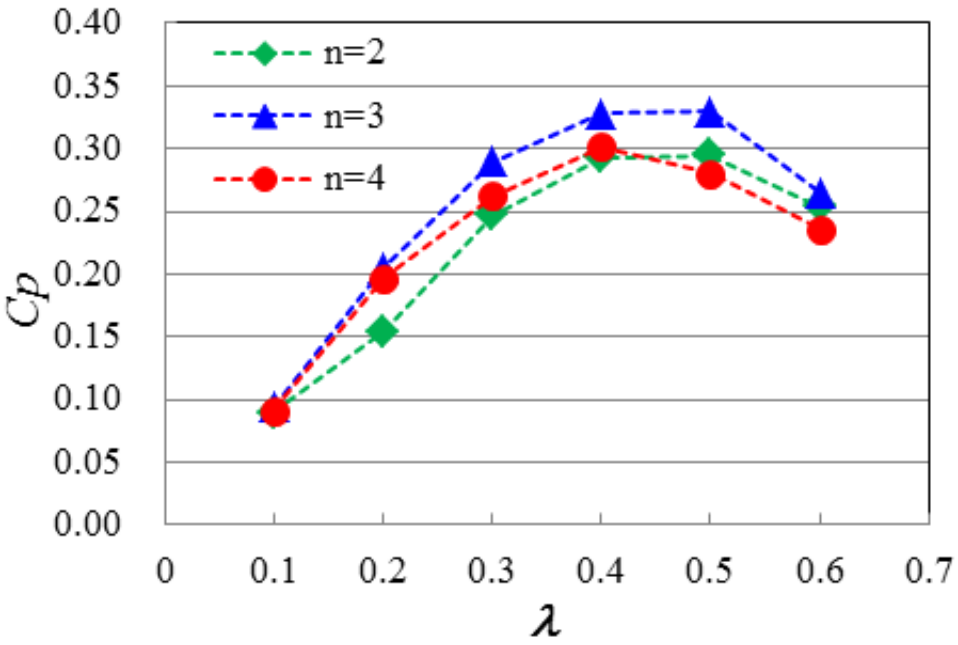

Figure 5-8 Performance coefficient on turbine due to revolution torque

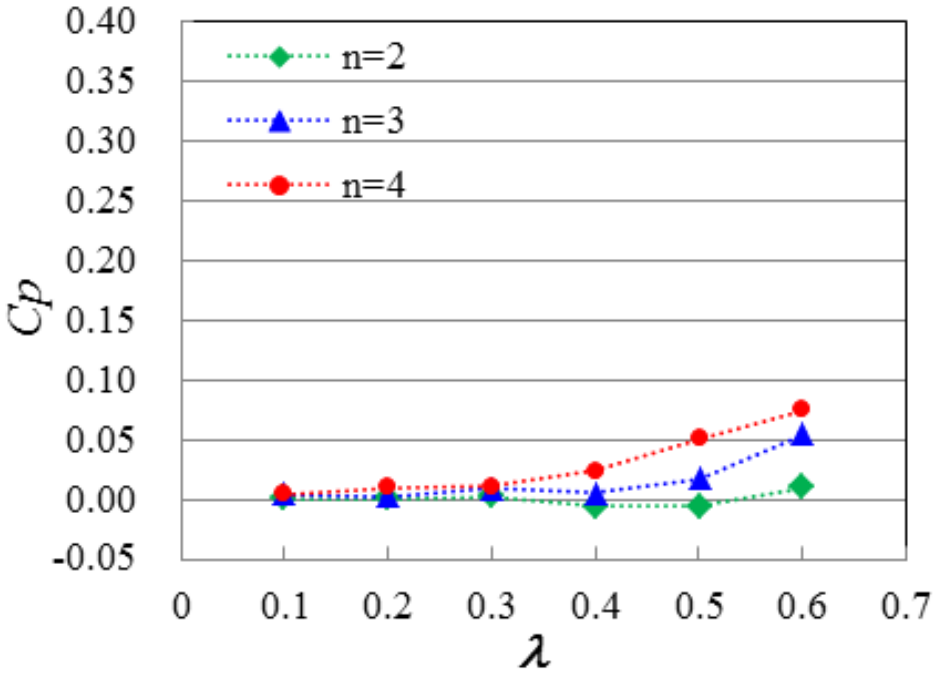

Figure 5-9 Performance coefficient on turbine due to rotation torque

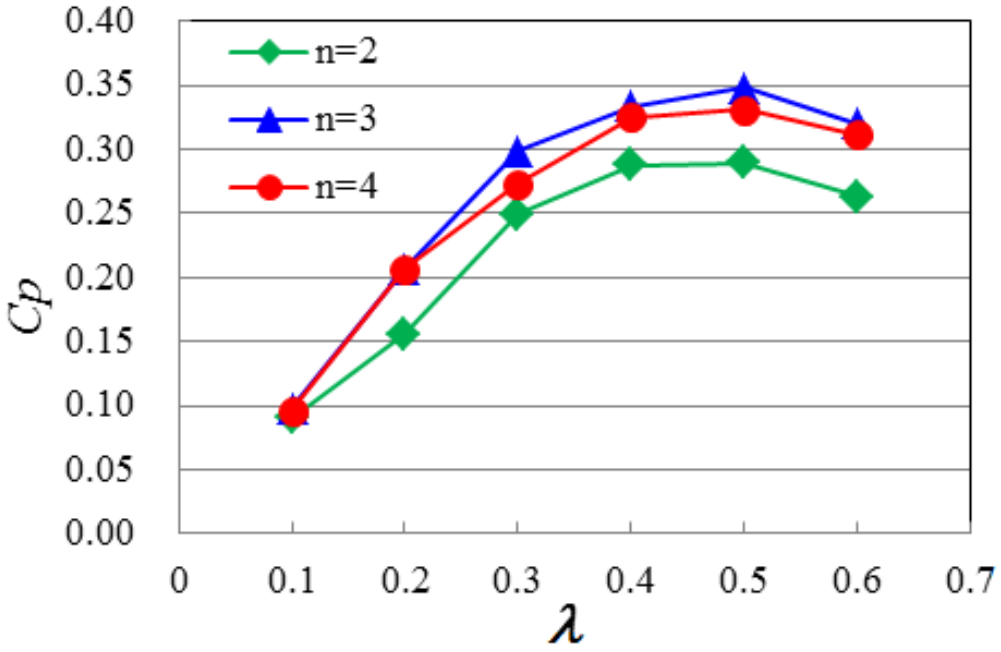

Figure 5-10 Total performance coefficient of numerical result

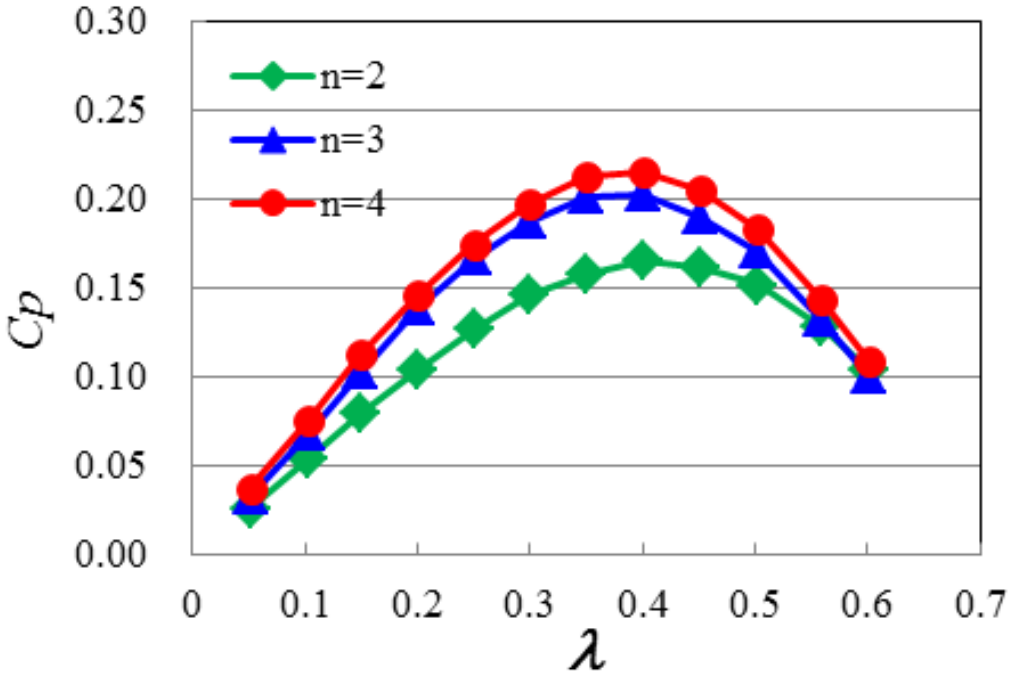

Figure 5-11 Performance coefficient of experiment result

5.3.6 The number of blade effect on the torque coefficient

The vertical axis wind turbine has high positive torque zone (HTZ) which this position high torque generate corresponding azimuth position based on type of wind turbine. For instant, the lift type VAWT has HTZ between $\theta = 120^{\circ}$ and $\theta = 270^{\circ}$ and for the drag-type VAWT has HTZ between $\theta = 180^{\circ}$ and $\theta = 360^{\circ}$. The orthopter wind turbine has combination for both type and has wide range of HTZ. In previously, tip speed ratio affect to HTZ start which high tip speed ratio has delay start. Figure 5-12 and Figure 5-13 show the effects of number of blade lead torque coefficient for tip speed ratio $\lambda = 0.4$ and $\lambda = 0.6$ respectively. There are different start of HTZ for number of blade n= 2, n=3, and n=4 which first start is n=2 followed by n=3 and n=4. The start delay of HTZ for n=3 and n=4 due to affected by previously blade which create disturbance of induced flow as seen in Fig 5-14 (a-1), Fig 5-14 (b-1)and Fig 5-14 (c-1). The difference of static pressure on the suction side and discharge side of blade is very big for n= 2 followed by n= 3 and n=4 as seen in Fig 5-14 (a-2), Fig 5-14 (b-2) and Fig 5-14 (c-2). Similarly, for blade at position between $\theta = 180^{\circ}$ and $\theta = 240^{\circ}$ the high torque is n= 2 followed n= 3 and n =4. The high torque for n=2 still exist when blade position between $\theta = 240^{\circ}$ and $\theta = 300^{\circ}$ which this position transform lift-type to drag-type. This phenomena due

to affected by static pressure on discharge side of previous blade lead to the static pressure on the suction side blade. The effect of tip speed ratio and number of blade can be seen in Figure 5-13, which the different torque for n=2, n=3, and n=4 slightly decrease compare to low tip speed ratio λ= 0.4 in Figure 5-12. The most significant difference between two- and three-bladed rotors or more is that the rotor torque ripple, which has a distinctive twice-per-revolution oscillation for a two-bladed VAWT, is almost eliminated in a three-bladed rotor or more [2].

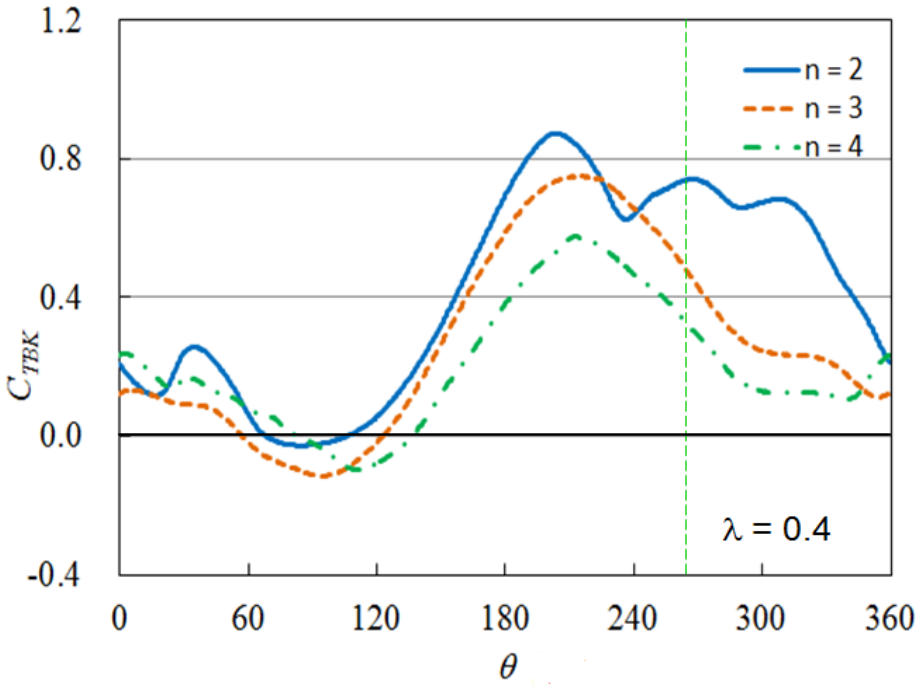

Figure 5-12 Effect number of blade on torque generation at low TSR

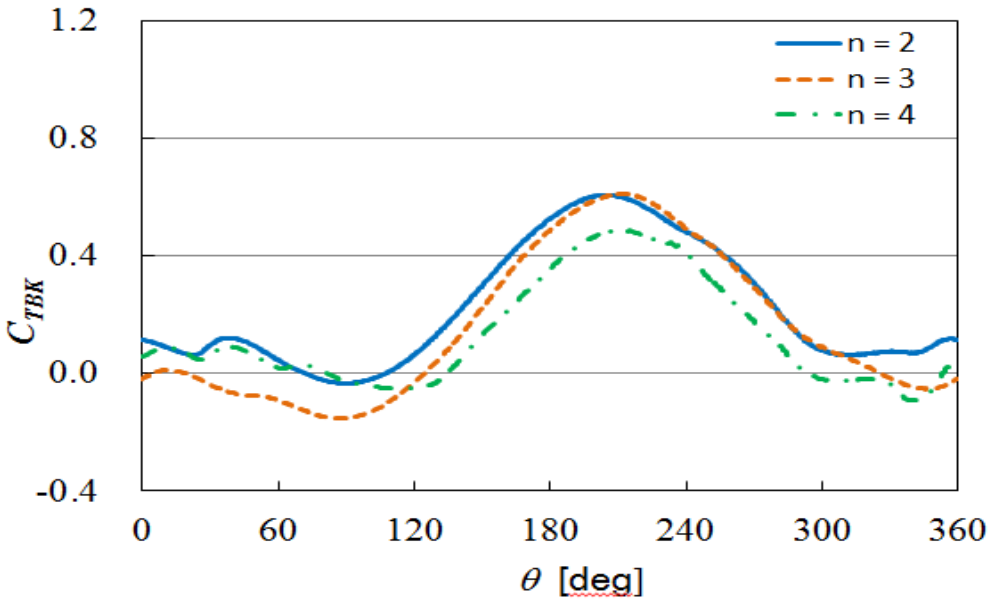

Figure 5-13 Effect number of blade on torque generation at high TSR

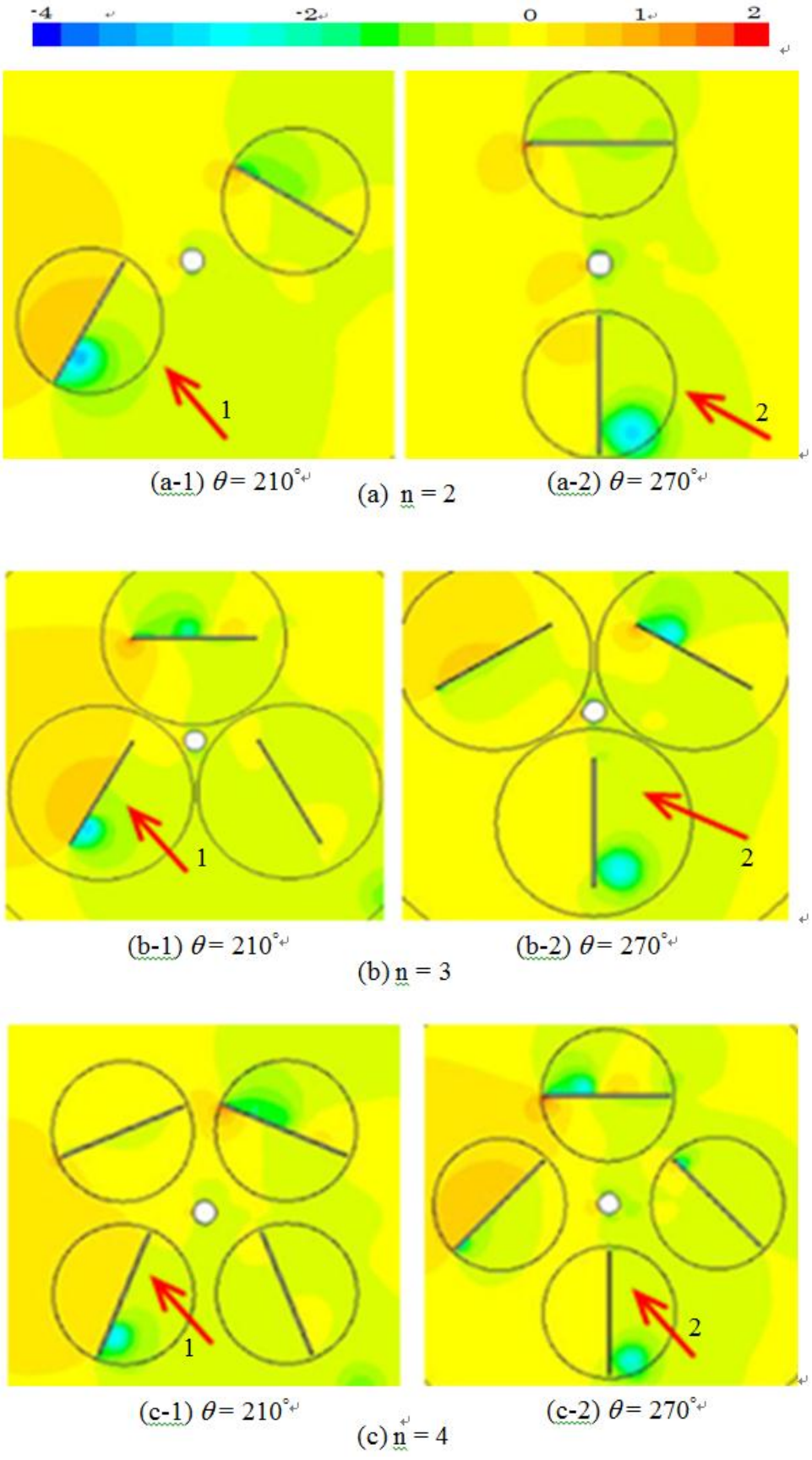

Figure 5-14 Pressure coefficient contour of the rotor blades

5.3.7 Effect solidity on the performance coefficient

The solidity on the VAWTs is defined ratio total area of rotor blade to circumference area of one. Figure 5-15 show effect solidity on the maximum performance coefficient of turbine. The increase of solidity give significant effect on the peak of performance coefficient until σ= 0.8 and then decrease as increase of one.

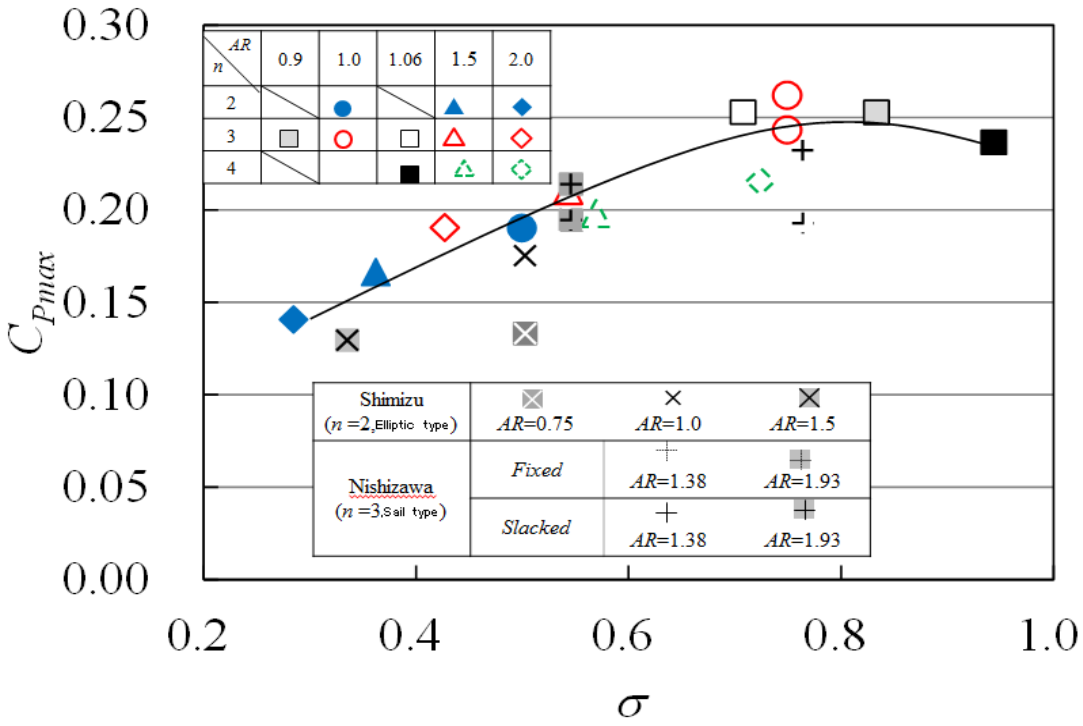

Figure 5-15 Effect solidity on the maximum of performance coefficient

5.3.8 Effect tip speed ratio on the torque coefficient

The orthopter wind turbine has wide range angle of attack of blade in one cyclic experience. The blade rotate opposite direction with main shaft rotation ω_1 which relative angular velocity of blade rotation its own axis ω_2 equal a half angular velocity main rotation shaft ω_1. Thereby, the pitch angle of blade is change relative to azimuth angle. In present study, the pitch angle of blade set $\alpha_p = 45^\circ$ relative to asymptote of path line of blade at azimuth angle position $\theta = 0^\circ$. Consequently, when $\theta = 90^\circ$,$\theta = 180^\circ$, and $\theta = 270^\circ$ the pitch angle of blade $\alpha_p = 0^\circ$, $\alpha_p = 45^\circ$, and $\alpha_p = 90^\circ$ respectively. The change of pitch angle of blade can reduce angle of attack of blade compare with fixed-pitch Darrieus wind turbine. The orthopter wind turbine is combination between drag-type

and lift-type vertical axis wind turbine. Similarly with Darrieus wind turbine, the angle of attack (AoA) decrease as increase tip speed ratio (λ). However, due to blade rotation its own axis in the orthopter wind turbine, the blade AoA more decrease as increase tip speed ratio compare to fixed-pitch Darrieus wind turbine. In Figure 5-16 presents the tip speed ratio affects to torque coefficient (C_T) for number of blade n=3. The lift-type VAWT has the lowest negative torque at azimuth angle position $\theta = 90^{\circ}$ because resultant of relative flow velocity is highest and direction of one is perpendicular to radius of main axis. There for the drag at this position is maximum and tip speed ratio is also contributes to resultant of relative flow velocity is higher. When the blade at position between $\theta = 330^{\circ}$ and $\theta = 90^{\circ}$, the positive torque generate only for tip speed ratio λ= 0.2 and λ= 0.4, while negative torque generate for high tip speed ratio λ= 0.6 due to effect drag is dominant corresponding to angle of attack. The high torque generate start from $\theta = 120^{\circ}$ and finish at $\theta = 360^{\circ}$ for low tip speed ratio λ= 0.2 . While for tip speed ratio λ= 0.4 and λ= 0.6 start from $\theta = 140^{\circ}$ and finish faster for tip speed ratio λ= 0.4 followed by tip speed ratio λ = 0.6

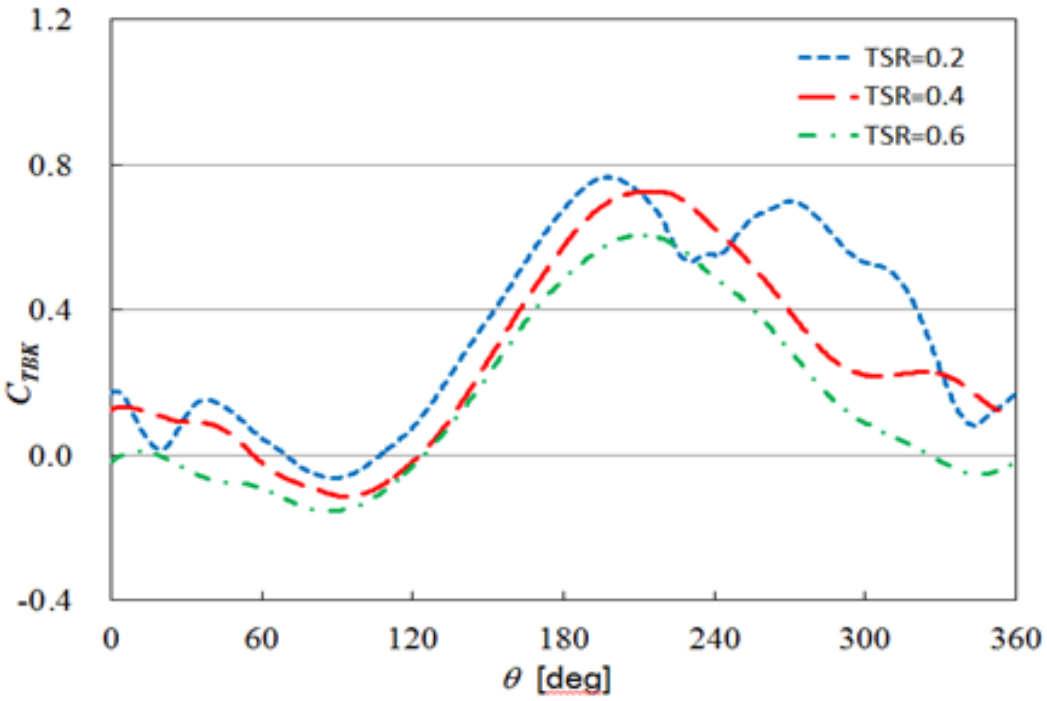

Figure 5-16 Effect tip speed ratio on the torque coefficient

Chapter 6 Conclusion

The effects of the variable pitch angle, TSR, and turbulent model on the performance of a Darrieus wind turbine and the unsteady flow around the blades was investigated using a two-dimensional numerical simulation. The numerical simulation of the power performance results were validated using wind tunnel experimental data. The following conclusions were drawn:

(1) The prediction of performance by numerical simulation using the RNG k-ε turbulence model qualitatively agreed with the experiment. It was found that a VAWT with variable-pitch blades has better performance than a VAWT with fixed-pitch blades.

(2) The performance of a VAWT is influenced by the amplitude and the rate of increase of the angle of attack. Reducing the angle of attack improves the torque coefficient, especially in the upwind area and some areas downstream, where a positive torque is generated on the VAWT with variable-pitch blades.

(3) For a low TSR of $\lambda < 1.5$ in a VAWT with variable-pitch blades, positive power is generated in both the upstream and downstream areas. For a high TSR of $\lambda > 1.5$, the downstream power coefficient becomes negative, and the power coefficient decreases as the TSR increases.

(4) The RNG k-ε turbulence model can capture the presence of a vortex on the blade rotor at low TSRs. A VAWT with variable-pitch blades can significantly suppressed the leading and trailing-edge separation as compared to a VAWT with fixed-pitch blades.

The effects of aspect ratio, TSR, and number of blade on the performance of the Orthopter were investigated by wind tunnel experiment and the unsteady flow around the blades and predict performance influences by TSR and number of blade were investigated using a two-dimensional numerical simulation. The following conclusions can be reveals;

(1) The performance of the orthopter influenced by aspect ratio, which the highest performance is the rotor has AR =1

(2) The prediction of performance by numerical simulation using the RNG k-ε turbulence model qualitatively agrees with the experiment. It was found that the performance affected by number of blades and tip speed ratios.

(3) The high tip speed ratio lead to reducing torque generation specially at downstream area

(4) The simulations show effects of number of blade on the performance. The high number of blade reduces torque generation of one blade. However, the overall of performance is increased

Appendix A

Nomenclature

a : Ratio induced velocity to free-stream velocity
AR : Aspect ratio of blade (= h/c)
C_{Lt} : Tangential lift coefficient
C_{Dt} : Tangential drag coefficient
C_p : Turbine power coefficient (=$T\omega/\rho RhV^3$)
C_{pu} : Turbine power coefficient in the upstream area (=$\frac{n\lambda}{2\pi}\int_{\frac{\pi}{2}}^{\frac{3\pi}{2}} C_{TBK}d\theta$)
C_{pd} : Turbine power coefficient in the downstream area (=$\frac{n\lambda}{2\pi}\int_{-\frac{\pi}{2}}^{\frac{\pi}{2}} C_{TBK}d\theta$)
C_t : Turbine torque coefficient (=$T/\rho R^2hV^2$)
C_{tu} : Turbine torque coefficient in the upstream area (=$\frac{n}{2\pi}\int_{\frac{\pi}{2}}^{\frac{3\pi}{2}} C_{TBK}d\theta$)
C_{td} : Turbine torque coefficient in the downstream area (=$\frac{n}{2\pi}\int_{-\frac{\pi}{2}}^{\frac{\pi}{2}} C_{TBK}d\theta$)
C_{TBK} : Turbine torque coefficient of one blade
c : Blade chord length
D : Turbine diameter
h : Blade span length
l_c : Blade link length
l_e : Eccentric link length
l_m : Main link length
l_s : Second link length
N : Turbine rotational speed
N : Number of blades
P : Static pressure at a point
p_∞ : Static pressure at free stream
R : Turbine radius
RNG : Renormalization group
SST : Shear stress transport
T : Turbine torque
T_c : Turbine mechanical loss torque
V_∞ : Wind speed
V_i : Induced Velocity
$\boldsymbol{V_t}$: Tangential velocity ($|\boldsymbol{V_t}| = R\omega$)
$\boldsymbol{W}$: Local relative velocity vector ($W = V_i + \boldsymbol{V_t}$)
α : Geometrical angle of attack
α_c : Blade offset pitch angle
α_p : Blade pitch angle
α_w : Blade pitch angle amplitude
θ : Azimuth angle (angle between the main-link and x-axis)
λ : Tip speed ratio (= $R\omega/ V_\infty$)
ρ : Air density
ρ_∞ : Air density of free stream
σ : Turbine solidity (= $nc/2\pi R$)
ω : Turbine angular velocity (= $2\pi N/60$)

References

1. Almohammadi, K.M., Ingham, D.B., Ma, L. and Pourkashan, M., Computational fluid dynamics (CFD) mesh independency techniques for a straight blade vertical axis wind turbine, Energy, Vol.58 (2013), pp.483-493.
2. Anderson, J., The 40kW Giromill, Proceedings Small Wind Turbine Systems, (1981), pp.93-105.
3. ANSYS FLUENT Theory Guide, ANSYS, Inc. Release 14.5, Southpointe, October 2012, 275 Technology Drive Canonsburg, PA 15317 ANSYS, Inc.
4. Aresti, L., Tutar, M., Chen, Y., and Calay, R. Computational study of a small scale vertical axis wind turbine (VAWT): Comparative performance of various turbulence models, *Wind and Structures*, Vol.17, No.6(2013), pp.647-670.
5. Castelli, M.R., Englaro, A. and Benini, E., The Darrieus wind turbine: Proposal for a new performance prediction model based on CFD, Energy, Vol.36 (2011), pp.4919-4934.
6. Chen, C.C. and Kuo, C.H., Effects of pitch angle and blade camber on flow characteristics and performance of small-size Darrieus VAWT, Journal of Visualization, Vol.16, Issue 1 (2013), pp. 65-74.
7. Chen,W. and Zhou, C.Y., Application of numerical simulation to obtain the optimization pitch angle for VAWT, Proc. 1st World Non-Grid-Connected Wind Power and Energy Conference, Nanjing, China: IEEE Computer Society, (2009), pp. 4244-4702.
8. Chong, W.T., Fazlizan,A. Poh,S.C., Pan,K.C., Hewb, W.P. and Hsiao,F.B., The design, simulation and testing of an urban vertical axis wind turbine with the omni-direction-guide-vane, Applied Energy, Vol.112 (2013), pp.568-575.
9. Fujisawa, N. and Shibuya, S., Observations of dynamic stall on Darrieus wind turbine blades, Journal of Wind Engineering and Industrial Aerodynamics, Vol.89 (2001), pp. 201–214.
10. Howell, R., Qin, N., Edward, J. and Durrani, N., Wind tunnel and numerical study of a small vertical axis wind turbine, Renewable Energy, Vol.35 (2010), pp.412–422.
11. Ross, I. and Altman, A., Wind tunnel blockage corrections: Review and application to Savonius vertical-axis wind turbines, Journal of Wind Engineering and Industrial Aerodynamics, Vol.99 (2011), pp.523–538.

12. Kiwata, T., Yamada, T., Kita, T., Takata, S., Komatsu, N. and Kimura, S., Performance of a vertical axis wind turbine with variable-pitch straight blades utilizing a linkage mechanism, Journal of Environment and Engineering, Vol.5, No.1 (2010), pp.213-224.
13. Larsen, J.W., Nielsen, S.R.K. and Krenk, S., Dynamic stall model for wind turbine airfoil, Journal of Fluid and Structures, Vol. 23 (2007), pp.959-982.
14. Leifur Leifsson, Variable-Fidelity Aerodynamic Shape Optimization, Computational Optimization, Methods and Algorithms Studies in Computational Intelligence Volume 356, 2011, pp 179-2102011
15. McNaughton, J. Billard, F. and Revell, A., Turbulence modelling of low Reynolds number flow effects around a vertical axis turbine at a range of tip-speed ratios, Journal of Fluids and Structures, Vol.47 (2014), pp.124-138.
16. Menter F. R., Two-equation eddy-viscosity turbulence models for engineering applications, AIAA Journal, Vol.32, No.8 (1994), pp.1598–1605.
17. Mertens, S., Wind energy in the built environment: Concentrator effects of buildings, TU Delft, (2006), pp.3-14, Multi-Science.
18. Mewburn-Crook, A., The design and development of an augmented vertical wind turbine, School of Mechanical, Aeronautical and Production Engineering, (1990), pp.1-59.
19. Montreal Premiere. (n.d.). First Affordable Wind Turbines for Metropolis. Retrieved August 2012, from Montreal Premiere: http://www.montreal-prem1ere.com
20. M.H. Mohamed , G. Janiga , E. Pap , D. Thévenin, Optimization of Savonius turbines using an obstacle shielding the returning blade, Renewable Energy, Volume 35, Issue 11, November 2010, Pages 2618–2626
21. Nattuvetty, V. and Gunkel, W.W., Theoretical performance of a straight-bladed cycloturbine under four different operating conditions, Wind Engineering, Vol.6, No.3 (1982), pp.110-130.
22. Nazary, H., Aalipour, N., Alizadeh, M., A numerical study of the flow through a butterfly valve, International Journal of Energy & Technology 3 (37) (2011) 1–9
23. Nobile, R., Vahdati, M., Barlow, J. and Mewburn-Crook, A dynamic stall for a vertical axis wind turbine in a two-dimensional study, Proceedings of World Renewable Energy Congress (2011), pp.4225-4232.

24. Noll, R.B. and Zvara, J., High-reliability vertical-axis wind turbine, Proceedings Small Wind Turbine Systems 1981, (1981), pp.17-28.
25. Paraschivoiu, I., Wind Turbine Design: With Emphasis on Darrieus Concept, Polytechnic International Press, (2002).
26. Patel, S., Patel, D.S., Application of CFD in STHE, International Journal of Engineering Science and Innovative Technology (IJESIT) Volume 3, Issue 2, March 2014.
27. Pawsey, N.C.K., Development and evaluation of passive variable-pitch vertical axis wind turbines, PhD Thesis, Univ. New South Wales, Australia, (2002).
28. Qin, N., Howell, R., Durrani, N., Hamada, K., Smith, T., Unsteady Flow Simulation and Dynamic Stall Behavior of Vertical Axis Wind Turbine Blades, Wind Engineering, Vol.35, No. 4, pp.510- 511(2011).
29. Roh S.C. and Kang S.H. "Effects of a blade profile, the Reynolds number, and the solidity on the performance of a straight bladed vertical axis wind turbine" Journal of Mechanical Science and Technology 27 (11) (2013) 3299~3307 www.springerlink.com/content/1738-494x DOI 10.1007/s12206-013-0852-x
30. Saha. U.K., and Jaya Rajkumar Ã, M., On the performance analysis of Savonius rotor with twisted blades, Renewable Energy 31 (2006) 1776–1788.
31. Sato,Y., Okazaki,H., Shoda,T., Nishio,Y., Shigeta,M. and Izawa,S., Hotwire measurement and numerical analysis of flows around a straight wing vertical axis wind turbine, Transactions of the Japan Society of Mechanical Engineers, Series B, Vol.77, No.775 (2011), pp.637-646 (in Japanese).
32. Savonius, S. J.: "The S-Rotor and Its Applications," Mechanical Engineering, Vol. 53, No. 5, May 1931, pp. 333-338.
33. Sheldahl, R.E. and Klimas, P.C., Aerodynamic characteristics of seven symmetrical airfoil sections through 180-degree angle of attack for use in aerodynamic analysis of vertical axis wind turbines. Sandia National Laboratories energy report: SAND80-2114 (1981).
34. Shih, T. H., Liou, W.W., Shabbir, A., Yang, Z. and Zhu, J., A new k- ε eddy-viscosity model for high Reynolds number turbulent flows - model development and validation, Computers Fluids (1995), 24(3), pp. 227–238.

35. Simão Ferreira, C., van Bussel, G. and van Kuik, G., 2D CFD simulation of dynamic stall on a vertical axis wind turbine: verification and validation with PIV measurements, 45th AIAA Aerospace Sciences Meeting and Exhibit, (2007), pp. 1-11.
36. Simão Ferreira, C., van Zuijlen, A., Bijl, H., van Bussel, G. and van Kuik, G., Simulating dynamic stall in a two-dimensional vertical-axis wind turbine: verification and validation with particle image velocimetry data, Wind Energy, Vol. 13, No. 1, (2010), pp. 1-17.
37. Simão Ferreira, C., van Kuik, G., van Bussel, G. and Scarano, F., Visualization by PIV of dynamic stall on a vertical axis wind turbine, Experiment in Fluids, Vol. 46 (2009), pp. 97-108.
38. Soerensen, J.N., VISCWIND, Viscous Effects on Wind Turbine. Blades, final report on the JOR3-CT95-0007, Joule III project, Technical Report ET-AFM-9902, Technical University of Denmark, (1999).
39. Spera, D.A., Wind Turbine Technology, Second edition, ASME Press, Chapter 5, pp.329-344 (2009).
40. Shimizu, Y., Maeda, T., Kamada,Y., Takada,M. and Katayama,T., Development of micro wind turbine (Orthoptere Wind Turbine), Proc. International Conference on Fluid Engineering JSME Centennial Grand Congress (1997), pp.1551-1556.
41. Tanaka, F., Kawaguchi, K., Sugimoto, S. and Tomioka, M., Influence of wing section and wing setting angle on the starting performance of a Darrieus wind turbine with straight wings, Journal of Environment and Engineering Vol. 6, No. 2 (2011), pp.302-315.
42. Takao, M., Maeda, T., Kamada, Y., Oki, M. and Kuma,H., A straight-bladed vertical axis wind turbine with a directed guide vane row, Journal of Fluid Science and Technology, Vol. 3, No. 3 (2008), pp.379-386.
43. Wang, Weizhang, and Mingbo Wang "Application of K-E Model on the Numerical Simulation of a Semi-confined Slot Turbulent Impinging Jet" Fourth International Joint Conference, 2011
44. Wang, S., Ingham, D.B., Ma, L., Pourkashanian, M., Tao,Z., Numerical investigations on dynamic stall of low Reynolds number flow around oscillating airfoils, Computers & Fluids, Vol.39, No.9, pp.1529-1541 (2010)

45. World Wind Energy Association 2011, World Wind Energy Report 2010, http://www.wwindea.org/home/images/ stories/pdfs/worldwindenergyreport2010_s.pdf, (accessed) May 06, 2014.
46. Yakhot, V. and Orszag, S.A., Renormalization group analysis of turbulence I basic theory, Journal of Scientific computing, Vol.1, No.1 (1986), pp. 1–51.
47. Yamada, S., Tamura, T. and Mochizuki, S., Effects of wing section on mean characteristics and temporal torque Variation for a small straight-bladed vertical axis wind turbine, Journal of Fluid Science and Technology, Vol. 6, No. 6 (2011), pp. 875-886.
48. Yamada, T., Kiwata, T., Kita, T., Hirai, M., Komatsu, N. and Kono,T., Over-speed control of a variable-pitch vertical-Axis wind turbine by means of tail vanes, Journal of Environment and Engineering, Vol. 7, No. 1 (2012), pp. 39-52.
49. Zhang, L.X., Liang, Y.B., Liu, X.H., Jiao, Q.F. and Guo, J., Aerodynamic performance prediction of straight-bladed vertical axis wind turbine based on CFD, Hindawi Publishing Corporation, Advances in Mechanical Engineering, Vol. 2013, Article ID 905379, 11 pages, http://dx.doi.org/10.1155/2013/905379.